# Scaling laws for stagnant-lid convection with a buoyant crust

## Kyle Batra $^1$ and Bradford Foley $^2$

<sup>1</sup>Department of Astronomy & Astrophysics, Pennsylvania State University <sup>2</sup>Department of Geosciences, Pennsylvania State University

5 Abstract

10

11

12

13

14

15

16

17

18

21

22

23

24

25

27

29

Stagnant-lid convection, where subduction and surface plate motion is absent, is common among the rocky planets and moons in our solar system, and likely among rocky exoplanets as well. How stagnant-lid planets thermally evolve is an important issue, dictating not just their interior evolution but also the evolution of their atmospheres via volcanic degassing. On stagnant-lid planets, the crust is not recycled by subduction and can potentially grow thick enough to significantly impact convection beneath the stagnant lid. We perform numerical models of stagnant-lid convection to determine new scaling laws for convective heat flux that specifically account for the presence of a buoyant crustal layer. We systematically vary the crustal layer thickness, crustal layer density, Rayleigh number, and Frank-Kamenetskii parameter for viscosity to map out system behavior and determine the new scaling laws. We find two end-member regimes of behavior: a "thin crust limit," where convection is largely unaffected by the presence of the crust, and the thickness of the lithosphere is approximately the same as it would be if the crust were absent; and a "thick crust limit," where the crustal thickness itself determines the lithospheric thickness and heat flux. Scaling laws for both limits are developed and fit the numerical model results well. Applying these scaling laws to rocky stagnant-lid planets, we find that the crustal thickness needed for convection to enter the thick crust limit decreases with increasing mantle temperature and decreasing mantle reference viscosity. Moreover, if crustal thickness is limited by the formation of dense eclogite, and foundering of this dense lower crust, then smaller planets are more likely to enter the thick crust limit because their crusts can grow thicker before reaching the pressure where eclogite forms. When convection is in the thick crust limit, mantle heat flux is suppressed. As a result, mantle temperatures can be elevated by 100s of degrees K for up to a few Gyrs in comparison to a planet with a thin crust. Whether convection enters the thick crust limit during a planet's thermal evolution also depends on the initial mantle temperature, so a thick, buoyant crust additionally acts to preserve the influence of initial conditions on stagnant-lid planets for far longer than previous thermal evolution models, which ignore the effects of a thick crust, have found.

**Key Words:** Planetary interiors, Planetary tectonics, Dynamics of lithosphere and mantle, Dynamics: convection currents, and mantle plumes

## $_{12}$ 1 Introduction

Stagnant-lid planets and satellites are common in the solar system, as Earth is the only rocky planet known to operate in a plate-tectonic regime of mantle convection (e.g. Breuer & Moore, 2015; Stern et al., 2018). Understanding the geologic history of rocky planets and moons in the solar system thus requires understanding the thermal evolution of stagnant-lid planets. Much work has been devoted to exploring the physics of stagnant-lid convection, in particular for determining scaling laws for convective heat flux or interior flow speed (e.g. Christensen, 1984; Ogawa et al., 1991; Davaille & Jaupart, 1993; Solomatov, 1995; Grasset & Parmentier, 1998; Reese et al., 1998; Dumoulin et al., 1999; Solomatov & Moresi, 2000; Reese et al., 2005; Korenaga, 2009; Weller & Lenardic, 2016; Thiriet et al., 2019), and modeling the thermal evolution of stagnant-lid planets with either parameterized models based on these scaling laws, or fully dynamic twoand three-dimensional convection models (e.g. Schubert et al., 1979; Spohn, 1991; Stevenson et al., 1983; Hauck & Phillips, 2002; Fraeman & Korenaga, 2010; Morschhauser et al., 2011; Grott et al., 2011; Plesa et al., 2015). The study of stagnant-lid planet evolution is also relevant to exoplanets. Whether exoplanets are more likely to have stagnant-lid tectonics, plate tectonics, or other intermediate forms of tectonics, is unclear and difficult to predict from first principles. Studies of exoplanet geodynamics have reached a range of conflicting conclusions on whether super-Earths are more likely to have plate tectonics or not, or even which planetary characteristics are most important for promoting plate tectonics (e.g. Valencia et al., 2007; O'Neill & Lenardic, 2007; Korenaga, 2010; Stamenkovic et al., 2011; van Heck & Tackley, 2011; Foley et al., 2012; Lenardic & Crowley, 2012; Stein et al., 2013; Noack & Breuer, 2014). However, given that these studies found that the operation of plate tectonics was quite sensitive to factors such as size, mantle heat budget, or the surface environment, and the ubiquity of stagnant-lids on the rocky objects of our solar system, stagnant-lid planets are likely to make up a significant portion of the exoplanet population. Operating in a stagnant-lid regime has important implications for a planet's volatile cycling and climate evolution. Plate tectonics has long been thought to be important, and possibly even essential, for a habitable surface environment, as it helps drive the carbonate-silicate cycle that regulates Earth's climate (e.g. Walker et al., 1981; Berner et al., 1983; Kasting & Catling, 2003; Foley & Driscoll, 2016). However, recent work has shown that stagnant-lid exoplanets can also sustain volatile cycling and outgassing that promotes a habitable climate, under some conditions (Noack et al., 2017; Tosi et al., 2017; Foley & Smye, 2018; Valencia et al., 2018; Foley, 2019; Höning et al., 2019). The thermal evolution of the mantle is critical for stagnant-lid planet climate evolution, as it dictates the rate of volcanic outgassing over time (Tosi et al., 2017; Dorn et al., 2018; Foley & Smye, 2018; Höning et al., 2019). Thus better constraints on the thermal evolution of stagnant-lid 64 planets will also allow better assessments of the potential for habitability of rocky exoplanets.

## 65 1.1 Crust formation and stagnant-lid convection

The physics of stagnant-lid convection in simple systems, where convection is purely thermally driven and viscosity depends only on temperature, is well understood. However, there are many additional complications present in real stagnant-lid planets that can significantly affect their thermal evolution. One such process is melting and subsequent chemical differentiation, which may be especially important early in stagnant-lid planets' histories, when mantle temperatures are expected to be high (e.g. Breuer & Moore, 2015; Byrne, 2020). In particular, mantle melting produces crusts that can grow thick on stagnant-lid planets, as there is no 71 subduction to constantly recycle this crust (e.g. Hauck & Phillips, 2002; Keller & Tackley, 2009; Morschhauser et al., 2011; Plesa & Breuer, 2014). The crust is chemically buoyant compared to the underlying mantle at 73 surface pressures, unless the degree of melting in the mantle is very high, but can become negatively buoyant due to metamorphic reactions at pressures  $> \sim 1-2$  GPa (e.g. Hacker, 1996). The crust is also expected 75 to be enriched in heat producing elements, as these elements are incompatible in the mantle (e.g. Hart & Brooks, 1974; Beattie, 1993), and to have a lower thermal conductivity than the mantle (e.g. Clauser & Huenges, 1995; Turcotte & Schubert, 2002). Each of these effects could significantly modulate a stagnant-lid planet's mantle dynamics and thermal history. Both a lower thermal conductivity in the crust, and enrichment of heat producing elements, can be incorporated in thermal evolution models using existing methods. A geotherm through the crust and stagnant-lid

Both a lower thermal conductivity in the crust, and enrichment of heat producing elements, can be incorporated in thermal evolution models using existing methods. A geotherm through the crust and stagnant-lid can be calculated from the heat conduction equation, and then the lid thickness can be determined based on a balance between the conductive heat flux at the base of the lid, and the convective heat flux supplied by the mantle (e.g. Hauck & Phillips, 2002; Grott et al., 2011, see also §6); this method has been successfully benchmarked against two- and three-dimensional convection models (e.g. Thiriet et al., 2019). However, when treating the crust in this manner, scaling laws for mantle convective heat flux are still needed.

Previous models have typically assumed that convective heat flux is unaffected by the presence of the crust (e.g. Morschhauser et al., 2011; Plesa & Breuer, 2014; Foley & Smye, 2018), or that standard stagnant-lid scaling laws apply to convection in the mantle beneath the crust (e.g. Fraeman & Korenaga, 2010). The buoyancy of the crust, however, could significantly modify the mantle convective heat flux, in particular if the crust grows thick. In many thermal evolution models, the crust grows so thick that it reaches the base of the stagnant lid, especially early in a planet's evolution, when mantle temperatures are high (e.g. Hauck & Phillips, 2002; Morschhauser et al., 2011; Plesa & Breuer, 2014; Foley & Smye, 2018). These models find that such thick crusts can form even when taking into account partitioning of heat producing elements

into the crust, and mantle depletion due to crustal extraction. However, many previous models ignore the influence crustal buoyancy could have on the dynamics at the base of the stagnant lid, and instead assume that all crust reaching the base of the lid founders into the mantle (e.g. Morschhauser et al., 2011; Plesa & Breuer, 2014; Foley & Smye, 2018); this is in keeping with the assumption that mantle convective heat flux is unaffected by the presence of the crust.

Assuming that crust always founders when reaching the base of the stagnant lid, and that lid thickness 100 is not influenced by the crust's buoyancy, is questionable. If the crust grows thick enough to reach the lid 101 base, its positive buoyancy could suppress foundering of the rheological sub-layer, the thin layer below the 102 lid where viscosities are low enough to fully participate in convection (e.g. Solomatov, 1995). As a result, 103 the effective thickness of the stagnant lid would increase, and the effective temperature difference driving 104 convection (that is, the temperature difference across the actively convecting portion of the mantle, beneath the stagnant lid) would decrease. Both of these effects would act to suppress convective heat flux. Lourenço 106 et al. (2018) argues that melting and crust production can enhance convective heat flux on stagnant-lid planets, via thermal weakening of the lower mantle lithosphere by melt migration. However, once the crust 108 has grown thick enough to reach the stagnant-lid base, thermal weakening will not help drive foundering, 109 since it is the crust's buoyancy that resists sinking rather than the lid's viscosity. Scaling laws for convective 110 heat flux when a thick, buoyant crust influences foundering at the base of the stagnant lid have not been 111 developed, nor has this effect been incorporated in thermal evolution models. The goal of our paper is thus 112 to accomplish this task. 113

The formation of eclogite, or other dense phases, in the lower crust can drive crustal foundering, and hence limit crustal thickness. As a result, in applying our newly developed scaling laws for heat flux with a buoyant crust to stagnant-lid planets, we will limit crustal thickness to the depth where eclogite forms (see §5). Moreover, crustal foundering driven by eclogite could also drag the underlying lithospheric mantle with it, in addition to limiting the crustal thickness (e.g. Johnson et al., 2014). If lithospheric mantle is entrained by foundering crust, the stagnant lid thickness will be decreased, at least during periods of crustal foundering, enhancing convective heat flux. While the effect of foundering dense crust could be important, at least for transient periods when foundering is active, it is beyond the scope of this study. Here we will focus solely on buoyant crusts. Future work will consider heat flux variations during crustal foundering events.

114

115

117

118

119

120

121

122

123

124

126

In addition to the crust, mantle melting also forms a depleted mantle layer below the crust (e.g. Schott et al., 2001; Fraeman & Korenaga, 2010; Plesa & Breuer, 2014). The depleted mantle is also buoyant compared to the primitive mantle, although depleted mantle density is larger than crust density in most cases. In addition, depleted mantle may have an elevated viscosity compared to primitive mantle, due to dehydration during melting (e.g. Hirth & Kohlstedt, 1996). The influence of a depleted mantle layer on

heat flux and thermal evolution of stagnant-lid planets has already been studied extensively (e.g. Schott et al., 2001; Korenaga, 2009; Fraeman & Korenaga, 2010; Morschhauser et al., 2011; Ogawa & Yanagisawa, 2011; Plesa & Breuer, 2014), so we will neglect this effect here and focus our modeling solely on the crust's buoyancy.

## 1.2 Previous work on thermo-chemical convection

132

There are a number of other important aspects of chemical geodynamics, a topic which includes the effects of chemical differentiation on mantle convection and the corresponding effects of mantle convection on 134 the formation and evolution of chemical heterogeneity, that have received extensive study previously (e.g. 135 Tackley, 2015). These include studying whether chemical differentiation of the mantle, either during magma ocean solidification or later magmatism and crust production, can lead to large-scale layering within the 137 mantle, the effects of melting and crust production on the properties and dynamics of the lithosphere, and the mixing of chemical heterogeneities by mantle convection (see e.g. Kellogg, 1992, for a review of mixing). 139 Some early studies considered whether the upper and lower mantles convected separately on Earth, due to density differences induced either by phase transitions (e.g. Christensen & Yuen, 1985; Tackley et al., 141 1993) or by differences in composition (e.g. Richter & Johnson, 1974; Richter & McKenzie, 1981; Davaille, 1999). Chemical layering could be primordial, developing as a result of fractional crystallization during 143 magma ocean solidification (e.g. Elkins-Tanton et al., 2003; Zaranek & Parmentier, 2004; Tosi et al., 2013), formed by deposition of dense, garnet-bearing crust in the lower mantle via subduction (e.g. Ogawa & Nakamura, 1998), or a combination of the two. However, seismic evidence now indicates that convection operates across the whole mantle (e.g. Helffrich & Wood, 2001), with any layering confined to the very lowermost mantle (e.g. Kellogg et al., 1999), most likely the large low shear velocity provinces (LLSVPs) 148 (e.g. Garnero & McNamara, 2008; Hernlund & McNamara, 2015). The formation and evolution of LLSVPs has received significant attention, in particular focusing on the density needed to explain the present day 150 shapes and persistence of these features (e.g. Davaille, 1999; McNamara & Zhong, 2005; Li & McNamara, 2013; Mulyukova et al., 2015; Jones et al., 2020). 152 More relevant to our study is previous work on how chemical differentiation modifies the properties and dynamics of the lithosphere. The effect of crustal buoyancy on the operation of plate tectonics on Earth has been well studied. A thick, buoyant crust can potentially prevent subduction (e.g. Oxburgh 155 & Parmentier, 1977; Vlaar, 1985; Davies, 1992; van Thienen et al., 2004b), however, even in this case local crustal thickening and the formation of eclogite can still drive at least short-lived subduction episodes 157 (van Thienen et al., 2004a). The formation of depleted mantle coincident with crust production modifies lithospheric viscosity. If the depleted mantle is very thick, then it can dictate the thickness of the lithosphere and suppress convective heat flux in a plate-tectonic regime (e.g. Korenaga, 2006), similar to what we show for stagnant-lid convection with a buoyant crust. Also relevant to our study is work on mantle convective heat flux through continents. Continents also suppress convective heat flux, effectively insulating the underlying mantle, and we find that the same principles used to develop scaling laws for this effect also work for our case of stagnant-lid convection (e.g. Lenardic & Kaula, 1996; Lenardic, 1998; Lenardic et al., 2005; Van Thienen, 2007).

Finally, as reviewed above in §1.1, the formation and evolution of crust and depleted mantle for stagnantlid planets, in particular Mars, has been studied previously. However, despite some studies where the
formation of buoyant crust due to mantle melting is modeled for Mars (Keller & Tackley, 2009; Ruedas
et al., 2013), no study has yet carefully examined how a buoyant crust influences convective heat flux, nor
developed scaling laws that can be used in parameterized thermal evolution models.

## 1.3 Purpose of this study

171

180

181

183

185

As outlined above, our study focuses on how a thick, buoyant crust modulates the dynamics of the base of
the stagnant lid, and hence convective heat flux, as this is a key remaining uncertainty in the role melting and
crust formation plays in stagnant-lid thermal evolution. We will focus solely on the role of crustal buoyancy,
as the effects of heat producing element enrichment in the crust and a lower thermal conductivity in the
crust have already been extensively studied. Likewise, the formation of a depleted mantle layer beneath the
crust has also been carefully studied previously, and will be neglected here. We will also only consider thick
buoyant crusts; how foundering of dense lower crust influences stagnant-lid convective heat flux is outside
this study's scope.

We therefore use simple numerical convection models to study how convective heat flux scales when a thick, buoyant crust is present, and to develop new scaling laws based on these models. We then apply these scaling laws to stagnant-lid planets, by first demonstrating the conditions under which crustal buoyancy significantly influences convective heat flux, assuming the crust can grow no thicker than the depth where eclogite forms. We then demonstrate how crusts up to this maximum thickness imposed by the formation of eclogite would influence stagnant-lid planet thermal evolution.

In both sets of models, the model set up will be kept as simple as possible. In the numerical convection models, we model convection in a two-dimensional Cartesian domain, with a strongly temperature-dependent viscosity and an imposed chemically buoyant layer at the surface representing the crust. As we focus solely on the influence of crustal buoyancy, the only distinguishing feature of the crustal layer in our models is its

buoyancy. We systematically vary the thickness of the crustal layer and the Rayleigh number over a wide parameter range, such that robust scaling laws can be developed.

The crustal layer in the numerical convection models can evolve as a result of mantle flow, becoming 192 thickened in regions of convergence and thinned in regions of divergence, but the volume of the crust is fixed. Crust is neither created by mantle melting nor destroyed by foundering. We also do not consider 194 mantle heat loss by melting, which can dominate when the mantle is hot, and keep the mantle temperature 195 regulated near the solidus (e.g. O'Reilly & Davies, 1981; Turcotte, 1989; Keller & Tackley, 2009; Ogawa & Yanagisawa, 2011; Nakagawa & Tackley, 2012; Moore & Webb, 2013). However, even in this case it is 197 important to know the thickness of the lithosphere and convective heat flux, which can be influenced by the 198 presence of the crust, as the scaling laws we develop in this paper show. Moreover, as volcanism rates decline. 199 convective heat loss will become the primary mode of mantle cooling. In this case, with a potentially thick crust left behind from prior volcanism, our scaling laws will be directly relevant for modeling subsequent 201 mantle thermal evolution.

In applying our scaling laws to stagnant-lid planet thermal evolution, we will make similar assumptions. 203 We will again focus solely on crust buoyancy, and neglect a lower thermal conductivity in the crust and 204 enrichment of heat producing elements. These effects are discussed in §6, and there we show that including 205 them would only reinforce our conclusions about how crustal buoyancy modulates mantle convective heat 206 flux. We will also assume fixed buoyant crustal layers, so the role of crustal buoyancy can be illustrated in 207 a simple manner. Time-evolving crustal thickness can be tracked with a model explicitly calculating mantle 208 melting and crust production, which our new heat flux scaling laws can be incorporated into; this is left 209 as a topic for future work. Throughout the paper, our models (both the numerical convection models and 210 thermal evolution models) will treat the crust as simply a buoyant layer, and neglect other characteristics of the crust as discussed above. We will still refer to this buoyant layer in our models as "crust," given that 212 this is the physical feature we are modeling. However, readers should note the other differences between 213 crust and mantle that our models neglect, as discussed here and further in §6. 214

The paper is organized as follows. The background theory and numerical model setup is described in §2, the numerical model results explained in §3, and scaling analysis presented in §4. In §5 we constrain the planetary characteristics (planet size, reference viscosity, and interior temperature) where a thick crust capable of impeding convective heat flux can form, and apply our new scaling laws to a set of simple models of stagnant-lid planet thermal evolution. Finally, we discuss key uncertainties in our scaling laws and modeling in §6, and summarize conclusions in §7.

## 221 2 Theory

250

251

## 2.1 Background and Governing Equations

Our models of thermo-chemical stagnant-lid convection, with an imposed buoyant layer representing the
crust, are performed in a two-dimensional Cartesian domain. Two-dimensional models capture the essential
physics of convection with a buoyant crust and are computationally cheap in comparison to three-dimensional
models, allowing for a large exploration of the relevant parameter space. In the models a purely temperaturedependent viscosity is used, with ratios of surface viscosity to mantle interior viscosity large enough to induce
stagnant-lid convection, as explained below.

The buoyant crust is represented by a chemical composition field, C. For the crust, C=1 and for 229 the mantle C=0. As chemical diffusion is slow compared to thermal diffusion (e.g. van Keken et al., 230 1997; Tackley & King, 2003), diffusion of composition is ignored and crust is only advected around the 231 domain. The buoyancy of the crust relative to the mantle due to composition is described by the buoyancy 232 number,  $B = \Delta \rho_c/(\rho \alpha \Delta T)$ , where  $\Delta \rho_c$  is the density difference between crust and mantle due solely to 233 composition, and  $\rho\alpha\Delta T$  is the density difference across the mantle due solely to temperature (where  $\rho$  is average mantle density,  $\alpha$  is the thermal expansion coefficient, and  $\Delta T = T_m - T_s$  is the super-adiabatic 235 temperature difference across the mantle, or the difference between the potential temperature at the bottom of the mantle,  $T_m$ , and the surface temperature,  $T_s$ ). 237

Our models are purely bottom heated, which is clearly a simplification as rocky planets will also likely be 238 heated significantly from within by radionuclides and primordial heat, as is the case for Earth (e.g. Jaupart 239 et al., 2015). Rocky exoplanets can also experience significant tidal heating (e.g. Jackson et al., 2008; Jackson 240 et al., 2008; Driscoll & Barnes, 2015). Previous work on stagnant-lid convection has found, however, that 241 purely bottom heated and purely internally heated convection result in the same scaling laws for convective 242 heat flux, when convection is described by an internal Rayleigh number, which we introduce below in §4 (e.g. Solomatov, 1995; Solomatov & Moresi, 2000; Korenaga, 2009). Our model setup is thus justifiable for a first 244 order analysis of how a thick, buoyant crustal layer influences convective heat flux. Changing the relative contributions of bottom and internal heating can cause deviations from the scaling laws found for either 246 pure bottom heating or pure internal heating, due to the changing strength of upwelling plumes (Moore, 247 2008; Weller & Lenardic, 2016; Weller et al., 2016; Korenaga, 2017). Thus exploring how the scaling laws 248 we develop depend on the percentage of internal heating is an important avenue for future work. 249

Our model solves the standard equations for conservation of mass, momentum, energy, and chemical composition, assuming infinite Prandtl number and applying the Boussinesq approximation. The equations are given below in terms of non-dimensional variables, where the following scales are used in the non-

Table 1: Key variables and non-dimensional parameters used in numerical models

Variable	Meaning	Equation
$\underline{v}'$	Velocity	(1)
$t^{'}$	Time	(2)
$P^{'}$	Pressure	(2)
$C_{\cdot}^{\prime}$	Composition $(C' = 1 \text{ is crust}, C' = 0 \text{ is mantle})$	(2) & (3)
$T^{'}$	Temperature	(2) & (4)
$\dot{\underline{arepsilon}}'$	Strain rate tensor	(2)
$\mu^{'}$	Viscosity	(2) & (5)
Non-dimensional parameter	Meaning	Equation
B	Buoyancy number	(2)
$Ra_0$	Reference Rayleigh number	(2)
heta	Frank-Kamenetskii parameter	(5) & (6)
$\delta_{c0}^{'}$	Initial crustal thickness	above $(7)$

Table 2: Quantities output from numerical models and parameters and variables used in scaling analyses

Output quantity	Meaning	Equation
		Lquation (7)
Nu	Nusselt number	(7)
$T_i^{'}$	Internal temperature	below $(7)$
$T_i^{'} \ \delta_c^{'}$	Crustal thickness	below $(7)$
$Ra_i$	Internal Rayleigh number	(8)
$\mu_i^{'}$	Interior mantle viscosity	below $(8)$
Parameter or variable	Meaning	Equation
$\delta_0^{\prime}$	Lithosphere thickness when crust is absent	(12) & (13)
$\delta_{sl}^{'}$	Sub-crustal thermal boundary layer thickness	(17)
$Ra_c$	Critical Rayleigh number	(17)
$\delta_{bot}^{'}$	Bottom thermal boundary layer thickness	(23)
$\overset{\circ}{C_1}$	Nusselt number scaling law constant $(C_1 = 0.48)$	(10)
$C_2$	Nusselt number scaling law constant $(C_2 = 2.95)$	(9)
$C_3$	Temperature scaling law constant $(C_3 = 2)$	(23)

dimensionalization (primes denote non-dimensional variables throughout the text):  $\underline{x} = \underline{x}'d$ , where  $\underline{x}$  is the spatial coordinate and d is the thickness of the mantle;  $t = t'd^2/\kappa$ , where t is time and  $\kappa$  is the thermal diffusivity of the mantle;  $\underline{v} = \underline{v}'\kappa/d$ , where  $\underline{v}$  is velocity;  $T = T'\Delta T + T_s$ , where T is temperature;  $P = P'\mu_m\kappa/d^2$ , where P is dynamic pressure and  $P_m$  is the reference viscosity of the mantle, defined as the viscosity at the basal mantle temperature,  $T_m$ ; and  $\underline{\dot{\varepsilon}} = \underline{\dot{\varepsilon}}'\kappa/d^2$ , where  $\underline{\dot{\varepsilon}} = 1/2(\partial u_i/\partial x_j + \partial u_j/\partial x_i)$  is the strain-rate tensor. The governing equations, in terms of non-dimensional variables, are

$$\nabla \cdot \underline{v}' = 0 \tag{1}$$

259

$$0 = -\nabla P' + \nabla \cdot (2\mu' \underline{\dot{\varepsilon}}') + Ra_0(T' - BC')\underline{\hat{z}}$$

$$\tag{2}$$

200

$$\frac{\partial C'}{\partial t'} + \underline{v}' \cdot \nabla C' = 0 \tag{3}$$

261

262

$$\frac{\partial T^{'}}{\partial t^{'}} + \underline{v}^{'} \cdot \nabla T^{'} = \nabla^{2} T^{'} \tag{4}$$

$$\mu' = e^{(\theta(1-T'))}. (5)$$

Here,  $\hat{z}$  is the unit vector in the vertical direction and the reference Rayleigh number,  $Ra_0$ , is defined as  $Ra_0 = \rho g \alpha \Delta T d^3/(\kappa \mu_m)$ , where g is gravitational acceleration. The definitions of all key variables, non-dimensional parameters, and output quantities calculated from the numerical models can be found in Tables (1) and (2). The viscosity, Eq. (5), follows a Frank-Kamenetskii approximation of the full Arrhenius temperature-dependent viscosity law; this simplifies the scaling analysis as only one parameter, the Frank-Kamenetskii parameter, is involved in the viscosity law (e.g. Solomatov & Moresi, 2000; Korenaga, 2009).

$$\theta = \frac{E_v \Delta T}{R(T_s + \Delta T)^2} \tag{6}$$

where  $E_v$  is the activation energy for viscosity and R is the universal gas constant. The difference between the Frank-Kamenetskii approximation and a full Arrhenius viscosity law is smallest at the high temperatures that prevail beneath the stagnant lid, and therefore actively participate in convection. As a result, scaling laws for convective heat flux developed with a Frank-Kamenetskii approximation have been found to only need a minor correction factor to fit numerical experiments performed with a full Arrhenius temperaturedependent viscosity law (Korenaga, 2009). The choice of viscosity law in our numerical convection models should thus not significantly impact our resulting scaling laws, or applications to rocky stagnant-lid planets. In most models we use  $\theta = 13.82$ , which results in a viscosity ratio between the surface and base of the

mantle of 10<sup>6</sup>, easily large enough to lie within the stagnant lid regime (e.g. Solomatov, 1995). We also explore the impact of  $\theta$  in our scaling laws by running an additional set of models at  $\theta = 16.12$ , which results in a viscosity ratio of  $10^7$ . 280

#### 2.2 Numerical model setup 281

289

291

293

294

295

296

297

298

302

The model equations (1)-(6) are solved using a finite volume code, as outlined in Foley & Bercovici (2014) 282 and Foley et al. (2014). The top and bottom boundaries are free slip, while the side boundaries are periodic. 283 The temperature is fixed to non-dimensional values of 0 and 1 at the top and bottom, respectively. To solve 284 for the advection of chemical composition, the tracer ratio method is used (Tackley & King, 2003). The 285 implementation of the tracer ratio method used in this code was benchmarked against the density-driven overturn test cases presented in van Keken et al. (1997); the results of these benchmark tests are shown in 287 the supplementary material of Foley & Rizo (2017).

The modeling strategy is to run sets of models with an increasingly thick buoyant layer representing the crust, at fixed  $Ra_0$  and  $\theta$ , to determine how the buoyancy of the crust and its thickness influences the underlying convection and surface heat flux. These sets of models are then repeated at different Rayleigh numbers and Frank-Kamenetskii parameters, to constrain the influence of these factors and to develop complete scaling laws for the surface heat flux from stagnant-lid convection with a buoyant crustal layer. Models are started from one of two possible initial conditions: an initially static, conductive mantle, with convection developing as a result of small initial perturbations added to the temperature field; and an already developed, statistical steady-state convection pattern to which a buoyant crustal layer is added. In the second case, the initial conditions used are from models without a crust that had been previously run at the same Rayleigh number and Frank-Kamenetskii parameter. Test cases found that models with the same parameters and buoyant layer thicknesses, but different initial conditions (i.e. starting from either a static, conductive mantle or an already developed, statistical steady-state convection pattern), result in the same 300 final interior temperature and Nusselt number at statistical steady-state. Our numerical convection model results are therefore independent of the initial condition.

The initial thickness of the buoyant crustal layer,  $\delta'_{c0}$ , is imposed as part of the initial condition. This layer 303 is then free to evolve self-consistently in response to the underlying convection pattern in the mantle. As a 304 result, there can be some entrainment of the crust into the mantle, so we track how crustal thickness evolves 305 over time, as outlined below. Most models use a buoyancy number of B = -1, where negative numbers correspond to buoyant material. We also ran sets of models with buoyancy number varying between -0.3307 and -0.7, to test if buoyancy number significantly influences the dynamics. In the numerical models we vary the non-dimensional parameters  $Ra_0$  and B independently to map out system behavior. On a real planet,  $Ra_0$  and B are related through mantle temperature, as decreasing mantle temperature will decrease  $Ra_0$ and increase B, for a fixed  $\Delta \rho_c$ . However, the resulting scaling laws will capture these co-dependencies, and allow self-consistent thermal evolution models to be developed; this is analogous to isochemical stagnantlid convection where  $\theta$  and  $Ra_0$  are both functions of mantle temperature as well, and typically varied independently when developing scaling laws.

With an average mantle density of  $\rho = 4500 \text{ kg} \cdot \text{m}^{-3}$ , thermal expansivity of  $\alpha = 3 \times 10^{-5} \text{ K}^{-1}$ , and 315 temperature difference across the mantle of  $\Delta T = 1350$  K, as on the modern day Earth, our chosen range of 316 buoyancy numbers scale to  $\Delta \rho_c \approx -55$  to  $-180 \text{ kg} \cdot \text{m}^{-3}$ . With a hot interior temperature giving  $\Delta T = 2000$ 317 K, the resulting chemical density differences range from  $\Delta \rho_c \approx -80$  to  $-270 \text{ kg} \cdot \text{m}^{-3}$ . The crusts of Venus 318 and Mars are predominantly mafic (e.g. Taylor & McLennan, 2009), as volcanism is expected to result mostly from primary melting of the mantle. Basalt has a density  $\approx 300-400~{\rm kg\cdot m^{-3}}$  lower than peridotite at surface 320 temperature and pressure. Higher temperature melts, such as komatiites, are denser, and only  $\approx 100-200$ kg·m<sup>-3</sup> less dense than peridotite (Arndt, 1983). Our chosen range of buoyancy numbers is consistent with 322 mafic crusts at the high end (B = -1.0), and also allows us to consider potentially denser crusts at the 323 low end (B = -0.3), to test whether a smaller density difference between crust and mantle significantly 324 influences the dynamics at the base of the lid when the crustal layer is thick. 325

To analyze the model results and develop scaling laws, we calculate the time averaged Nusselt number (Nu), internal temperature  $(T_i')$ , and average crustal thickness  $(\delta_c')$  from the numerical models. Convection simulations were run until a statistical steady-state is reached for Nu,  $T_i'$ , and  $\delta_c'$ . Most models experience some entrainment of the buoyant crustal layer early in the model run, but then show an approximately constant buoyant layer thickness for the remainder of the run. However, models with B = -0.7, -0.5, and -0.3 show higher rates of entrainment that continue throughout the model run, such that a statistical steady-state is never reached (see §3.1). For the models reaching statistical steady-state, we calculate time averages of Nu,  $T_i'$ , and  $\delta_c'$  during the time period after statistical steady-state is reached. For models that don't reach statistical steady-state due to entrainment of the buoyant crustal layer, we take time averages over a short time window of 25 timesteps at the end of the model run, after the model has reached an approximately constant rate of entrainment.

Nusselt number is calculated as

326

327

328

329

331

332

333

334

335

336

337

$$Nu = \left\langle \frac{\partial T'}{\partial z'} \right\rangle_{z'=1} \tag{7}$$

at each time step, where  $\langle \partial T^{'}/\partial z^{'}\rangle_{z^{'}=1}$  is the horizontal average of the vertical temperature gradient evaluated at  $z^{'}=1$ , the top of the domain. The resulting time series is then integrated in time to find the time

averaged Nusselt number. The internal temperature is measured based on horizontally averaged, vertical profiles of temperature through the mantle. Horizontally averaged temperature has a local maximum just below the base of the stagnant lid; we designate this maximum as the interior temperature at each timestep, as this is the temperature that controls the dynamics of the base of the stagnant lid. Time averaging for internal temperature is the same as for Nusselt number.

Finally, to determine the thickness of the buoyant crustal layer, we calculate a contour line at C'=0.95,
which occurs at the base of this layer, and then horizontally average the depth of this contour across the
mantle. This calculation of crustal layer thickness is done as a post-processing step, using the full compositional field in two dimensions. The full composition field is output less frequently than the calculations
of Nu and  $T'_i$ , which are done every timestep. However, there is sufficient time resolution to produce time
averages of crustal thickness after each model has reached statistical steady-state.

## 351 Results

Example numerical model results with  $Ra_0 = 10^6$ ,  $\theta = 13.82$ , B = -1.0 and increasing initial crustal thicknesses,  $\delta'_{c0}$ , are shown in Figures 1-2 (a compilation of all numerical model results and input parameters can be found in Table 4). The results can largely be grouped into two end member regimes of behavior: a "thin crust limit" and a "thick crust limit." In the thin crust limit, the initial crustal layer is much thinner than the stagnant lid thickness of the "control" case, where the crust is absent; that is  $\delta'_{c0} << \delta'_0$ , where  $\delta'_0$  is the stagnant lid thickness with no crust present.

In this thin crust limit, the convection planform, Nusselt number, and interior mantle temperature 358 are hardly affected by the presence of the crust or by changing the crust's thickness (e.g. the cases with  $\delta_{c0}' = 0.1 - 0.2$  in Figures 1 & 2). As active convection is already confined to the region beneath the stagnant 360 lid, a thin crust that sits entirely within the lid does not significantly impact convection or surface heat flux. 361 However, as crustal thickness is increased, the thick crust limit is reached; in this limit the thickness of the 362 crust itself controls the lid thickness. Thus with increasing crustal thickness, convection is confined to a 363 smaller and smaller region beneath the base of the crust. The effective thickness of the lithosphere increases, 364 thereby decreasing the Nusselt number and increasing the mantle interior temperature, due to less efficient 365 heat loss from the mantle (e.g. the cases with  $\delta'_{c0} = 0.3 - 0.5$  in Figures 1 & 2).

The same trends in convection planform, Nusselt number, and mantle interior temperature are seen at different Rayleigh numbers and when the Frank-Kamenetskii parameter is varied. Figures 3-4 show the convective planform, time evolution of Nusselt number, and time evolution of mantle interior temperature, for models with  $Ra_0 = 10^8$ ,  $\theta = 13.82$ , B = -1.0, and a range of crustal thicknesses. As before, when

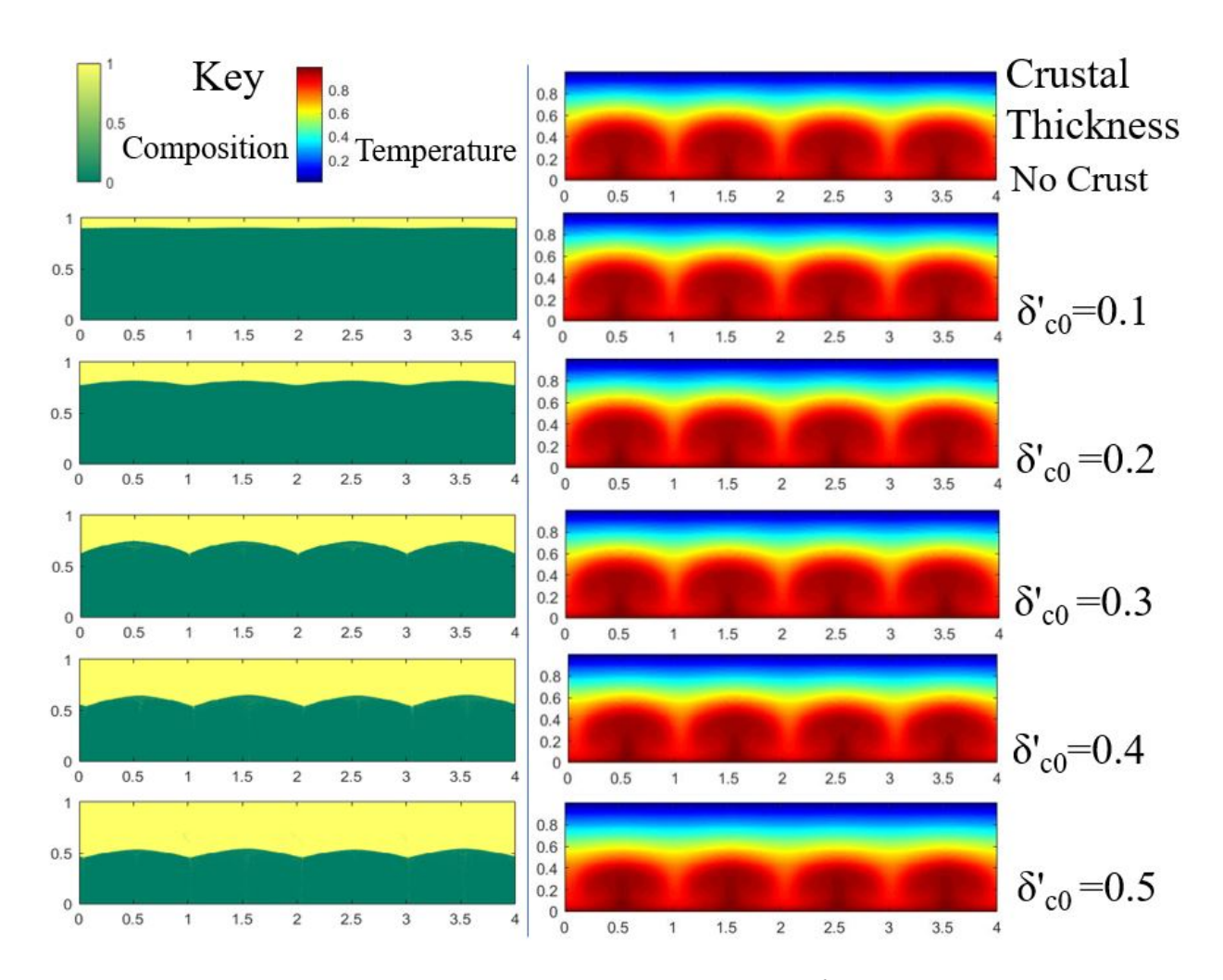


Figure 1: Convection pattern at steady-state for models with  $Ra_0 = 10^6$  &  $\theta = 13.82$ , showing both the composition field (left) and temperature field (right). For the composition field, C' = 1 represents crust, while C' = 0 represents mantle. Models with increasing initial crustal thickness,  $\delta'_{c0}$ , are shown, starting from the case with no crust at the top, and increasing initial crustal thickness to  $\delta'_{c0} = 0.5$  at the bottom.

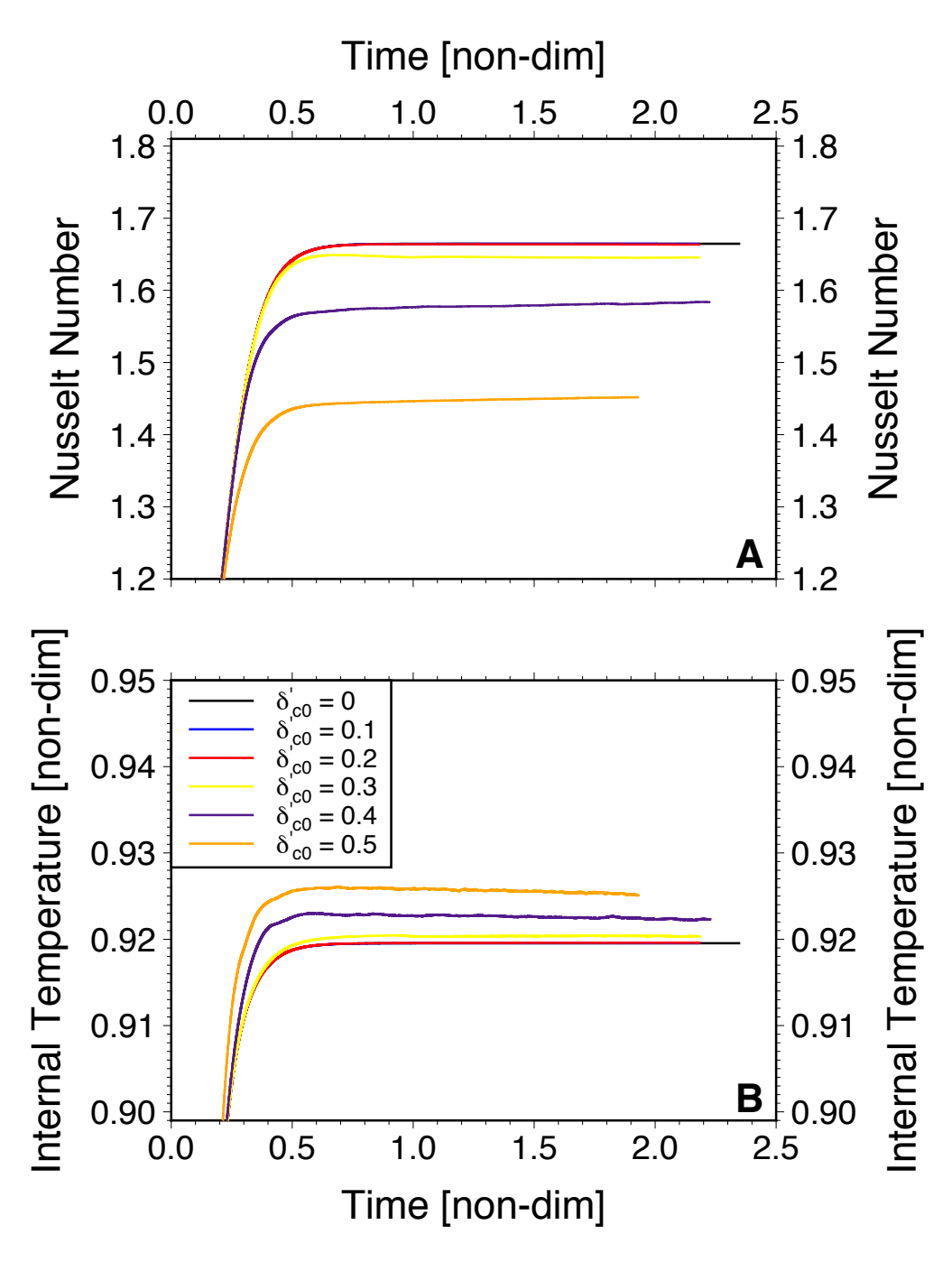


Figure 2: Nusselt number as a function of time (A) and mantle internal temperature as a function of time (B), for models with  $Ra_0 = 10^6$ ,  $\theta = 13.82$ , and for initial crustal thicknesses,  $\delta'_{c0}$ , as given in the legend. Models correspond to those shown in Figure 1.

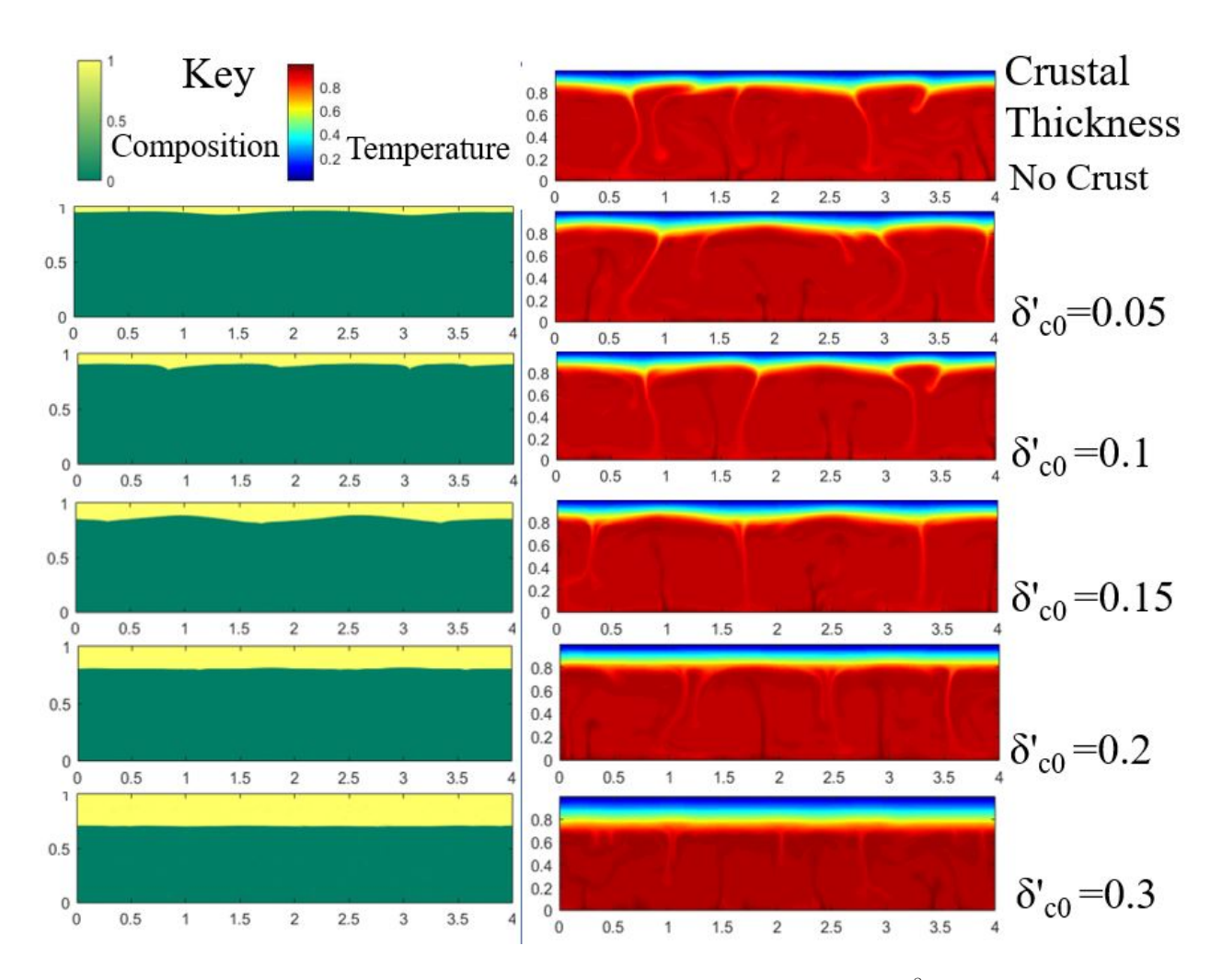


Figure 3: Convection pattern at statistical steady-state for models with  $Ra_0 = 10^8$  &  $\theta = 13.82$ . Analogous to Figure 1.

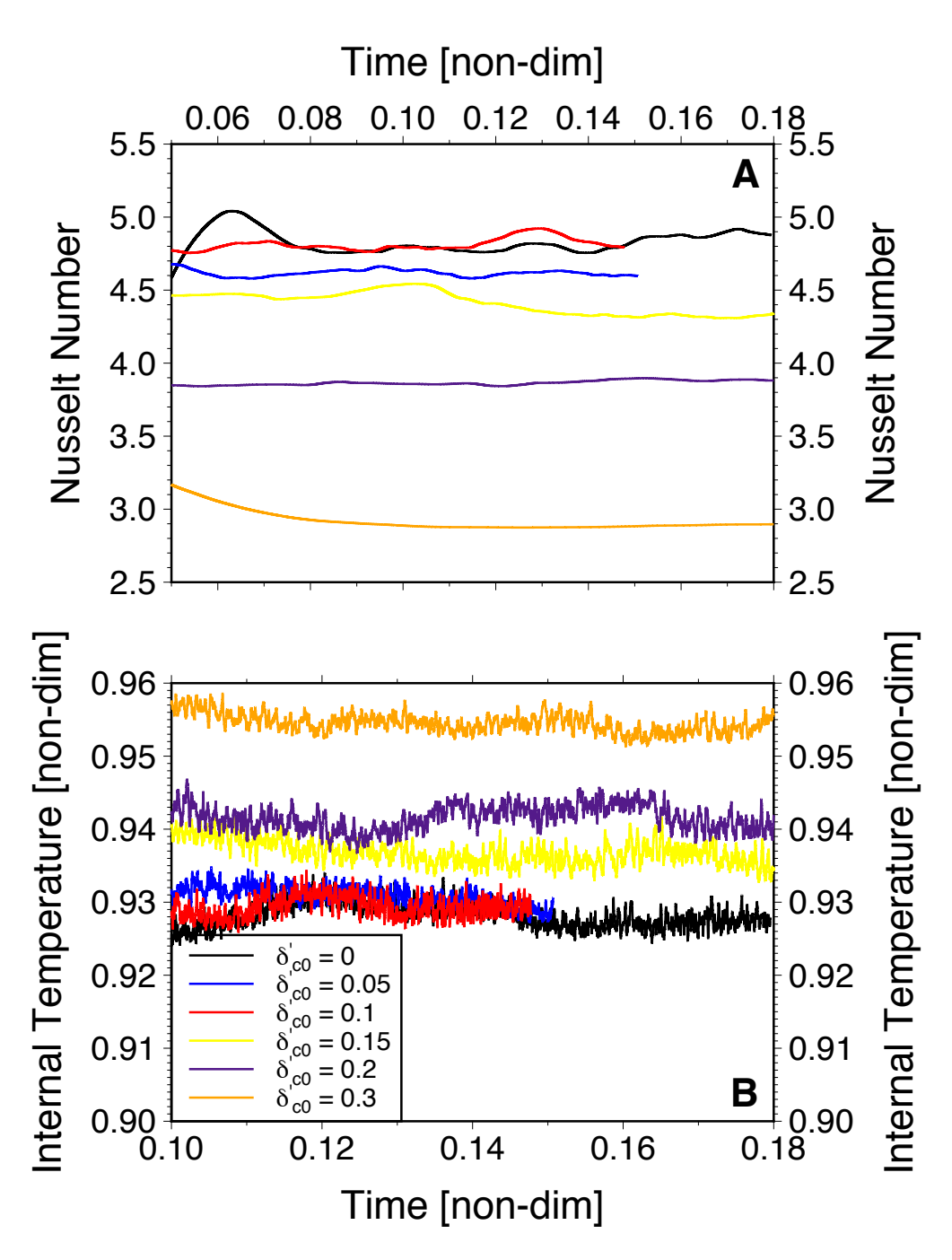


Figure 4: Nusselt number as a function of time (A) and mantle internal temperature as a function of time (B), for models with  $Ra_0 = 10^8$ ,  $\theta = 13.82$ , and for initial crustal thicknesses,  $\delta'_{c0}$ , as given. Models correspond to those shown in Figure 3.

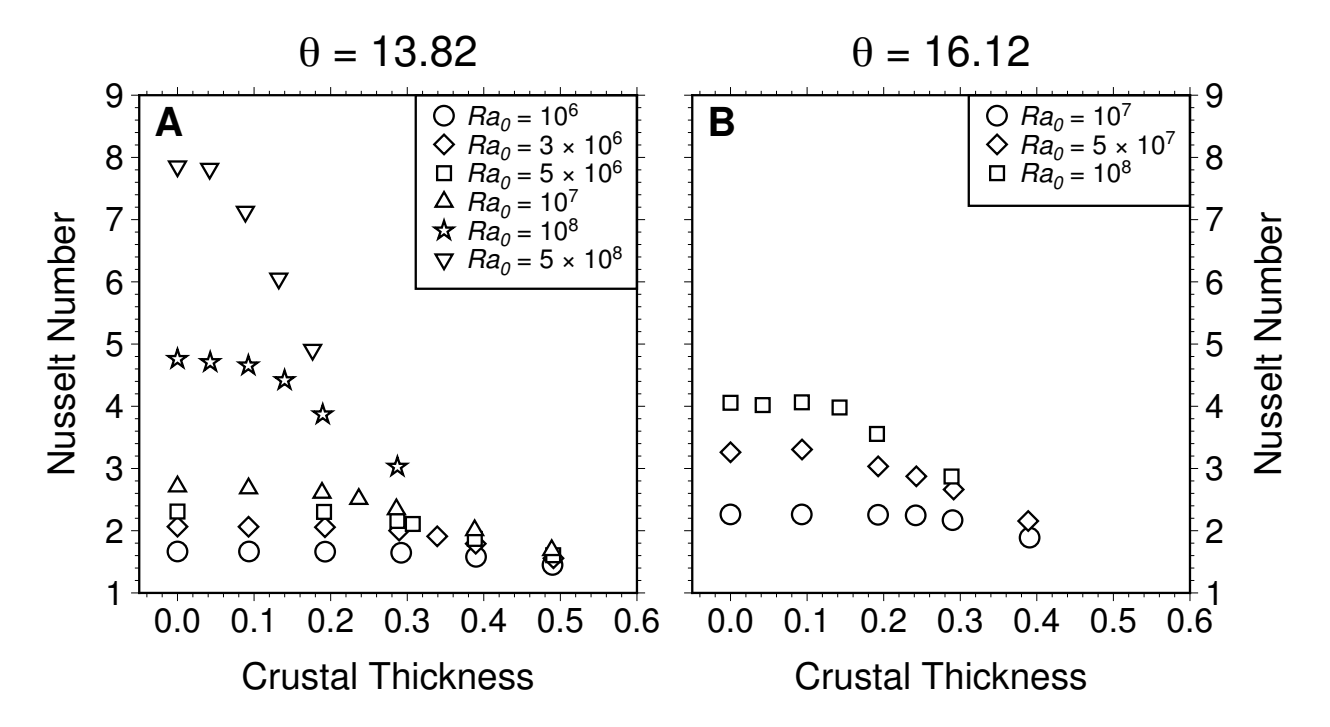


Figure 5: Average Nusselt number (Nu) as a function of average crustal thickness  $(\delta'_c)$  for models with  $Ra_0$  as specified in the legend and  $\theta = 13.82$  (A) and  $\theta = 16.12$  (B). As explained in the text (see §2.2), both Nusselt number and average crustal thickness are time averages after the models have reached statistical steady-state.

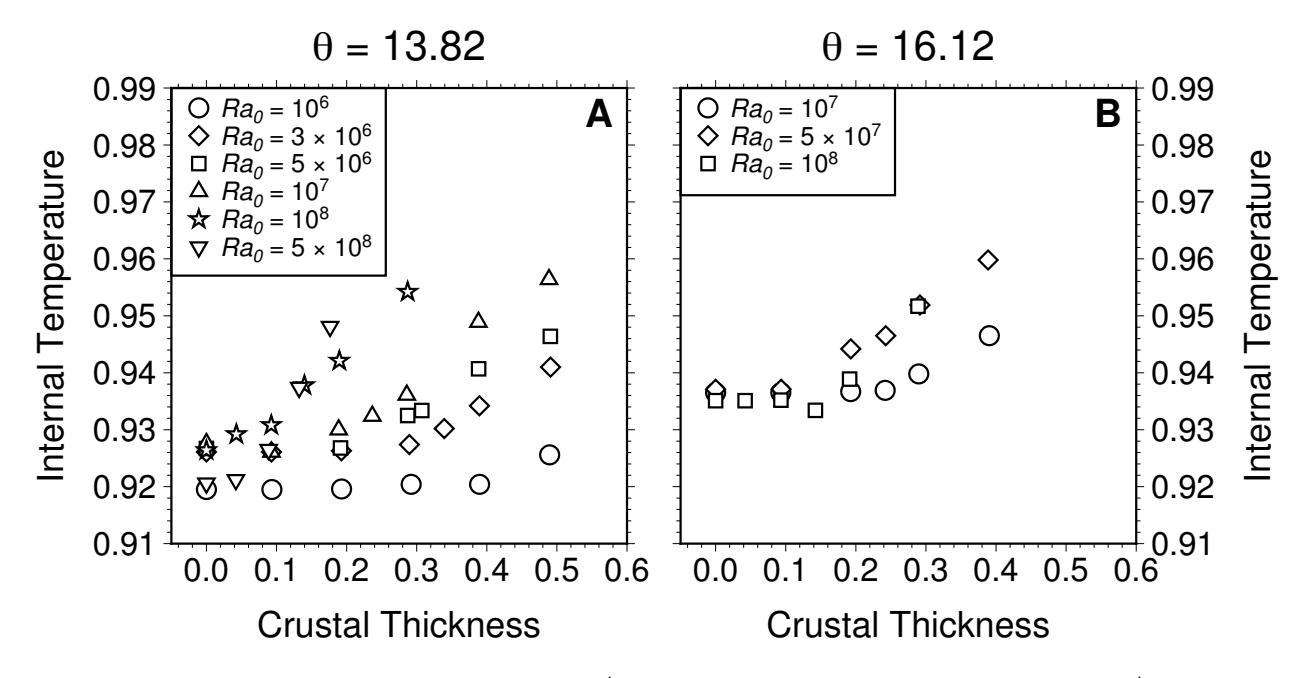


Figure 6: Average mantle interior temperature  $(T_i')$ , as a function of average crustal thickness  $(\delta_c')$  for models with  $Ra_0$  as specified in the legend and  $\theta = 13.82$  (A) and  $\theta = 16.12$  (B), as in Figure 5.  $T_i'$  is calculated from the numerical models as outlined in §2.2.

 $\delta'_{c0} << \delta'_0$ , changing crustal thickness has negligible impact. However, for crustal thicknesses larger than a critical crustal thickness, the crust itself dictates the stagnant lid thickness, and from this point onward increasing crustal thickness leads to lower Nusselt numbers and higher interior temperatures. As higher Rayleigh number convection produces a thinner stagnant-lid, when the crust is absent, than lower Rayleigh number convection, the critical crustal thickness where the thick crust limit is reached occurs at a lower value. With  $Ra_0 = 10^8$ , the thick crust limit is reached with initial crustal thicknesses of  $\delta'_{c0} \geq 0.15$ , while with  $Ra_0 = 10^6$  crustal thicknesses of  $\delta'_{c0} \geq 0.3 - 0.4$  are needed before the thick crust limit is reached.

Plotting time averaged Nusselt number as a function of time averaged crustal thickness for all model results with B=-1.0 further highlights the trends discussed above (Figure 5). Time averages of Nusselt number and crustal thickness are calculated as described in §2.2. For these models with B=-1.0, there is some initial entrainment of the crust at the start of the model run, but eventually a statistical steady-state is reached where Nu,  $T_i'$ , and  $\delta_c'$  are all constant. Nu and  $\delta_c'$  values reported in Figure 5 are for convection after this statistical steady-state is reached.

378

379

380

381

382

383

For a given Rayleigh number and Frank-Kamenetskii parameter, all models show an approximately 384 constant Nusselt number with increasing crustal thickness, for low crustal thicknesses; this regime of behavior 385 is the thin crust limit. Then a sharp decline in Nusselt number with increasing crustal thickness at larger  $\delta'_c$  is 386 seen, as convection enters the thick crust limit. The turnover point, where Nusselt number begins declining 387 with increasing crustal thickness, occurs at different  $\delta_c'$  depending on the system's Rayleigh number and 388 Frank-Kamenetskii parameter. The crustal thickness must be larger at lower Rayleigh number before the 389 thick crust limit is reached. Likewise larger  $\theta$  also requires a larger crustal thickness before the thick crust limit is reached. These trends are consistent with the idea that the crust is unimportant for stagnant-lid 391 convection when it is much thinner than the lid thickness expected without a crust, and then begins to control the thickness of the lid at larger values. 393

The drop in Nusselt number with increasing crustal thickness means less efficient heat loss from the 394 mantle interior, and thus a rise in internal temperature (Figure 6). We thus see a general trend where mantle 395 internal temperature is constant for thin crustal layers, then internal temperature increases with increasing 396 crustal thickness in the thick crust limit. In the thin crust limit, where the crust does not significantly 397 impact convection, temperature is largely insensitive to Rayleigh number, but increases with increasing  $\theta$ , 398 as expected for stagnant-lid convection (Morris & Canright, 1984; Davaille & Jaupart, 1993; Solomatov, 1995; Grasset & Parmentier, 1998; Reese et al., 1998; Solomatov & Moresi, 2000; Korenaga, 2009). When 400 the crust controls the lid thickness, the internal temperature increases with increasing Rayleigh number. A higher Rayleigh number leads to a higher heat flux across the base of the mantle, which, combined with a 402 low surface heat flux due to the thick crust present, causes the mantle to warm (see §4.2).

## 404 3.1 Changing Buoyancy Number

With B = -1, we find that the buoyant crustal layer strongly resists sinking into the mantle, such that, when 405 thick enough, it can dictate the thickness of the lithosphere overall. With this buoyancy number, entrainment of the crust over time is also limited. However, the buoyancy number of the crust on real stagnant-lid planets 407 can vary, based on the density of the crust and the temperature difference across the mantle. We therefore explore how varying the buoyancy number of the crust in our models influences convection in the mantle 409 below. Larger in magnitude buoyancy numbers (that is, more negative) would mean larger positive buoyancy 410 forces for the crust, and hence would thus only enhance the effects already seen, namely that a thick crust 411 can suppress foundering at the base of the stagnant lid. However, lower in magnitude buoyancy numbers 412 may result in crusts with buoyancy forces too weak to suppress foundering at the lid base. We thus repeat 413 some of our model suites using buoyancy numbers of -0.7, -0.5, and -0.3, at a range of Rayleigh numbers. 414 The two main goals of these additional models are, first, to test whether entrainment of the buoyant 415 crustal layer occurs when smaller magnitude buoyancy numbers are used, and to quantify the rate of this 416 entrainment over time. If entrainment is fast on geologic timescales, it could reduce crustal thickness to the 417 point where the thick crust limit can not be reached, or where convection could only operate in this limit 418 for short time periods. The second is to test whether changing the buoyancy number significantly alters the 419 previously observed relationship between crustal thickness and Nusselt number, in particular when convection 420 is in the thick crust limit and if crustal entrainment is indeed significant. 421

We find that the buoyant crustal layer is slowly entrained by convection, at an approximately constant 422 rate over time, for buoyancy numbers with absolute value < 1. The rate of entrainment also increases with 423 decreasing absolute value of B (Figure 7; Table 6). These same trends hold for all models we ran, with different buoyancy numbers, Rayleigh numbers, and initial crustal thicknesses (see Table 6). In addition to 425 the effect of B on entrainment rate, we also find that entrainment rate generally increases with increasing Rayleigh number. We calculated average entrainment rates in our models by measuring the difference 427 between the initial and final (at the ending time of the model run) crustal thicknesses, and the elapsed time from when entrainment of the crust began. The average entrainment rate is then the difference between 429 initial and final crustal thicknesses divided by the elapsed time during which entrainment occurred. The highest non-dimensional entrainment rate we observed (for model parameters of  $Ra_0 = 5 \times 10^8$ , B = -0.3, 431  $\theta=13.82, \ {\rm and} \ \delta_{c0}^{'}=0.1), \ {\rm was} \approx -0.7869.$  Scaling this to a dimensional rate using the scaling factors 432 outlined in §2.1, we obtain  $\approx -2.7 \times 10^{-13}~\mathrm{m\cdot s^{-1}}$ , or  $\approx -8.6~\mathrm{m\cdot Myr^{-1}} = -8.6~\mathrm{km\cdot Gyr^{-1}}$ , for Earth's 433 thermal diffusivity and mantle thickness. For Mars, the entrainment rates would be larger by about a factor 434 of two, though Mars would also have a smaller Rayleigh number than Earth for the same mantle temperature

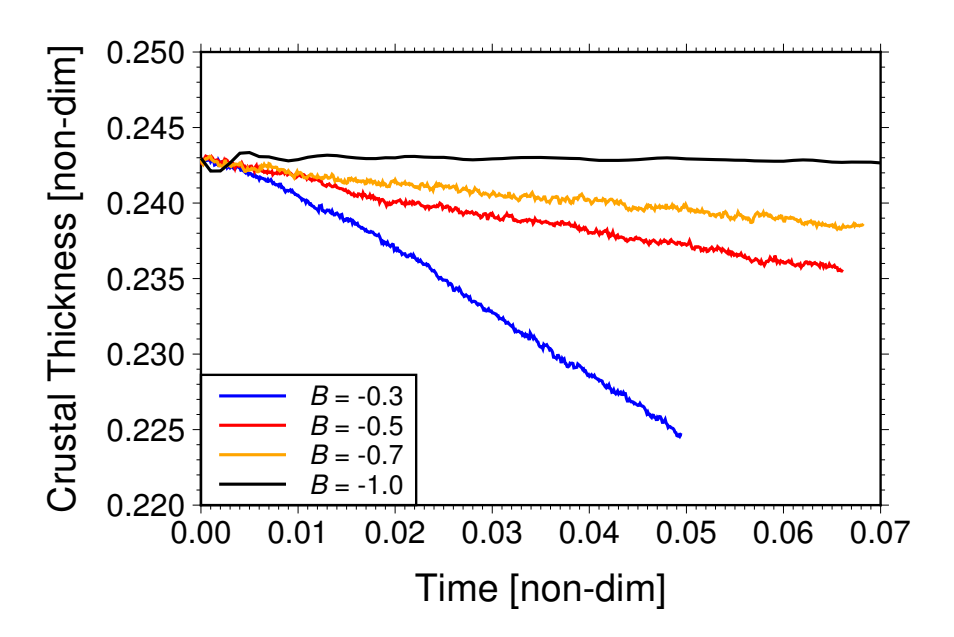


Figure 7: Buoyant crustal layer thickness as a function of time for models with  $Ra_0 = 10^8$  and the same initial buoyant crustal layer thickness,  $\delta'_{c0}$ . The models have different buoyancy number of B = -0.3 (blue), B = -0.5 (red), B = -0.7 (orange), and B = -1.0 (black). Time sampling was less frequent in the model with B = -1.0, so high frequency fluctuations are absent in the black curve. Lowering the buoyancy number magnitude clearly leads to larger entrainment rates.

and viscosity. It would therefore take hundreds of millions to billions of years for significant crustal loss, on the scale of  $\sim 10$  kilometers, to occur even in our most rapidly entraining models.

Despite the observed crustal entrainment with B = -0.7, -0.5 and -0.3, we find that models with 438 different buoyancy numbers, but the same Rayleigh number and Frank-Kamenetskii parameter, still fall 439 along the same crustal thickness-Nusselt number trend as models with B = -1.0 (Figures 8A & B). The buoyancy of the crust is still able to dictate lithosphere thickness and push convection into the thick crust 441 limit, even with lower in magnitude buoyancy numbers. The trends for mantle interior temperature as a 442 function of crustal thickness are less clear than for the Nusselt number, but again appear to be largely 443 insensitive to the buoyancy number, at least in the range of buoyancy numbers we tested (Figure 8C). In our 444 models where  $B \neq -1.0$  and therefore entrainment is non-negligible, no statistical steady-state is reached. 445 The Nusselt number and internal temperature will continue evolving as the crust is thinning. For these 446 models, we calculate time averages of Nu,  $T_i'$ , and  $\delta_c'$  over the final 25 timesteps of each model run (see §2.2); 447 these model end time averages are what is plotted in Figures 8A & C. 448

However, the ending point in our models is arbitrary, so we also plot Nusselt number as a function of crustal thickness for different timesteps during the model run, after the influence of the initial conditions on the model Nusselt number has been erased (Figure 8B). The timesteps plotted are at intervals of  $10^{-2} - 10^{-3}$  in non-dimensional units for  $Ra_0 = 10^7$ , and  $10^{-4}$  for  $Ra_0 = 10^8$  and  $5 \times 10^8$ . Figure 8B therefore shows

449

450

451

452

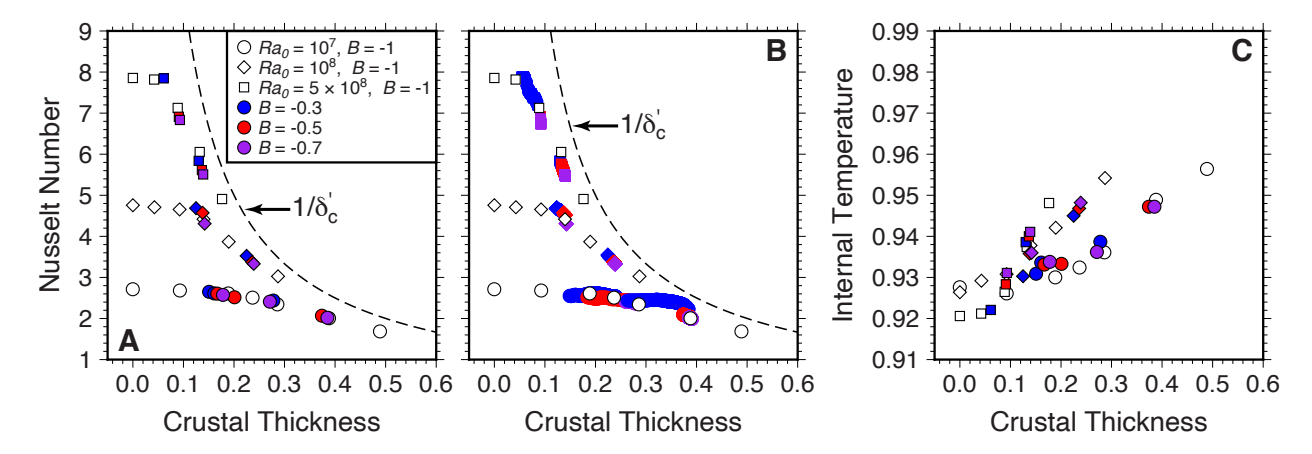


Figure 8: Nusselt number as a function of crustal thickness (A & B) and internal temperature as a function of crustal thickness (C) for models with  $\theta=13.82,\ Ra_0=10^7$  (circles),  $Ra_0=10^8$  (diamonds), and  $Ra_0=5\times 10^8$  (squares). Symbols are colored by the buoyancy number: B=-1.0 (white), B=-0.3 (blue), B=-0.5 (red), and B=-0.7 (purple). In Figures 8A & C, the Nu,  $T_i'$ , and  $\delta_c'$  plotted for  $B\neq -1.0$  are averages over the final 25 timesteps of the model run, because active crustal entrainment means a statistical steady-state is not reached in these models (see text for more details). In Figure 8B, Nusselt number and crustal thickness are plotted at multiple timesteps during the model runs with  $B\neq -1.0$ , to show how Nusselt number evolves as the crust thins due to entrainment. Specifically, results are plotted at timestep intervals of  $10^{-2}-10^{-3}$  in non-dimensional units for  $Ra_0=10^7$ , and intervals of  $10^{-4}$  for  $Ra_0=10^8$  and  $5\times 10^8$ . Finally, in Figures 8A & B the curve  $1/\delta_c'$  is shown, representing the maximum possible Nu in the thick crust limit (i.e. the conductive heat flux across a layer of thickness  $\delta_c'$  with a non-dimensional temperature difference of one).

how Nusselt number evolves as the crust thins due to entrainment. The results demonstrate that even as 453 the crust is thinning, the Nusselt number still follows the same trend as a function of crustal thickness, 454 with some fluctuation around this trend due to inherent time-dependence in convection. Entrainment does 455 not significantly change the scaling behavior, and thus the scaling laws we develop next, which give Nusselt 456 number as a function of crustal thickness, will hold even if entrainment is significant (as long as one knows 457 the actual crustal thickness at any given time). Moreover our arbitrary choice of end points to plot in Figures 458 8A & C is justifiable, as one could pick earlier timesteps in our models and still find that these points plot 459 along the same trend in  $\delta'_c - Nu$  space. 460

Our results show that entrainment rates are low on geologic timescales, even for low absolute value buoyancy numbers, and that the same scaling behavior is observed regardless of buoyancy number, even when the crust is actively thinning due to entrainment. Based on the entrainment rates seen in our models, crustal entrainment will not prevent a thick crust from forming, and a planet from entering the thick crust limit. Early in planets' histories when the mantle is hot and volcanism is extensive, crust formation is significantly faster than even the fastest entrainment rates we observe in our models (e.g. Hauck & Phillips, 2002; Fraeman & Korenaga, 2010; Morschhauser et al., 2011), so thick crusts can still form. Entrainment could cause crustal thinning when volcanism rates have waned due to mantle cooling, or after volcanism has

462

463

464

466

467

shut down entirely. A thinning crust would have an important influence on a planet's thermal evolution, because a thinner crust will lead to a higher heat flux for a given  $Ra_0$  and  $\theta$  in the thick crust limit, as our model results show. However, as long as one is able to track changes in crustal thickness over time, our scaling laws, developed below, can capture this effect (see §6). Moreover, the entrainment rates in our models are likely overestimates. Tackley & King (2003) show that entrainment rates in models using the tracer-ratio method, as ours do, are sensitive to grid resolution and the number of tracers employed, with higher resolution leading to lower entrainment rates. We thus expect that using higher resolution would lower the already small entrainment rates seen in our models.

An important remaining question is how small in magnitude the buoyancy number would have to be for 477 thermal bouyancy to dominate over the crustal layer's chemical buoyancy; in this situation entrainment rates 478 would likely be much higher, and the crust may be unable to ever grow thick enough for convection to enter the thick crust limit, or the thick crust limit would be very short-lived if reached. While a buoyancy number 480 of B = -1.0 (or absolute value of 1) would represent a situation where chemical and thermal bouyancy 481 forces are equal when the surface fully participates in convection, in the stagnant lid regime the temperature 482 difference actually driving convection is reduced by the factor  $1/\theta$  (e.g. Davaille & Jaupart, 1993; Grasset 483 & Parmentier, 1998; Reese et al., 1998; Solomatov & Moresi, 2000; Korenaga, 2009, see also §4.2). The 484 thermal buoyancy forces driving foundering at the base of the lid are thus also reduced by the same factor. 485 For thermal buoyancy to dominate over compositional buoyancy, the absolute value of the buoyancy number 486 would therefore likely need to be  $B < 1/\theta$ , or about 0.06 - 0.07 for the range of  $\theta$  used in our models. We 487 therefore expect that as long as the absolute value of the crustal buoyancy number is larger than  $\approx 1/\theta$ , then buoyancy forces are sufficient to allow convection to enter the thick crust limit, if the crust is thick enough. 489

## 490 3.2 Convective Stability of the Crust

When both the Rayleigh number and the buoyant crustal layer thickness are large, it is possible for the Rayleigh number of just the crustal layer to exceed the critical Rayleigh number for the onset of convection.

In this case, convection will occur in both the crust and underlying mantle separately (Richter & Johnson, 1974; Richter & McKenzie, 1981). We therefore examined the temperature and velocity fields in our models to determine if there is convection within the buoyant crustal layer or not. The large majority of the models do not show crustal convection (Figure 9); only those models with large reference Rayleigh numbers,  $Ra_0$ , and large initial crustal thicknesses,  $\delta'_{c0}$ , display crustal convection. Specifically, with  $\theta = 13.82$  we only observe crustal convection in cases when  $Ra_0 = 10^8$  and the initial crustal thickness is 0.35 or greater, and when  $Ra_0 = 5 \times 10^8$  and the initial crustal thickness is 0.2 or greater.

As the focus of this paper is on stagnant-lid planets where convection does not occur in the crust, because this situation is more geologically relevant as we show in §5.1, we exclude models where convection develops in the crust in Figures 5, 6, and 8, and the scaling analysis in §4.

We also observed different crustal dynamic states in two models with the same  $Ra_0 = 5 \times 10^8$  and  $\delta'_{c0} = 0.2$ , but different buoyancy numbers and different initial conditions (Figure 9). A model with B = -1.0 and an 504 initially static, conductive mantle and crust did not develop convection within the crust. However, crustal 505 convection did start in models with B = -0.7, B = -0.5, and B = -0.3 that used a fully developed convec-506 tion pattern, into which the buoyant crustal layer is inserted, as the initial condition. The different behavior 507 in the crust could be due to the different buoyancy numbers of those models. However, as buoyancy number 508 does not explicitly control convective stability of the crust (see §4.3), a more likely explanation is the differ-509 ence in initial condition. The initial conductive temperature profile produces cold temperatures in the crust, and therefore high viscosities which inhibit convection. Meanwhile starting from fully developed convection 511 produces warmer temperatures in the crust, thereby promoting convection. We only saw models with the same Rayleigh number and crustal thickness produce different states of crustal dynamics for conditions that 513 are very close to the boundary between non-convecting and convecting buoyant crustal layers. Hysteresis 514 at Rayleigh numbers very close to the critical Rayleigh number has been documented previously for fluids 515 with strongly temperature-dependent viscosity (Stengel et al., 1982; Richter et al., 1983; Solomatov & Barr, 516 2006, 2007). 517

# 518 4 Scaling Analysis

## 519 4.1 Nusselt Number

500

502

The numerical models indicate that there are two end member limiting behaviors: the thin crust and thick crust limits. Here scaling laws for the convective heat flux for both of these limits are derived. In the thin crust limit, convection behaves the same as isochemical stagnant-lid convection, where scaling laws for heat flux have been extensively studied. We thus provide a brief introduction to these scaling laws here, and fit them to our numerical convection model results.

Without a crust, scaling laws for Nusselt number in the high Rayleigh number, high Nusselt number limit (i.e. far from the critical Rayleigh number) for bottom heated convection typically take the form of (e.g. Morris & Canright, 1984; Fowler, 1985; Solomatov, 1995; Dumoulin et al., 1999; Reese et al., 1998;

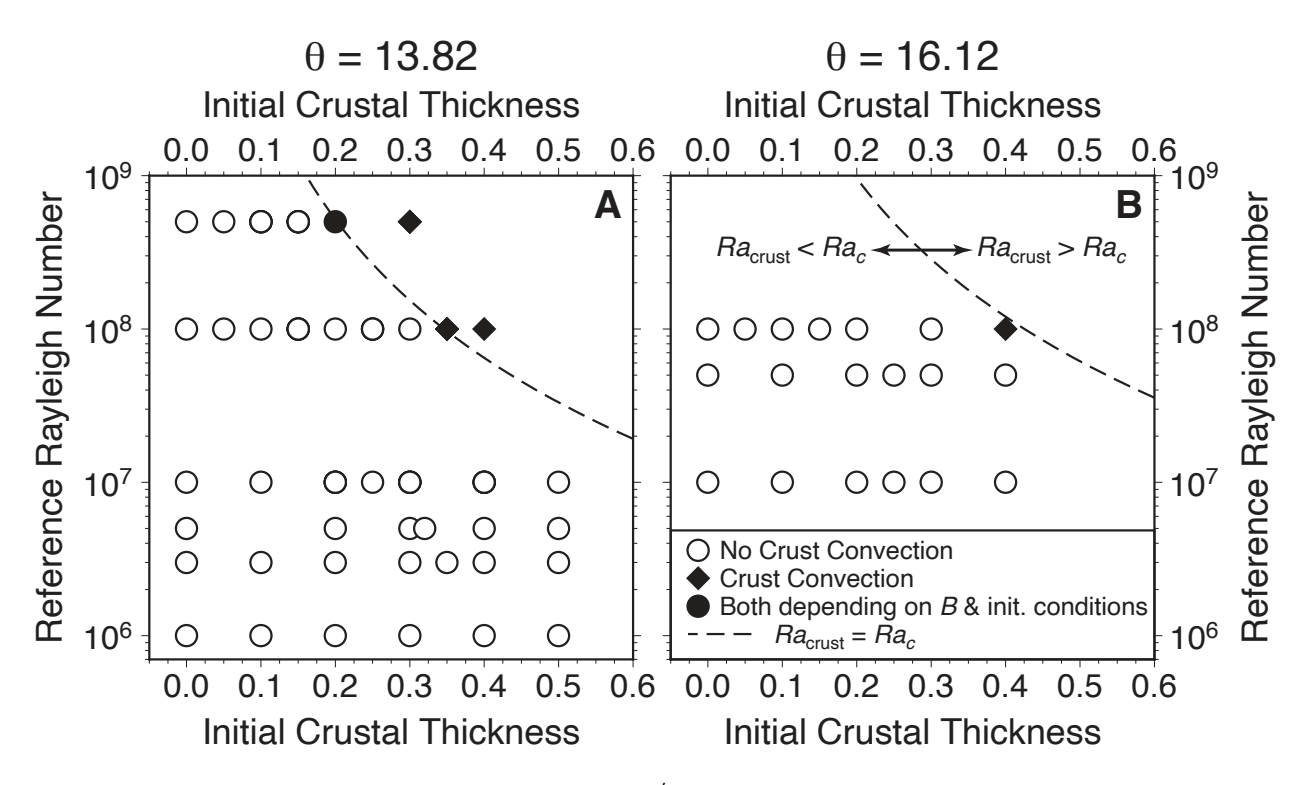


Figure 9: Regime diagram in initial crustal thickness ( $\delta'_{c0}$ )-reference Rayleigh number ( $Ra_0$ ) space, for Frank-Kamenetskii parameters of  $\theta = 13.82$  (A) and  $\theta = 16.12$  (B). Model results where no crustal convection was seen are indicated by white circles, while black diamonds indicate model results where crustal convection was observed. In some cases, models with the same  $Ra_0$  and  $\delta'_{c0}$  were run at different buoyancy numbers and with different initial conditions. The black circle indicates a case where both crustal convection and a static crust were seen in models at the same  $Ra_0 = 5 \times 10^8$  and  $\delta'_{c0} = 0.2$ , but with different B and initial conditions. The dashed line shows the theoretical curve for the onset of convection in the crust, developed in §4.3.

Solomatov & Moresi, 2000; Korenaga, 2009):

$$Nu = C^* \theta^{-(1+\beta)} R a_i^{\beta} \tag{8}$$

where  $C^*$  is a constant found empirically,  $\beta$  is the Nu-Ra scaling law exponent,  $Ra_i=Ra_0/\mu_i^{'}$  is the internal Rayleigh number, and  $\mu'_i$  is the average mantle interior viscosity, just beneath the stagnant lid. The average 530 interior viscosity can be calculated as the non-dimensional viscosity at  $T^{'} = T_{i}^{'}$ , giving  $\mu_{i}^{'} = \exp{(\theta(1 - T_{i}^{'}))}$ . 531 Note that this same form of the Nusselt number scaling law also holds for purely internally heated convection, 532 where the internal Rayleigh number is defined at the same average interior viscosity as given above, and the 533 temperature drop across the mantle is defined as the difference between the average interior temperature and surface temperature (e.g. Solomatov & Moresi, 2000; Korenaga, 2009). 535 Much work has then been devoted to determining the scaling law exponent  $\beta$ , from both theoretical studies, laboratory experiments, and numerical models. When the convection pattern is steady, both asymptotic 537 boundary layer theories and numerical experiments show that  $\beta \approx 1/5$ , and the scaling law takes the form (e.g. Morris & Canright, 1984; Fowler, 1985; Reese et al., 1998; Dumoulin et al., 1999; Solomatov & Moresi, 539 2000):

$$Nu = C_2 \theta^{-\frac{6}{5}} R a_i^{\frac{1}{5}}. (9)$$

On the other hand, when convection is time-dependent,  $\beta \approx 1/3$  (e.g. Solomatov, 1995; Dumoulin et al., 1999; Solomatov & Moresi, 2000; Korenaga, 2009), yielding:

$$Nu = C_1 \theta^{-\frac{4}{3}} Ra_i^{\frac{1}{3}}. (10)$$

To establish scaling laws for the thin crust limit, we fit our isochemical numerical convection models 543 (that is, models that lack a buoyant crustal layer) to the above scaling laws, Eqs. (9)-(10). As in Dumoulin 544 et al. (1999), we find that with increasing Rayleigh number, convection transitions from steady to time-545 dependent behavior (Figure 10A). We determine whether models are steady or time-dependent based on the standard deviations in Nusselt number and internal temperature, and visual inspection of the temperature 547 fields. There is a clear increase in standard deviations from negligably small values to values on the order of  $\sim 10^{-3}-10^{-4}$  at the switch from steady to time-dependent convection (Table 4), as well as a clear 549 switch from steady to time-dependent convection patterns when inspecting the temperature fields. We fit our numerical models where a steady-state convection pattern develops to Eq. (9), and our models where 551 convection is time-dependent to Eq. (10). From this, we find  $C_1 = 0.48$  and  $C_2 = 2.95$ , nearly identical to 552 the scaling laws from Dumoulin et al. (1999). We further find that our isochemical model results can be well 553

fit using 554

573

574

given by

$$Nu = \max\left(C_1 \theta^{-\frac{4}{3}} R a_i^{\frac{1}{3}}, C_2 \theta^{-\frac{6}{5}} R a_i^{\frac{1}{5}}\right),\tag{11}$$

also consistent with Dumoulin et al. (1999). That is, the transition from steady-state to time-dependent 555 convection occurs at approximately the point where Eq. (9) and Eq. (10) are equal.

Moore (2008) suggests Nusselt number scaling laws should have the form  $Nu-1=(Ra-Ra_c)^{\beta}$ , so that 557 Nusselt number converges to 1 as Rayleigh number approaches the critical Rayleigh number,  $Ra_c$ . However, as shown in Solomatov (1995), Nu also approaches 1 as  $Ra_i$  approaches the critical Rayleigh number in Eq. 559 (10). With  $Ra_c = 20.9\theta^4$  from (Solomatov, 1995, see also §4.3), Eq. (10) has the form  $Nu \sim (Ra/Ra_c)^{\beta}$ . A 560 scaling law with the form  $Nu-1=(Ra-Ra_c)^{\beta}$  converges to a scaling law with the form  $Nu\sim(Ra/Ra_c)^{\beta}$ 561 at high Rayleigh numbers, but shows different behavior at low Rayleigh numbers, despite both scaling laws 562 approaching Nu = 1 at  $Ra = Ra_c$ . The scaling law form of Moore (2008) shows a weaker dependence of 563 Nu on Ra at lower Rayleigh number, similar to lowering  $\beta$  in Eq. (8). As a result, the scaling law form 564 of Moore (2008) may even be able to fit both our steady and time-dependent model results with a single 565 value of  $\beta \approx 1/3$ . While this is attractive, no study carefully testing the  $Nu-1=(Ra-Ra_c)^{\beta}$  scaling 566 law form with stagnant-lid convection model results currently exists, so we use Eq. (9) & Eq. (10), which have been extensively tested. The goal of our study is not to develop new scaling laws for isochemical 568 stagnant-lid convection, but instead develop scaling laws for stagnant-lid convection with a thick, buoyant layer representative of the crust. As our models with a thin crust behave the same as models with no crust, 570 any scaling law that properly captures isochemical stagnant-lid convection could be used for the thin-crust limit, in place of Eq. (9) & Eq. (10) as used in this study. 572 As  $Nu = T_i'/\delta_0'$ , where  $\delta_0'$  is the thickness of the lithosphere due to purely thermal convection,  $\delta_0'$  is then

> $\delta_0' = \left(\frac{T_i'}{C_1}\right) \theta^{\frac{4}{3}} \left(\frac{Ra_0}{\mu_i'}\right)^{-\frac{1}{3}}$ (12)

for time-dependent convection at high Rayleigh number, and for steady convection at low Rayleigh number

$$\delta_{0}^{'} = \left(\frac{T_{i}^{'}}{C_{2}}\right) \theta^{\frac{6}{5}} \left(\frac{Ra_{0}}{\mu_{i}^{'}}\right)^{-\frac{1}{5}}.$$
(13)

We next develop scaling laws for the thick crust limit, where the thickness of the crust itself controls the 576 thickness of the stagnant lid. The Nusselt number in the thick crust limit will therefore be given by 577

$$Nu = \frac{T_i'}{\delta_{sl}' + \delta_c'},\tag{14}$$

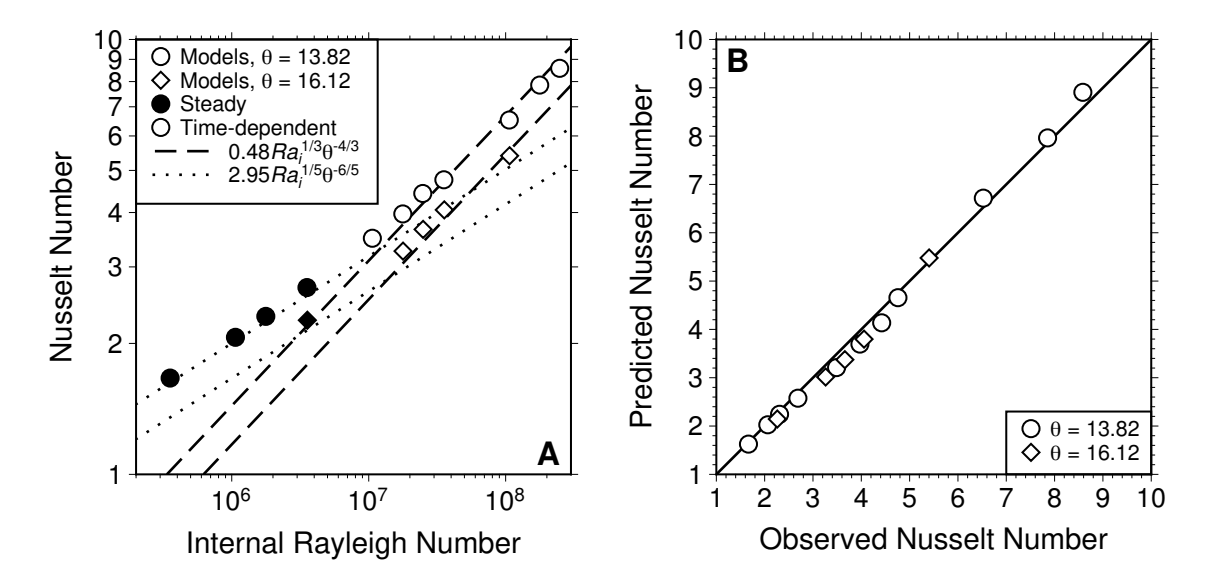


Figure 10: Nusselt number as a function of internal Rayleigh number for models without a crust (A), and comparison of iso-chemical stagnant-lid convection scaling law predictions to model results (B). Model results are used to determine the constants,  $C_1$  and  $C_2$ , in equations Eq. (10) and Eq. (9). Filled black symbols in Figure 10A denote model results where the convection pattern was steady, while open symbols denote time-dependent convection. See the main text for how models are classified as exhibiting steady or time-dependent convection.  $C_1$  is found by fitting the time-dependent models to Eq. (10), and  $C_2$  is found by fitting the steady convection models to Eq. (9).

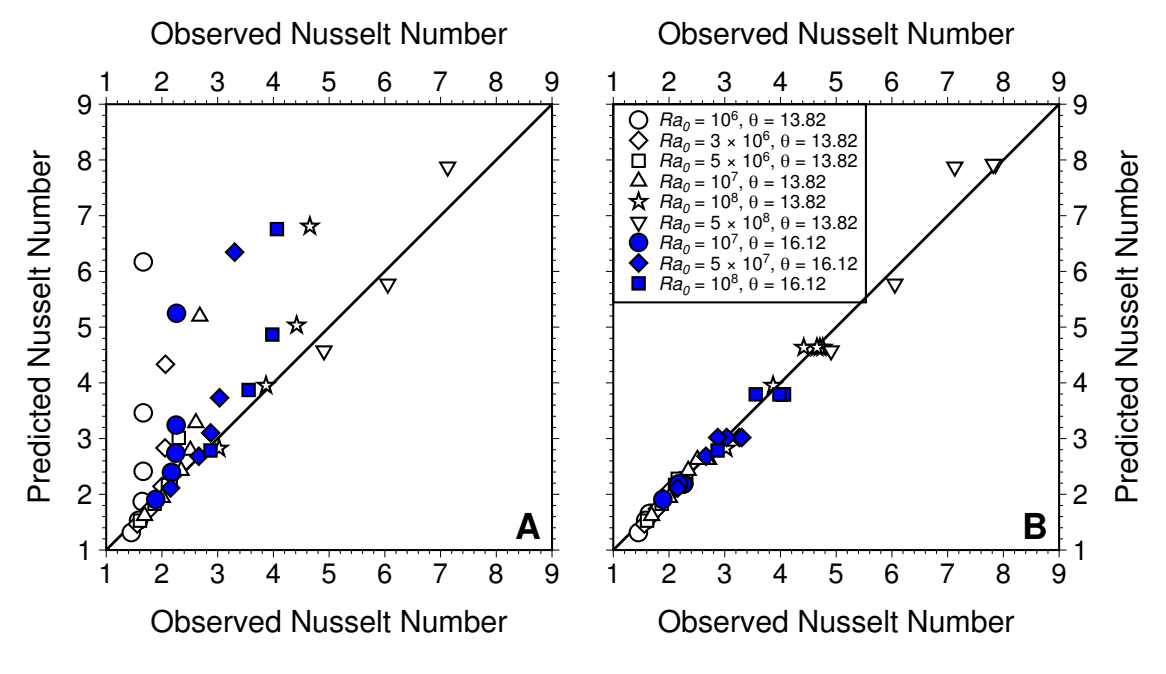


Figure 11: Scaling law for Nusselt number in the thick crust limit, Eq. (14) & Eq. (17), against the observed average Nusselt number from the numerical models (A). Predictions deviate from the model results at low crustal thickness, when the crust does not significantly influence convection and Nusselt number is given by standard thermal convection scaling laws, Eq. (9) & Eq. (10). Note that for models with a thin crust, or no crust, the thick crust limit scaling law predicts high Nusselt numbers, > 10, and these points plot off our scale in Figure 11. Scaling law for Nusselt number combining thick and thin crust limits Eq. (18) against observed Nusselt number from the numerical model results (B).

where  $\delta_{sl}^{'}$  is the thickness of a thermal boundary layer in the mantle just below the crust; we call this the subcrustal thermal boundary layer. The total thickness of the top thermal boundary layer is then  $\delta' = \delta'_c + \delta'_{sl}$ . A similar approach has been used successfully to describe heat flux through continents (Lenardic et al., 580 2005; Van Thienen, 2007); in these studies the total thickness of the conductive boundary layer is assumed to consist of the continent and mantle root, as well as a thermal boundary layer beneath the rigid continent. 582 We assume that the sub-crustal boundary layer follows a scaling law analogous to the rheological boundary layer in stagnant-lid convection. In this case, boundary layer thickness scales with Rayleigh number to 584 the -1/3 power, with the Rayleigh number defined based on the temperature difference across just the 585 active boundary layer, as this is the temperature scale driving convection (e.g. Solomatov, 1995). For the sub-crustal boundary layer, the temperature scale across this boundary layer is  $T_i' - T_c'$ , where  $T_c'$  is the 587 temperature at the crust-mantle interface. With these assumptions

$$\delta'_{sl} = \left(\frac{Ra_0(T_i^{'} - T_c^{'})}{Ra_c\mu_i^{'}}\right)^{-\frac{1}{3}},\tag{15}$$

where, as in Eqs. (12)-(13), we define Rayleigh number based on the mantle interior viscosity. We also include the critical Rayleigh number,  $Ra_c$ , in the denominator of Eq. (15), as in Lenardic et al. (2005), because 590 convection will not occur if the Rayleigh number is sub-critical. We find that this allows our numerical 591 models results to be well fit with  $Ra_c \approx 1000$  (see below). A critical Rayleigh number for constant viscosity 592 convection is used here, because the small temperature difference between  $T_i^{'}$  &  $T_c^{'}$  in the thick crust limit 593 results in approximately constant viscosity in the actively convecting mantle beneath the crust. In the thick 594 crust limit,  $T_i - T_c < \Delta T_{rh}$  where  $\Delta T_{rh}$  is the rheological temperature scale across the actively convecting 595 region in isochemical stagnant-lid convection, where viscosity variations are no greater than a factor of  $\approx 10$ (see §4.2). As our numerical models neglect internal heating and have a constant thermal conductivity 597 through the mantle and crust, we can assume a linear temperature profile through the lithosphere. With this assumption  $T_c^{\prime}$  follows 599

$$T_c^{'} = T_i^{'} \left( \frac{\delta_c^{'}}{\delta_{sl}^{'} + \delta_c^{'}} \right). \tag{16}$$

In §6 we show how  $T_c'$  can be calculated in the more general case, where heat production is not negligible in the crust and mantle, and the crust and mantle have different thermal conductivities. We also discuss how these additional factors would influence our derived scaling laws. Combining Eq. (15) & Eq. (16) and rearranging,

$$\frac{\delta_{sl}^{'4}}{\delta_{sl}^{'} + \delta_{c}^{'}} = \frac{Ra_{c}\mu_{i}^{'}}{Ra_{0}T_{i}^{'}}.$$
(17)

Equation (17) is solved numerically, using  $\delta_c^{'}$  and  $T_i^{'}$  values that are determined from each numerical con-

vection model as a post-processing step (see §2.2) when comparing the scaling law to model results.

Equation (17) shows that increasing internal Rayleigh number, either through an increase in  $Ra_0$  or a decrease in  $\mu_i^{'}$ , will lead to a thinner sub-crustal thermal boundary layer due to higher convective vigor in 607 the mantle. A larger  $\delta_c'$  causes a modest increase in  $\delta_{sl}'$ , due to a decrease in the temperature difference driving foundering of the sub-crustal thermal boundary layer,  $T_i^{'} - T_c^{'}$ , with increasing crustal thickness. We 609 note our scaling law for  $\delta'_{sl}$ , Eq. (17), implies that  $\delta'_{sl} \sim Ra_0^{-1/3}$  regardless of  $Ra_0$ , while our isochemical 610 numerical models were best fit by scaling laws implying  $\delta' \sim Ra_0^{-1/5}$  at low  $Ra_0$ , when the convection pattern 611 is steady. Despite this potential inconsistency, our scaling law for Nu in the thick crust limit fits the data 612 well, even at low Rayleigh number (Figure 11). The stagnant lid in the thick crust limit at low  $Ra_0$  appears 613 to have a flatter base than when the crust is absent (see Figure 1), and these flatter lid slopes might explain 614 why Eq. (17) produces an accurate scaling law even at low  $Ra_0$ . In addition, when the crust is very thick such that  $\delta_c' >> \delta_{sl}'$ , lithosphere thickness, and hence heat flux, are primarily controlled by crustal thickness. 616 Therefore our scaling law for Nu under these conditions is not strongly sensitive to how  $\delta'_{sl}$  scales with  $Ra_0$ . At large crustal thicknesses, i.e. in the thick crust limit, Eq. (14) & Eq. (17) provide a good fit to the 618 numerical model results (Figure 11A). However, as expected, the scaling laws fail to match the numerical 619 model results when the crust is thin, and the Nusselt number is approximately the same as for purely thermal convection. To account for this, we join the scaling laws for Nu in the thick crust and thin crust limits, as 621

$$Nu = \min\left(\frac{T_i'}{\delta_{sl}' + \delta_c'}, \max\left[C_1 \theta^{-\frac{4}{3}} \left(\frac{Ra_0}{\mu_i'}\right)^{\frac{1}{3}}, C_2 \theta^{-\frac{6}{5}} \left(\frac{Ra_0}{\mu_i'}\right)^{\frac{1}{5}}\right]\right), \tag{18}$$

from the numerical models with B = -1.0 shows a good match (Figure 11B). Thus the scaling laws are 623 accurate across a wide range of parameters and in both the thin and thick crust limits. However, right around the transition point between the thick and thin crust limits, the numerical model results do show a 625 relatively small deviation from the scaling laws (Figure 11B). This deviation is likely caused by the crust 626 disrupting the slopes that would form at the base of the stagnant lid in the isochemical case, and thereby 627 lowering the heat flux in a way our scaling laws do not capture. However, our scaling laws match the 628 thick and thin crust limits well, and the deviation described here is confined to a narrow range of crustal thicknesses. 630 An implicit assumption in our scaling laws is that the switch between the thin and thick crust limits occurs when the predicted Nusselt numbers from the two limits are equal, or equivalently when  $\delta'_c + \delta'_{sl} = \delta'_0$ . 632 The critical crustal thickness where convection transitions between these two limits is thus  $\delta_{c-\text{crit}}^{'}=\delta_{0}^{'}-\delta_{sl}^{'}$ .

where  $\delta'_{sl}$  is given by Eq. (17). Comparing our predicted Nusselt numbers from Eq. (18) to those measured

To test the preceding prediction using the numerical model results, we compare the Nusselt number of models

634

with a crust to the Nusselt number of the corresponding isochemical control case, that has the same  $Ra_0$  and  $\theta$ . We assume that the crust is significantly affecting convection, and thus the thick crust limit has been reached, at the crustal thickness where the Nusselt number first becomes > 5% lower than the Nusselt number for the corresponding isochemical control case.

For  $Ra_0 = 10^6$ , we find that the thickness of the stagnant lid in the control case is  $\delta'_0 = 0.55$ , using 639 equation Eq. (13) because with  $Ra_0 = 10^6$  a steady-state convection pattern develops. The crustal thickness where Nu is > 5% lower than the control case Nu was found to be  $\delta_c' = 0.3441$ . Using Eq. (15) with 641 the internal temperature of this model,  $T_i' = 0.9302$ , we calculate a sub-crustal thermal boundary layer 642 thickness of  $\delta_{sl}^{'}=0.2058$ . The critical crustal thickness where convection should enter the thick crust limit is thus  $\delta'_{c-\text{crit}} = 0.3442$ , nearly identical to the crustal thickness where we see a significant drop in the Nusselt 644 number. For  $Ra_0 = 10^8$ , Nusselt number first begins to significantly decrease with a crustal thickness of  $\delta_c^{'}=0.0925.$  Using Eq. (12) for this high Rayleigh number case, we estimate  $\delta_0^{'}=0.133,$  and, with a measured  $T_i^{'}=0.9308,$  find  $\delta_{sl}^{'}=0.0430.$  The critical crustal thickness for the onset of the thick crust limit is thus  $\delta'_{c-\text{crit}} = 0.09$ , again matching what was found in the numerical models. The scaling laws thus 648 successfully capture the transition between the thin and thick crust limits. 649

The models analyzed above all used B = -1.0. As discussed in §3.1, we also ran sets of models at 650 different buoyancy numbers of B = -0.7, B = -0.5, and B = -0.3. While these models display elevated 651 rates of crustal entrainment compared to the B = -1.0 models, the positive buouyancy of the crust still 652 dominates over the negative buoyancy of cool temperatures at the base of the lid, such that thick crusts 653 that dictate the overall thickness of the stagnant lid can still form. In addition, these models fall on the 654 same  $\delta'_c - Nu$  trend as the models with B = -1.0, indicating that the thickness of the buoyant crustal layer 655 still controls convective heat flux in the same way in the thick crust limit, even with progressively weaker positive buoyancy. Here we confirm that the models with varying buoyancy numbers also follow our scaling 657 law for Nusselt number, Equation (18) (Figure 12). 658

Our Nusselt number scaling law for convection with a buoyant crustal layer is therefore independent of the buoyancy number, as long as: 1) the buoyancy of the crust is strong enough for a thick crust to form and persist, which likely requires buoyancy numbers with absolute value  $> 1/\theta$ ; and 2) one knows and uses the actual crustal thickness present at a given time, taking into account crustal loss due to entrainment. In fact, our numerical models show that even when the crust is actively thinning due to entrainment, Nu scales with crustal thickness in the same way as our scaling laws predict (see §3.1). Our results therefore indicate that the buoyancy of the crustal layer itself does not influence the thickness of the subcrustal boundary layer, again as long as one considers the actual thickness of crust present at any given time. The buoyancy number influences the rate of entrainment, with less buoyant crust being easier to entrain. However, given

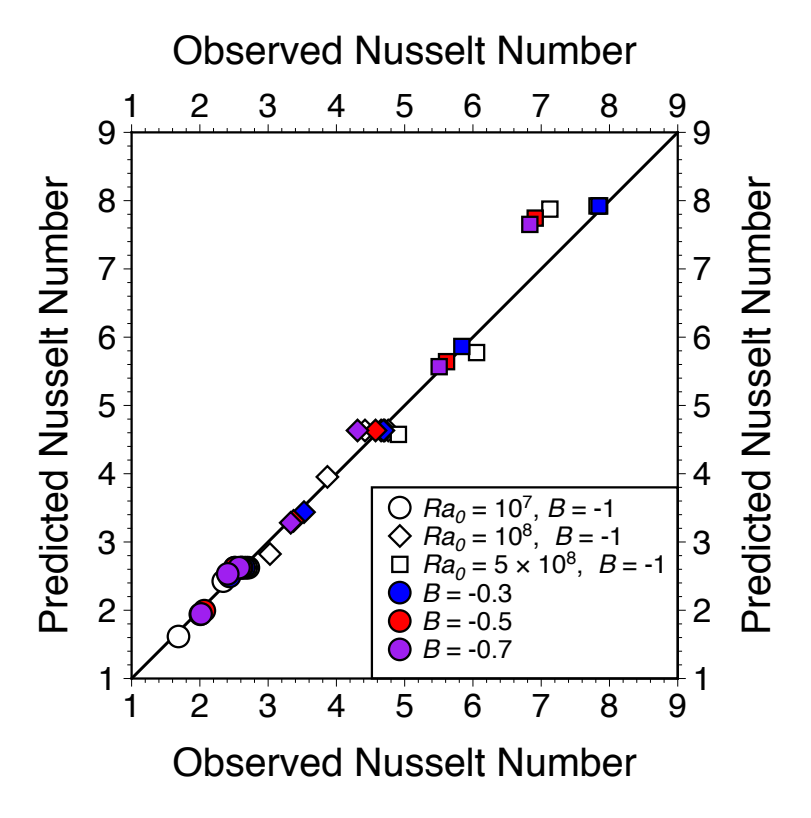


Figure 12: Predicted Nusselt number from our scaling law Eq. (18) against observed Nusselt number from numerical models with varying Rayleigh number and Buoyancy number. Symbols are the same as in Figure 8. Observed Nusselt numbers presented here for models with  $B \neq -1.0$  are averages at the end of each model run, as explained in §2.2 & 3.1.

that the entrainment rates seen in our models are slow on geologic timescales for both Earth and Mars sized planets, and that they are likely overestimates due to the significant numerical challenges involved in modeling physically accurate entrainment rates, we chose not to develop a scaling law for the entrainment rate. Such a task is best left for a study devoted to studying the physics of entrainment in detail.

## 4.2 Internal Temperature

In the thin crust limit, the internal temperature of the mantle is unaffected by the presence of the crust, and thus the same as for purely thermal stagnant-lid convection (e.g., Solomatov & Moresi, 2000; Reese & Solomatov, 2009). In this case, the non-dimensional temperature difference driving convection is  $\Delta T'_{rh} = a_{rh}/\theta$ , where  $a_{rh}$  is a constant (e.g. Davaille & Jaupart, 1993; Grasset & Parmentier, 1998; Reese et al., 1998; Solomatov & Moresi, 2000; Korenaga, 2009). With  $a_{rh} \approx 2$ , and with symmetry between the bottom boundary layer and top rheological boundary layer (i.e. the boundary layer beneath the stagnant lid),  $T'_i \approx 1 - \theta^{-1}$ , which matches our numerical model results well. We find  $T'_i \approx 0.925$  for  $\theta = 13.82$ , and  $T'_i \approx 0.935$  for  $\theta = 16.12$ ; these internal temperatures are approximately constant as  $Ra_0$  changes and for

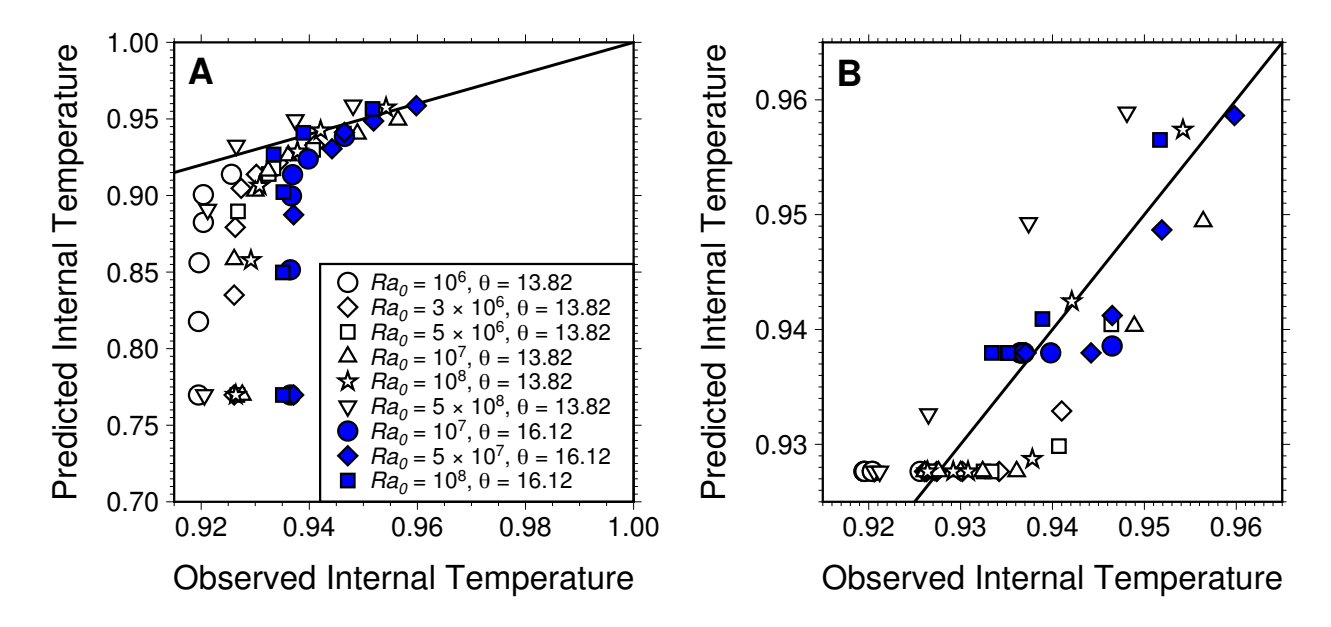


Figure 13: Internal temperature in the thick crust limit predicted by the scaling law Eq. (24), as a function of the observed internal temperature from the numerical model results (A). Predictions deviate from the model results when the crust is thin, and convection operates in the thin crust limit. Scaling law prediction for internal temperature combining the thick and thin crust limits (as explained in the text), against the observed internal temperature from the numerical models (B).

variations in crustal thickness within the thin crust limit (see §3 and Figure 6). However, when the crust is thick we observe an increase in mantle interior temperature with increasing crustal thickness. We thus develop a scaling law for the internal temperature in the thick crust limit, using a simple energy balance approach where we equate the heat flux into the base of the mantle and the heat flux leaving the top of the mantle. In terms of non-dimensional variables, heat flux into the bottom of the mantle,  $F'_{bot}$ , is:

$$F_{bot}^{'} = \frac{1 - T_i^{'}}{\delta_{bot}^{'}},\tag{19}$$

where  $\delta'_{bot}$  is the thickness of the boundary layer at the bottom of the mantle. The non-dimensional heat flux at the top of the mantle, the Nusselt number, is:

$$Nu = \frac{T_i'}{\delta'}. (20)$$

Equating these heat fluxes, we have

$$\frac{T_i^{'}}{\delta^{'}} = \frac{(1 - T_i^{'})}{\delta_{hot}^{'}},\tag{21}$$

which can be rearranged to give

$$\frac{\delta'_{bot}}{\delta'_c + \delta'_{sl}} = \frac{1 - T'_i}{T'_i},\tag{22}$$

where  $\delta^{'} = \delta^{'}_c + \delta^{'}_{sl}$  as we are considering convection in the thick crust limit.

702

703

705

706

707

708

711

714

We assume that  $\delta_{bot}'$  follows a scaling law analogous to that for the sub-crustal boundary layer Eq. (15):

$$\delta'_{bot} = C_3 \left( \frac{Ra_0(1 - T'_i)}{\mu'_i} \right)^{-\frac{1}{3}}, \tag{23}$$

where  $C_3$  is a constant. Empirically fitting our resulting scaling for internal temperature to the numerical results we find  $C_3 \approx 2$ . Combining equations (23) & (22),

$$\frac{1 - T_i'}{T_i'} = \left(\frac{C_3}{\delta_c' + \delta_{sl}'}\right) \left(\frac{\mu_i'}{Ra_0(1 - T_i')}\right)^{\frac{1}{3}}.$$
 (24)

In Eq. (24),  $\delta_{sl}'$  is given by Eq. (17). We thus have a system of two equations for the unknowns  $T_i'$  &  $\delta_{sl}'$ , which is solved numerically.

In the thin crust limit, internal temperature is unaffected by crustal thickness, and so our scaling law, 696 derived for the thick crust limit, naturally does not match the numerical model results (Figure 13A). The scaling law significantly underpredicts internal temperature because it assumes that crustal thickness dictates the thickness of the top thermal boundary layer. Thus, for thin crusts it predicts thin lithospheres and hence 699 low internal temperatures. However, with increasing crustal thickness, the internal temperatures predicted from the scaling law converge to the observed internal temperatures from the numerical models. 701

As with the scaling law for Nusselt number, we can combine the thin and thick crust limits into one scaling law, by taking the internal temperature to be the maximum of these limits (i.e. the maximum of  $T_i \approx 1 - \theta^{-1}$ for the thin crust limit, and  $T_i$  found from solving Eq. (24) for the thick crust limit). This combined scaling law matches the full set of numerical model results with B = -1.0 to first order, across both the thick and thin crust limits (Figure 13B). As with the scaling law for Nu, the fit to models where B is varied is of similar accuracy (not shown). In particular, the scaling law accurately predicts the magnitude of temperature increase with increasing crustal thickness in the thick crust limit, as numerical model results cluster around the line representing a perfect match between scaling law prediction and numerical model results. However, there is scatter around this trend line, indicating that the scaling law is slightly underpredicting the influence 710 of Rayleigh number or Frank-Kamenetskii parameter on internal temperature. In particular, there appears to be a stronger dependence of internal temperature on  $Ra_0$  than our scaling law predicts, so this is likely 712 the main source of error.

Also similar to our analysis for Nu, there is deviation between the scaling law and numerical convection model results near the transition between the thick and thin crust limits. Observed internal temperatures begin to increase with increasing crustal thickness before the scaling laws predict that they would enter the thick crust limit. This leads to data points plotting along a horizontal line in Figure 13B, at two different predicted temperatures depending on  $\theta$ . However, as crustal thickness increases further and models fall fully into the thick crust limit, the scaling law more accurately predicts the observed increase in temperature. Further refinement of this scaling law could improve the fit to the numerical models, both in the thick crust limit and in the transition region between the thick and thin crust limits. However, as scaling laws for internal temperature are not needed for modeling the thermal evolution of stagnant-lid planets, such further analysis is beyond this paper's scope.

One result of Eq. (24) is that internal temperature increases with increasing Rayleigh number in the thick 724 crust limit, as seen in the numerical results (see Figure 6). A higher Rayleigh number reduces the thickness of 725 the bottom thermal boundary layer, thereby increasing the heat flux into the bottom of the mantle. Although 726 a higher Rayleigh number also decreases the thickness of the sub-crustal thermal boundary layer, this effect is not enough to outweigh the influence of a higher basal heat flux, and interior temperature increases. The 728 reason for this is that as  $\delta'_{sl}$  gets thinner, the crust temperature,  $T'_c$ , gets warmer and hence the temperature difference driving foundering of the sub-crustal thermal boundary layer gets smaller. This makes  $\delta'_{sl}$  less 730 sensitive to  $Ra_0$  than the bottom thermal boundary layer. Changing  $\theta$  does not have a significant effect on 731 internal temperature in the thick crust limit in the numerical model results (see Figure 6), and the scaling 732 law reflects this. A larger  $\theta$  actually causes internal temperature to decrease slightly, the opposite of the 733 effect of  $\theta$  on internal temperature for purely thermal stagnant-lid convection. Again this is due to the 734 dynamics of the bottom thermal boundary layer; a larger  $\theta$  increases  $\delta'_{bot}$  and hence lowers the heat flux at 735 the base of the mantle. However, as  $\delta_c^{'}$  increases the effect of  $\theta$  becomes smaller, and models with the same Rayleigh number and crustal thickness converge towards the same internal temperature regardless of  $\theta$ . 737

### <sup>738</sup> 4.3 Onset of Convection in the Crust

For convection to occur in the crust, the Rayleigh number of just the buoyant crustal layer,  $Ra_{\text{crust}}$ , must exceed the critical Rayleigh number,  $Ra_c$ . The critical Rayleigh number for convection with a strongly temperature-dependent viscosity, where the viscosity at the base of mantle is used as the viscosity scale – as in our definition of  $Ra_0$  – is (Stengel et al., 1982; Richter et al., 1983; Solomatov, 1995):

$$Ra_c = 20.9\theta^4. \tag{25}$$

Defining the temperature at the base of the crust as  $T_c$ , the crustal Rayleigh number is:

$$Ra_{\text{crust}} = \frac{\rho g \alpha (T_c - T_s) \delta_c^3}{\kappa \mu(T_c)}$$
 (26)

where  $\delta_c$  is the crustal thickness. The crustal Rayleigh number can then be written in terms of the reference Rayleigh number of the mantle,  $Ra_0$ , and non-dimensional variables as:

$$Ra_{\text{crust}} = Ra_0 \left( \frac{\delta_{c0}^{'3} T_c'}{\exp(\theta(1 - T_c'))} \right), \tag{27}$$

where we have assumed  $\delta'_c = \delta'_{c0}$  as the onset of convection in the crust occurs early during a model's evolution, before significant crustal entrainment. 747

Intuitively, the theory demonstrates that increasing  $Ra_0$  or  $\delta'_{c0}$  will increase the crustal Rayleigh number, and can induce convection. A higher basal crustal temperature,  $T_c^{'}$ , also increases  $Ra_{crust}$  and favors 749 convection, while a larger Frank-Kamenetskii parameter for viscosity increases the critical Rayleigh number, and inhibits crustal convection.

To compare the theoretical estimate for the onset of convection in the crust to our numerical models, we calculate the crustal thickness where  $Ra_{\text{crust}} = Ra_c$  as a function of  $Ra_0$  and  $\theta$ . To calculate  $T'_c$ , we use Eqs. 753 (16) - (17) assuming a mantle interior temperature of  $T_i^{\prime} \approx 1$ , because mantle temperatures approaches one 754 as crustal thickness increases (see §4.2). The theoretical curve fits the numerical model results well, with 755 only some small deviation for the models with  $\theta = 16.12$  (Figure 9).  $Ra_{\text{crust}}$  is strongly sensitive to  $T'_c$ , so our 756 calculation for  $T_c^{'}$  is the most likely source of error. Estimating  $T_c^{'}$  requires assumptions about the structure 757 of convection in the underlying mantle, which may not hold for all models, especially those with different 758 initial conditions. Strong sensitivity of the boundary between convecting and non-convecting crustal layers to  $T_c^{'}$  is also consistent with our numerical model results, where initial conditions that produced warmer 760 temperatures at the base of the crust were more likely to induce convection than those that produced colder temperatures. Ultimately, crustal thickness on stagnant-lid planets will likely be limited by the transition of lower crust to dense eclogite, and foundering of this crust. As we show next in §5.1, when crustal thickness is assumed to be limited to the depth where eclogite forms, the crust is sub-critical for convection for a geologically relevant range of mantle interior temperatures and reference viscosities. 765

#### Application to Planetary Thermal Evolution 5

751

#### Conditions for planetary mantles to convect in the thick crust limit 5.1767

Our numerical models and scaling analyses show that when buoyant crusts grow as thick, or thicker, than the thickness of the stagnant lid that would have existed with no crust present, they suppress convective heat flux. These thick, buoyant crusts effectively increase the thickness of the stagnant lid, as the crust is too buoyant to sink into the mantle. However, as introduced in §1.1, there are processes that limit crustal

thickness, and thus may prevent crusts from growing thick enough for planets to enter the thick crust limit that our numerical models and scaling analyses explore. Heat producing elements partition into the crust, thereby lowering the heating power in the mantle (e.g. Hauck & Phillips, 2002; Fraeman & Korenaga, 2010; 774 Foley & Smye, 2018), partial melting depletes the mantle, increasing its solidus and therefore making further melting more difficult (e.g. Maaløe, 2004), the temperature at the base of the crust increases as the crust 776 grows thicker, which can lead to melting of the lower crust, and metamorphic reactions, in particular the 777 transition of basalt to eclogite, densify the lower crust and can cause it to founder into the mantle (e.g. Ito 778 & Kennedy, 1971; Hacker, 1996; Semprich et al., 2010; Jull & Kelemen, 2001; Taylor & McLennan, 2009; 779 Artemieva & Meissner, 2012; Baratoux et al., 2014). Heat producing element partitioning into the crust and 780 increases in mantle solidus upon depletion have been studied previously, and thick crusts capable of reaching 781 the base of the stagnant lid can still form, as explained in §1.1. However, the formation of eclogite could more stringently limit crustal thickness, as the dense eclogitized crust is likely to founder into the mantle. 783 We thus use our scaling laws developed in §4.1 to estimate here whether, and under what conditions, crusts thick enough for convection to enter the thick crust limit can form, when their thickness is limited by the 785 formation of eclogite. 786

Stagnant-lid planets produce crust through primary melting of the mantle, and hence the composition of
this crust is expected to be mafic. For mafic crusts, eclogite is the dense phase that forms at high pressure,
so we focus on eclogite here. The pressure where eclogite forms depends on temperature, water content,
and other factors (e.g. Ito & Kennedy, 1971; Hacker, 1996; Hacker et al., 2003; Semprich et al., 2010; Taylor
& McLennan, 2009; Artemieva & Meissner, 2012; Baratoux et al., 2014). For a mid-ocean ridge basalt
composition, the minimum pressure for eclogite formation given by Hacker (1996) is 1.2 GPa; we will use
this pressure in our analysis.

We first calculate the minimum crustal thickness needed for convection to enter the thick crust limit, 794  $\delta_{c-\text{crit}}$ . As outlined in §4.1,  $\delta_{c-\text{crit}} = \delta_0 - \delta_{sl}$ . We calculate  $\delta_{c-\text{crit}}$  for a range of mantle reference viscosities, 795 mantle interior temperatures, and for different planet sizes, as these are the key controlling parameters that 796 likely vary from planet to planet in the galaxy, or over a planet's history (Figure 14A & B). We assume pure 797 internal heating in this analysis, as real stagnant-lid planets are likely to contain a significant component of 798 internal heat production, as is the case for the Earth (e.g. Jaupart et al., 2015). When convection is purely 799 internally heated, it is unlikely to develop steady-state convection patterns, even at low Rayleigh numbers. Heat flux is thus found to scale as Eq. (10) for internally heated, isochemical stagnant-lid convection (e.g. 801 Solomatov & Moresi, 2000; Korenaga, 2009). That is, the steady-state convection scaling relationship of  $Nu \sim Ra^{1/5}$  is typically not seen. As a result we use Eq. (12) to calculate  $\delta_0$  regardless of Rayleigh 803 number here. Moreover, when convection is purely internally heated,  $\Delta T = T_i - T_s$ , as there is no thermal boundary layer at the base of the mantle. The internal Rayleigh number,  $Ra_i$ , is therefore defined as  $\rho g \alpha(T_i - T_s) d^3/(\kappa \mu(T_i))$ , and  $\theta = E_v(T_i - T_s)/(RT_i^2)$ .

Our numerical convection models were bottom heated, rather than internally heated. However timedependent, isochemical stagnant-lid convection follows the same Nusselt number-Rayleigh number scaling
law, Eq. (10), for both purely bottom heated and purely internally heated convection. Even the constant  $C_1$  is nearly unchanged: we find  $C_1 \approx 0.48$  for our bottom heated models, while Solomatov & Moresi (2000)
and Korenaga (2009) find  $C_1 \approx 0.5 - 0.55$  for their purely internally heated models. Moreover, Lenardic
et al. (2005) develop scaling laws for convection beneath continental lithosphere that are analogous to our
scaling laws for the thick-crust limit; they find these scaling laws hold for convection with internal heating.
Applying our scaling laws to internally heated planets should thus be at least first order accurate.

The following Arrhenius temperature-dependent viscosity law is used:

$$\mu = \mu_r \exp\left(\frac{E_v}{R} \left(\frac{1}{T_i} - \frac{1}{T_r}\right)\right) \tag{28}$$

where the reference viscosity of the mantle,  $\mu_r$ , is defined at the reference temperature  $T_r = 1650$  K,  $E_v = 300 \text{ kJ} \cdot \text{mol}^{-1}$  is the activation energy, and  $R = 8.314 \text{ J} \cdot \text{mol}^{-1} \cdot \text{K}^{-1}$  is the universal gas constant. All mantle temperatures discussed in this section are reported as potential temperatures, as it is differences in potential temperature that contribute to the thermal buoyancy forces driving convection, rather than absolute temperatures. We are also primarily interested in the mantle temperature just beneath the stagnant lid, as mantle properties here control instability at the base of the lid. The distinction between absolute and potential temperature is only important deeper in the interior, where adiabatic heating is significant.

Our numerical mantle convection models use a Frank-Kamenentskii approximation for the viscosity law, rather than the full Arrhenius law given above in Eq. (28). However, Korenaga (2009) showed that the same heat flux scaling law holds for either viscosity formulation, and only a small correction factor to the effective Frank-Kamenetskii parameter is needed when an Arrheinus viscosity law is used; this correction factor is beyond the scope of the simple first order calculations presented here. The correction factor results in slightly larger effective values of  $\theta$ , and hence lower Nu and larger  $\delta_0$ . Our calculations presented here therefore slightly underestimate  $\delta_0$ .

Finally, as in our numerical convection models, we also neglect differences in thermal conductivity between crust and mantle, and heat production in the crust and stagnant-lid. However, as we explain in §6, including these effects would only act to decrease the crustal thickness needed for convection to enter the thick crust limit, for a given mantle temperature. As a result, the calculations presented in Figure 14 are conservative, and the critical crustal thicknesses needed for convection to enter the thick crust limit shown are upper

bounds. The reason is that both effects increase the temperature at the base of the crust,  $T_c$ , and thus also increase the subcrustal boundary layer thickness,  $\delta_{sl}$ . With a thicker  $\delta_{sl}$ , the critical crustal thickness needed for convection to enter the thick crust limit is smaller, for a given  $\delta_0$ .

We solve for  $\delta_{c-\text{crit}}$  for an Earth-size (Figure 14A) and Mars-size planet (Figure 14B). For the Earth-size planet, we assume  $\rho = 4500 \text{ kg} \cdot \text{m}^{-3}$ ,  $g = 9.8 \text{ m} \cdot \text{s}^{-2}$ ,  $\alpha = 3 \times 10^{-5} \text{ K}^{-1}$ , and d = 2890 km. For the Mars-size 839 planet, we assume only the mantle density, gravity, and mantle thickness are different: we use  $\rho = 3500$  $kg \cdot m^{-3}$ ,  $g = 3.7 \text{ m} \cdot \text{s}^{-2}$ , and d = 1740 km (e.g. Zuber, 2001). We assume the same mantle thermal diffusivity 841 for Earth-size and Mars-size planets of  $\kappa = 10^{-6} \text{ m}^2 \cdot \text{s}^{-1}$ , which can be calculated from  $\kappa = k/(\rho_{\text{um}} c_p)$ , where 842 k is thermal conductivity,  $\rho_{\rm um}$  is upper mantle density, and  $c_p$  is heat capacity. Using  $k=5~{\rm W\cdot m^{-1}\cdot K^{-1}}$ 843  $\rho_{\rm um}=3300~{\rm kg\cdot m^{-3}},~{\rm and}~c_p=1250~{\rm W\cdot m^{-1}\cdot K^{-1}}$  for both Earth- and Mars-size planets,  $\kappa\approx 10^{-6}~{\rm m^2\cdot s^{-1}}.$ 844 Our estimate ignores variations in thermal diffusivity with pressure or temperature in the mantle, which could lead to slightly different average thermal diffusivities for Earth-size and Mars-size planets. For all models 846 presented in this section, surface temperature,  $T_s$ , is fixed to  $T_s = 273$  K. A complete list of parameters and variables used for the calculations here in §5.1-5.2 can be found in Table (3). 848

We find that the higher the mantle temperature and lower the reference viscosity, the thinner the critical 849 crustal thickness needs to be for convection to enter the thick crust limit. A higher mantle temperature also 850 decreases the buoyancy number, for a given crust-mantle chemical density difference, making crust easier to 851 entrain. However, entrainment rates are slow on geologic timescales for all our numerical convection models, 852 and the compositional density difference between the crust and mantle would have to be very small (< 10 853 kg·m<sup>-3</sup>) for thermal buoyancy to dominate over the positive chemical buoyancy of the crust and drive more 854 rapid entrainment (see §3.1 & 6). It is thus easier for planetary mantles to operate in the thick crust limit 855 when reference viscosity is low or mantle temperature is high. For an Earth-size planet, crusts less than 30 km thick will still be thick enough for convection to be in the thick crust limit, and hence to suppress 857 convective heat flux, if  $T_i > 1800$  K at  $\mu_r = 10^{18}$  Pa·s, or  $T_i > 2000$  K at  $\mu_r = 10^{19}$  Pa·s. Higher mantle 858 temperatures and lower reference viscosities lead to more vigorous convection and hence a thinner  $\delta_0$ . The 859 thinner  $\delta_0$ , the thinner the crust can be and still dictate the overall thickness of the lithosphere. However, 860 with decreasing mantle temperature or increasing reference viscosity,  $\delta_{c-\text{crit}}$  rapidly increases, to very large 861 thickness of  $>\sim 100$  km. Such thick crusts are unlikely to form in reality due to the transition of basalt 862 to eclogite, as we show next. For a Mars-size planet the same trends hold, but  $\delta_{c-\text{crit}}$  is everywhere larger. A Mars-size planet has lower  $\rho$  and g, which decreases convective vigor and increases  $\delta_0$  for a given mantle 864 temperature and reference viscosity. As a result, a thicker crust is needed for convection to enter the thick crust limit. 866

As crusts thick enough for the lower crust to transition to eclogite are dynamically unstable, and unlikely

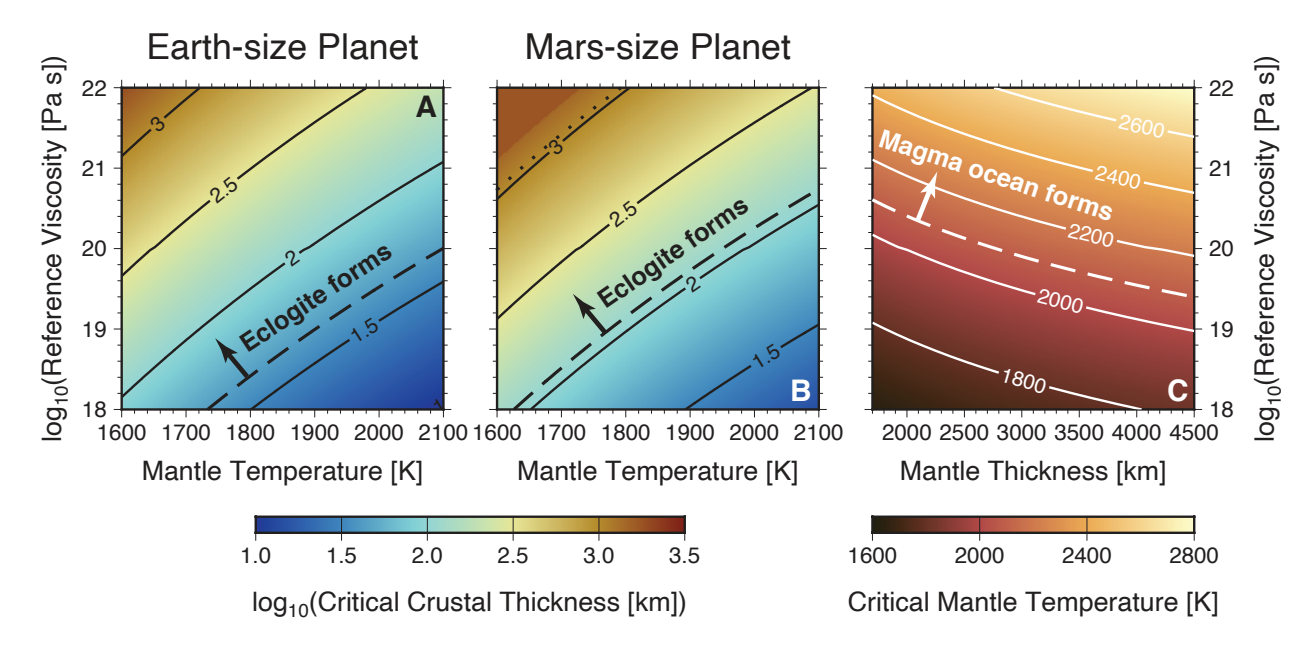


Figure 14: The critical crustal thickness needed for convection to enter the thick crust limit,  $\delta_{c-\text{crit}}$ , for an Earth-size planet as a function of internal temperature and mantle reference viscosity (A). Dashed contour line at 43 km (or  $\log_{10}{(43)} = 1.63$ ) is the depth where eclogite forms. Therefore, it may not be possible for the crust to grow thicker than  $\approx 43$  km. The critical crustal thickness needed for convection to enter the thick crust limit for a Mars-sized planet (B). For this size planet the depth where eclogite forms is  $\approx 116$  km, (or  $\log_{10}{(116)} = 2.06$ ). Above the dotted line in the upper left corner our scaling laws predict convection would cease. (C) Critical mantle temperature,  $T_{i-\text{crit}}$ , required for convection to be in the thick crust limit as a function of mantle thickness and reference viscosity, when the crust is assumed to extend to the depth where eclogite forms. Above the dashed contour line at  $\approx 2100$  K, the mantle would experience complete melting beneath the stagnant lid, and therefore effectively form a magma ocean. For all the results shown here we confirmed that the crust would be subcritical for convection, using the critical Rayleigh number for stagnant-lid convection given in Solomatov (1995).

to persist over geologic timescales, we assume that the maximum plausible crustal thickness,  $\delta_{c-\text{max}}$ , is set by
the depth where eclogite forms. With a pressure where eclogite forms of  $P_{\text{ecl}} = 1.2 \text{ GPa}$ ,  $\delta_{c-\text{max}} = P_{\text{ecl}}/(\rho_c g)$ ,
where  $\rho_c = 2800 \text{ kg} \cdot \text{m}^3$  is the density of the crust. For an Earth-size planet we find  $\delta_{c-\text{max}} \approx 43 \text{ km}$ , and for a
Mars-size planet  $\delta_{c-\text{max}} \approx 116 \text{ km}$ . These maximum crustal thickness limits are plotted on Figures 14A & B
as dashed lines. When  $\delta_{c-\text{crit}} < \delta_{c-\text{max}}$ , as found for high mantle temperatures and low reference viscosities,
then crusts thick enough for convection to enter the thick crust limit can plausibly form. However, when  $\delta_{c-\text{crit}} > \delta_{c-\text{max}}$ , it is unlikely that convection will ever be able to enter the thick crust limit, because the
formation of dense eclogite will prevent crusts from growing thick enough to reach  $\delta_{c-\text{crit}}$ .

For an Earth-size planet, convection will be unlikely to ever enter the thick crust limit for the majority 876 of the range of plausible reference viscosities and internal temperatures we considered, unless crusts can 877 grow thicker than the nominal depth where eclogite forms (Figure 14A). However, for a Mars-size planet, 878  $\delta_{c-\text{crit}} < \delta_{c-\text{max}}$  for a larger range of  $\mu_r$  and  $T_i$ . Convection can therefore enter the thick crust limit for a 879 wider range of conditions on a Mars-size planet than on an Earth-size planet. Although the critical crustal thickness needed for convection to enter the thick crust limit increases due to lower  $\rho$  and g, the lower g881 also means the depth where eclogite forms increases. As  $\delta_{c-\text{max}}$  scales linearly with g, while  $\delta_0$  scales as 882  $(\rho g)^{1/3}$ ,  $\delta_{c-\text{max}}$  increases more rapidly than  $\delta_{c-\text{crit}}$ . The thick crust limit is therefore more likely to be seen 883 on smaller planets than on larger ones. 884

To more completely explore the influence of planet size, we calculate the critical mantle temperature,  $T_{i-\text{crit}}$ , needed for convection to enter the thick crust limit, for a crustal thickness equal to  $\delta_{c-\text{max}}$  (Figure 14C). We calculate  $T_{i-\text{crit}}$  for a range of mantle reference viscosities and mantle thicknesses. We use the same methodology and assumptions, outlined above, as we used to calculate  $\delta_{c-\text{crit}}$ . To scale mantle properties  $\rho$ , g, and d with planet size, we use the scaling laws developed by Valencia et al. (2006, 2007):

$$\rho = \rho_{\bigoplus} \left(\frac{M}{M_{\bigoplus}}\right)^{0.2} \tag{29}$$

$$g = g_{\bigoplus} \left(\frac{M}{M_{\bigoplus}}\right)^{0.5} \tag{30}$$

$$d = d_{\bigoplus} \left(\frac{M}{M_{\bigoplus}}\right)^{0.28} \tag{31}$$

where M is planet mass. Equations (29)-(31) assume an approximately Earth-like core mass fraction.

891

893

894

The lower the critical mantle temperature for convection to enter the thick crust limit, the more likely it will be for planets to convect in this regime, because it means this regime will be found for a broader range of mantle temperatures. Planets are also likely to spend a larger fraction of their lifetime in the thick crust

Table 3: Parameters and variables used in  $\S 5.1\text{--}5.2$ 

Parameter	Meaning	Assumed value	Equation
$\mu_r$	Reference viscosity	$10^{18} - 10^{22} \text{ Pa·s}$	(28)
$T_r$	Reference mantle potential temperature	$1650~\mathrm{K}$	(28)
$E_v$	Viscosity activation energy	$300 \text{ kJ} \cdot \text{mol}^{-1}$	(28)
R	Universal gas constant	$8.314 \text{ J} \cdot \text{mol}^{-1} \cdot \text{K}^{-1}$	(28)
$T_s$	Surface temperature	$273 \mathrm{~K}$	below $(28)$
$\alpha$	Thermal expansion coefficient	$3 \times 10^{-5} \ \mathrm{K}^{-1}$	below $(28)$
$\kappa$	Thermal diffusion coefficient	$10^{-6} \text{ m}^2 \cdot \text{s}^{-1}$	below $(28)$
ho	Average mantle density (Earth)	$4500 \; {\rm kg \cdot m^{-3}}$	below $(28)$
ho	Average mantle density (Mars)	$3500 \ {\rm kg \cdot m^{-3}}$	below $(28)$
ho	Average mantle density (General planet size)	=	(29)
g	Gravity (Earth)	$9.81 \ \mathrm{m \cdot s^{-2}}$	below $(28)$
g	Gravity (Mars)	$3.71 \text{ m} \cdot \text{s}^{-2}$	below $(28)$
g	Gravity (General planet size)	=	(30)
d	Mantle thickness (Earth)	$2890~\mathrm{km}$	below $(28)$
d	Mantle thickness (Mars)	$1740~\mathrm{km}$	below $(28)$
d	Mantle thickness (General planet size)	<del>-</del>	(31)
$P_{ m ecl}$	Pressure where eclogite forms	1.2  GPa	below $(28)$
$ ho_c$	Average crust density	$2800 \ {\rm kg \cdot m^{-3}}$	below $(28)$
k	Thermal conductivity (Earth and Mars)	$5 \text{ W} \cdot \text{m}^{-1} \cdot \text{K}^{-1}$	(32)
$V_{man}$	Volume of the mantle (Mars)	$1.4 \times 10^{20} \text{ m}^3$	(33)
$c_p$	Heat capacity	$1250 \text{ J} \cdot \text{kg}^{-1} \cdot \text{K}^{-1}$	(33)
$A_s$	Surface area of planet (Mars)	$1.4 \times 10^{14} \text{ m}^2$	(33)
$Q_0$	Initial heat production rate	25  or  50  TW	(33)
$ au_{rad}$	Radioactive decay constant	$2.94 \mathrm{\ Gyrs}$	(33)
Variable	Meaning	Units	Equation
$\overline{q}$	Heat flux	$W \cdot m^{-2}$	(32) & (33)
$T_i$	Potential temperature of the mantle interior	K	(32) & (33)
$\mu$	Viscosity of the mantle	$Pa \cdot s$	(28)
t	Time	$\mathbf{S}$	(33)

limit, when  $T_{i-\text{crit}}$  is lower. As expected based on Figures 14A & B, we find that  $T_{i-\text{crit}}$  decreases with decreasing planet size or reference viscosity. For a planet with a Mars-like mantle thickness and  $\mu_r = 10^{18}$  Pa·s,  $T_{i-\text{crit}} \approx 1600$  K. However, for a planet with  $\mu_r = 10^{18}$  and d = 4500 km,  $\approx 1.5$  times thicker than Earth's mantle,  $T_{i-\text{crit}} > 1800$  K.  $T_{i-\text{crit}}$  then increases sharply with increasing reference viscosity, as with larger reference viscosities the stagnant lid thickness produced by convection without a crust increases significantly, when all else is held fixed. The mantle would then have to be very hot for convection to enter the thick crust limit, when crustal thickness is limited to the depth where eclogite forms.

For very high mantle temperatures, extensive melting would occur. If melt fractions are larger than  $\approx 60$ 903 \%, then the molten region will deform like a liquid, rather than like a solid (Solomatov, 2015). A large region 904 of the mantle experiencing such extensive melting would then behave more like a magma ocean than the 905 solid state mantle convection our models and scaling analyses apply to. To estimate the mantle temperature where such magma ocean-like behvaior would develop, we estimate the minimum temperature where the 907 mantle exceeds the liquidus at the base of the lid, using the liquidus of Katz et al. (2003); this temperature is found to be  $T_i \approx 2100$  K. For  $\mu_r > 4 \times 10^{20}$  Pa·s and d = 1700 km, the mantle can not get hot enough 909 to ever enter the thick crust limit, without leading to complete melting of the mantle, unless crust can grow 910 thicker than the depth where eclogite forms. For d=4500 km this limit is lower;  $\mu_r < 2.5 \times 10^{19}$  Pa·s for 911 convection to ever reach the thick crust limit, with our assumed maximum plausible crustal thickness. 912

Our results therefore indicate that the thick crust limit is more likely to be seen on small planets, and planets with hot interiors and low reference viscosities. The formation of a thick, buoyant crust could thus significantly impact the thermal evolution of such planets. Meanwhile, on large planets or planets with high reference viscosities, the thick crust limit is unlikely to ever be reached, and hence the positive buoyancy of the crust can be ignored in modeling such planets' thermal evolution.

913

914

915

916

917

However, even for smaller planets, where a broader range of conditions allow convection to operate in 918 the thick crust limit, thermal evolution modeling is necessary to determine how large an impact a thick, 919 buoyant crust would have on such planets' thermal histories, and for how long convection would remain in 920 the thick crust limit once entered. In particular, factors that promote convection entering the thick crust 921 limit, smaller planet size and lower reference viscosity, also enhance the rate of mantle cooling, when all else 922 is equal. It is therefore unclear how long such planets would remain in the thick crust limit. Initial mantle 923 temperature and planetary heat budget will also be important, as planets most prone to entering the thick crust limit may need high rates of internal heating, or significant stores of primordial heat, for convection to 925 remain in the thick crust limit for an extended period of time. More rapid cooling on smaller planets may also keep them from forming thick crusts in the first place. However, previous models for Mars show that 927 thick crusts (>≈ 100 km) can form when mantle reference viscosity is low or heat production rate is high

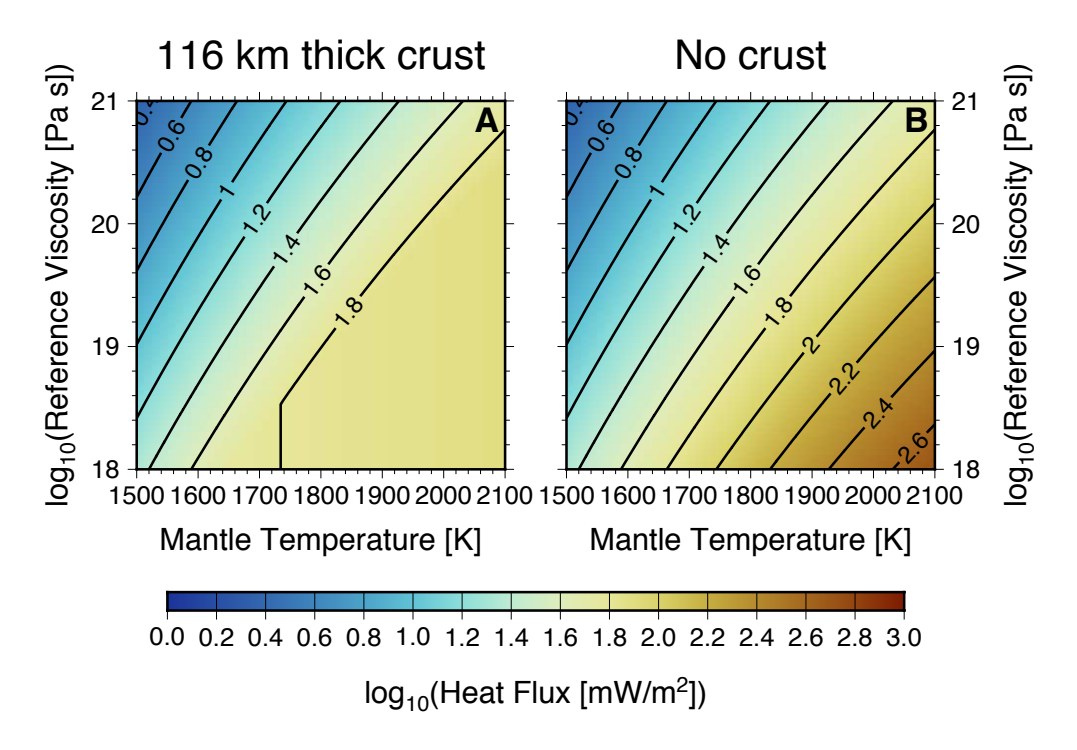


Figure 15: Heat flux for a Mars-sized planet with a 116 km thick crust, which is the limit where eclogite would form, as a function of mantle interior temperature and reference viscosity (A), and the heat flux for the same conditions but where the influence of the crust is ignored (B).

(e.g. Hauck & Phillips, 2002; Fraeman & Korenaga, 2010); low reference viscosity further leads to the crust forming rapidly, within ~ 100 Myrs (Fraeman & Korenaga, 2010). So the same conditions that make a small planet more prone to entering the thick crust limit, based on our scaling analysis, also promote the rapid formation of a thick crust. The thick crusts seen in these models (at extreme end-member values of reference viscosity or heat production rate) are probably not realistic for Mars based on geophysical observations (Wieczorek & Zuber, 2004; Goossens et al., 2017), but demonstrate the potential relevance of the thick crust limit to planets with different interior properties and heat budgets. We therefore present a set of simple parameterized convection models next, in order to explore these effects further.

#### 5.2 Thermal evolution modeling

937

943

Here we present simple thermal evolution models of a Mars-size planet that incorporate our newly developed scaling laws. We chose a Mars-size planet to model because smaller planets are more likely to enter the thick crust limit, when the maximum crustal thickness is set by the depth where eclogite forms; the effect of crustal buoyancy on mantle convective heat flux will thus be most pronounced for this size planet.

We first demonstrate how a thick, buoyant crust influences convective heat flux by calculating heat flux as a function of the average mantle interior temperature,  $T_i$ , and mantle reference viscosity,  $\mu_r$ , for a case

where the crust is  $\approx 116$  km thick and a case where no crust is present (Figure 15). A crustal thickness of 116 km is used because this is the maximum thickness possible before the eclogite transition would be reached on a Mars-size planet. We calculate heat flux, q, based on our scaling law for Nusselt number, Eq. (18), employing all of the same assumptions as outlined above in §5.1. We assume time-dependent, internally heated convection and therefore remove the scaling law for steady-state convection. The scaling law for heat flux used in this section is thus

$$q = \min\left(\frac{k(T_i - T_s)}{\delta_{sl} + \delta_c}, C_1 \frac{k(T_i - T_s)}{d} \theta^{-\frac{4}{3}} R a_i^{\frac{1}{3}}\right).$$
(32)

The definitions of internal Rayleigh number,  $Ra_i$ , and Frank-Kamenetskii parameter,  $\theta$ , are the same as given in §5.1. We also assume the same material properties for a Mars-size planet,  $\rho = 3500 \text{ kg} \cdot \text{m}^{-3}$ , g = 3.7951  ${\rm m\cdot s^{-2}},\ d=1740\ {\rm km},\ T_s=273\ {\rm K},\ \alpha=3\times 10^{-5}\ {\rm K^{-1}},\ \kappa=10^{-6}\ {\rm m^2\cdot s^{-1}},\ {\rm and}\ k=5\ {\rm W\cdot m^{-1}\cdot K^{-1}}\ ({\rm Table}\ 3).$ As in §5.1 and in our numerical convection models, we neglect differences in thermal conductivity between 953 the crust and mantle, and enrichment of heat producing elements in the crust. Although these assumptions were already justified above, additional discussion is warranted here. Including the effects of heat producing 955 element enrichment and a lower thermal conductivity in the crust would change the geotherm there, leading to warmer temperatures at depth. However, in standard thermal evolution models that ignore the crust's 957 buoyancy, or when the crust's buoyancy is negligible (i.e. in the thin crust limit), this modified crustal geotherm does not influence mantle convective heat flux in the stagnant lid regime (e.g. Hauck & Phillips, 2002). Mantle convective heat flux is dictated by the heat flux across the rheological sublayer at the base of 960 the stagnant lid in the thin crust limit (e.g. Solomatov, 1995). In this case, the temperature drop across the rheological sublayer is entirely controlled by  $\theta$  and  $\Delta T = T_i - T_s$ , as  $\Delta T_{rh} \sim \Delta T/\theta$ , while the thickness of the 962 rheological sublayer is controlled by  $\theta$  and  $Ra_i$  (e.g. see §4). Both  $\theta$  and  $Ra_i$  are functions of mantle interior properties, mainly temperature and, for  $Ra_i$ , viscosity, and not affected by the geotherm within the crust. 964 The total surface heat flux would be influenced, as the surface heat flux would be the sum of the heat flux supplied to the base of the stagnant lid by the convecting mantle, and the heat produced within the crust. However, it is the mantle convective heat flux that controls mantle thermal evolution, and therefore this is the heat flux we present in Figure 15. Our estimate of the heat flux in the thin crust limit will therefore not be affected by neglecting enrichment of heat producing elements and a lower thermal conductivity in the crust. 970 In the thick crust limit, the crustal geotherm will influence mantle convective heat flux, as the temperature 971 difference across the subcrustal boundary layer is a function of the temperature at the base of the crust,  $T_c$ . Hence the thickness of the subcrustal boundary layer,  $\delta_{sl}$ , is also a function of  $T_c$ . As explained below

in §6, including heat producing element enrichment and a lower thermal conductivity in the crust both 974 act to increase  $T_c$ . As a result, the temperature difference driving foundering of the subcrustal boundary layer,  $T_i - T_c$ , shrinks and  $\delta_{sl}$  increases. Including heat producing element enrichment and a lower thermal 976 conductivity in the crust would therefore lower mantle convective heat flux in the thick crust limit, beyond what the calculations presented here show. Moreover, as explained above in §5.1, these same factors would 978 make it easier for convection to enter the thick crust limit in the first place. The lower mantle convective heat flux brought about by a warmer  $T_c$  would then feedback on the mantle interior temperature during a planet's 980 thermal evolution. Neglecting heat producing element enrichment and variations in thermal conductivity in 981 the crust are thus conservative assumptions for the heat flux calculations presented in Figure 15; including these effects would only accentuate the influence of crustal buoyancy on mantle heat flux illustrated here. However, these same effects would have a more complicated effect on a planet's mantle thermal history, in particular heat producing element partitioning into the crust, which lowers the heating power in the mantle 985 as discussed further below.

When the mantle temperature is low or the reference viscosity is high, there is no difference in convective 987 heat flux between the no crust case and the 116 km thick crust case (Figure 15), because convection operates in the thin crust limit at these conditions. The base of the stagnant lid extends far deeper than the base of the crust. However, for mantle temperatures > 1600 K at  $\mu_r = 10^{18}$  Pa·s, or > 1950 K at  $\mu_r = 10^{20}$ Pa·s, convection operates in the thick crust limit. In this situation, convective heat flux is substantially 991 suppressed by the presence of the crust: heat flux is held to  $\approx 60-65 \text{ mW}\cdot\text{m}^{-2}$ , and only weakly decreases 992 with decreasing mantle potential temperature or increasing reference viscosity, with a 116 km thick crust. 993 Meanwhile, if no crust is present, heat flux reaches  $\approx 400 \text{ mW} \cdot \text{m}^{-2}$  for  $T_i = 2100 \text{ K}$  and  $\mu_r = 10^{18} \text{ Pa·s}$ . As 994 a result, the presence of a thick, buoyant crust will suppress convective heat flux early in a planet's history, if mantle reference viscosity is lower than  $\sim 5 \times 10^{20}$  Pa·s and the initial mantle temperature is  $\approx 2100$ 996 K. As reference viscosity decreases, this suppression of heat flux by a thick crust extends to lower mantle temperatures, and can thus persist longer during a planet's thermal evolution. 998

To illustrate how suppression of convective heat flux by a thick, buoyant crust influences a stagnant-lid planet's thermal history, we next perform a set of simple parameterized convection models. We employ all the same assumptions and material property values as given above, which results in the following equation for the evolution of mantle temperature (e.g. Davies, 2007; Spohn, 1991; Foley & Smye, 2018)

$$\rho V_{man} c_p \frac{\mathrm{d}T_i}{\mathrm{d}t} = A_s q - Q_0 \exp\left(-\frac{t}{\tau_{rad}}\right). \tag{33}$$

Mantle heat flux, q, is calculated from Eq. (32) as in Figure 15,  $V_{man}$  is the volume of the mantle,  $c_p = 1250$ 

 $J \cdot kg^{-1} \cdot K^{-1}$  is the heat capacity, and  $A_s$  is the surface area of the mantle. Initial mantle heat production rates,  $Q_0$ , of 11.7, 25, and 50 TW are used. The first two are the heat production rates derived from the compositional models of Wanke & Dreibus (1994) and Lodders & Fegley (1997), respectively, while the last represents a planet enriched in heat producing elements beyond what is seen in the solar system. Such enrichment in radionuclide abundances are possible for exoplanets, because large system to system variations in heat producing element abundances are seen in stars (e.g. Unterborn et al., 2015; Botelho et al., 2019), and thus likely to be reflected in any planets orbiting these stars. The decay constant,  $\tau_{rad} = 2.94$  Gyrs, is calculated based on a weighted average of the four major heat producing elements (Driscoll & Bercovici, 2014; Foley & Smye, 2018). We run sets of models with assumed crustal thicknesses of 0 km (no crust), 58 km (half the depth to the eclogite transition), and 116 km (at the depth of the eclogite transition), reference viscosities ranging from  $\mu_r = 10^{18} - 10^{20}$  Pa·s, and with initial mantle interior temperatures of  $T_{\rm init} = 1800$ K and  $T_{\text{init}} = 2100 \text{ K}$  (Figure 16). 

Only mantle heat loss by solid-state convection is considered in these thermal evolution models. We thus neglect heat loss due to mantle melting and eruption, which could be significant when mantle temperatures are high. We also hold the crustal thickness fixed in time; this is justifiable if the crust forms rapidly, as is thought to be the case for Mars (e.g. Nimmo & Tanaka, 2005). Furthermore, if the formation of eclogite ultimately limits crustal thickness, then the base of the crust will remain fixed over time at the depth where eclogite forms, after an initial period of crust growth to this depth. Finally, as before, heat producing element partitioning into the crust is ignored. The influence of these simplifications on the results presented here is discussed further in §6. Though there are competing effects, in particular with heat producing element enrichment in the crust, in sum we expect that our model simplifications lead to an overestimate of mantle temperatures, particularly in the thick crust limit. The mantle temperatures presented below should therefore be taken as upper bounds.

With the lower initial heat production rate of  $Q_0 = 11.7$  TW (Figures 16A, C, & E), decreasing reference viscosity leads to a greater influence of crustal buoyancy on the thermal history. With an initial mantle temperature of  $T_{\rm init} = 2100$  K and reference viscosity  $\mu_r = 10^{20}$  Pa·s, only the thickest crust case enters the thick crust limit, leading to a very small increase in mantle temperature during the first  $\approx 3$  Gyrs of evolution compared to the no crust case. However, with  $\mu_r = 10^{18}$  Pa·s, both the 116 km and 58 km thick crust models enter the thick crust limit, leading to elevated mantle temperatures during the first  $\approx 2$  and  $\approx 4-5$  Gyrs, respectively. The buoyancy of the crust acts to suppress convective heat flux during these time periods (Figure 17E), thereby causing mantle temperatures to run hotter. As the mantle cools and the thickness of the stagnant lid increases, planets transition into the thin crust limit, and begin cooling more rapidly. The mantle temperature histories thus eventually converge, regardless of the imposed crustal thickness. However,

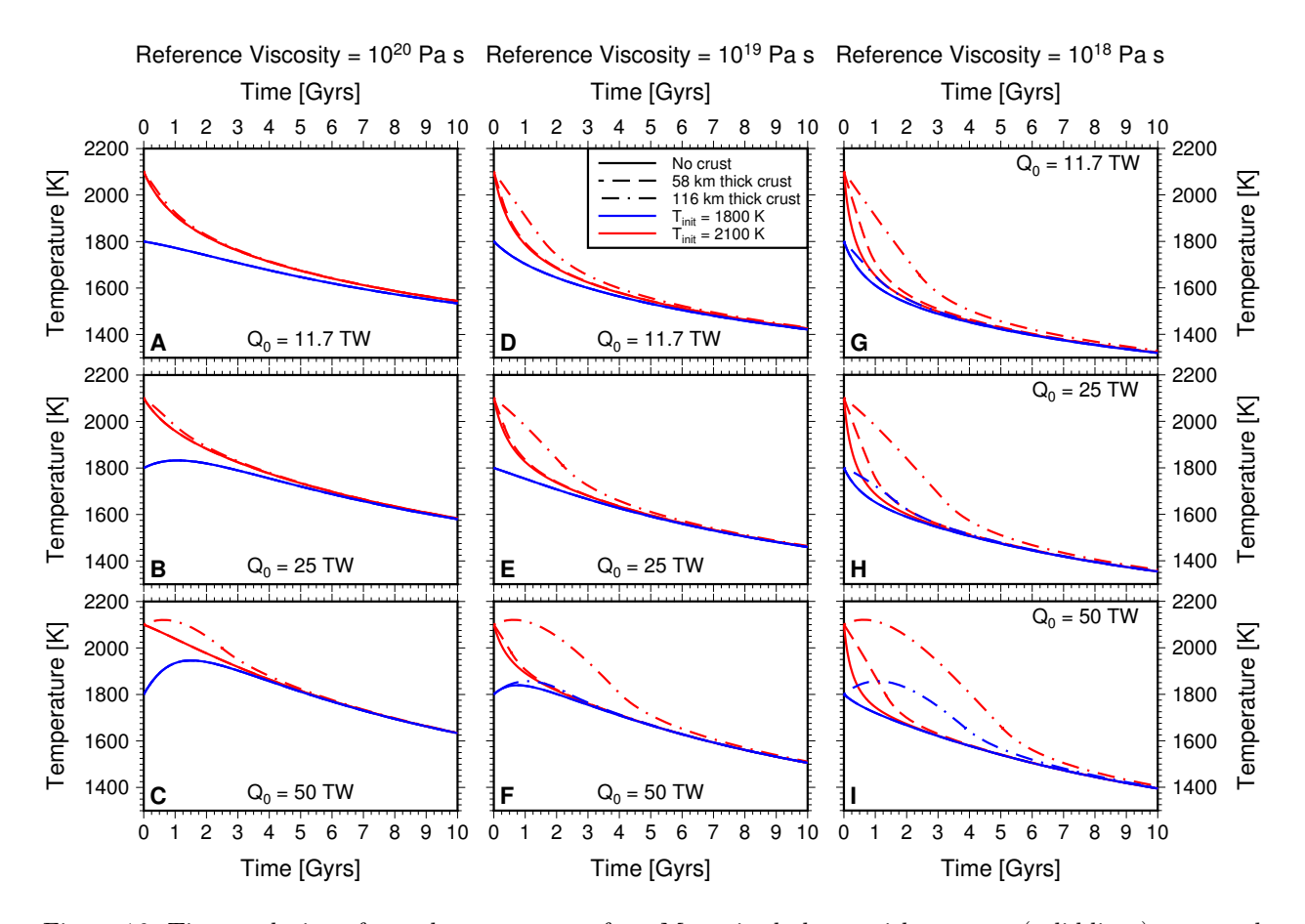


Figure 16: Time evolution of mantle temperature for a Mars-sized planet with no crust (solid lines), a crustal thickness of 58 km (dashed lines), and a crustal thickness of 116 km (dot-dashed lines). The latter two crustal thicknesses correspond to pressures at the base of the crust that are halfway to, and equal to, the pressure where eclogite forms, respectively. Initial mantle temperatures are either 1800 K (red) or 2100 K (blue). Three different reference viscosities are shown,  $10^{20}$  Pa·s (A,B,C),  $10^{19}$  Pa·s (D,E,F), and  $10^{18}$  Pa·s (G,H,I). Models assume a total initial radiogenic heating rate of 11.7 TW (top row; A, D, & G), 25 TW (middle row; B, E, & H) or 50 TW (bottom row; C, F, & I).

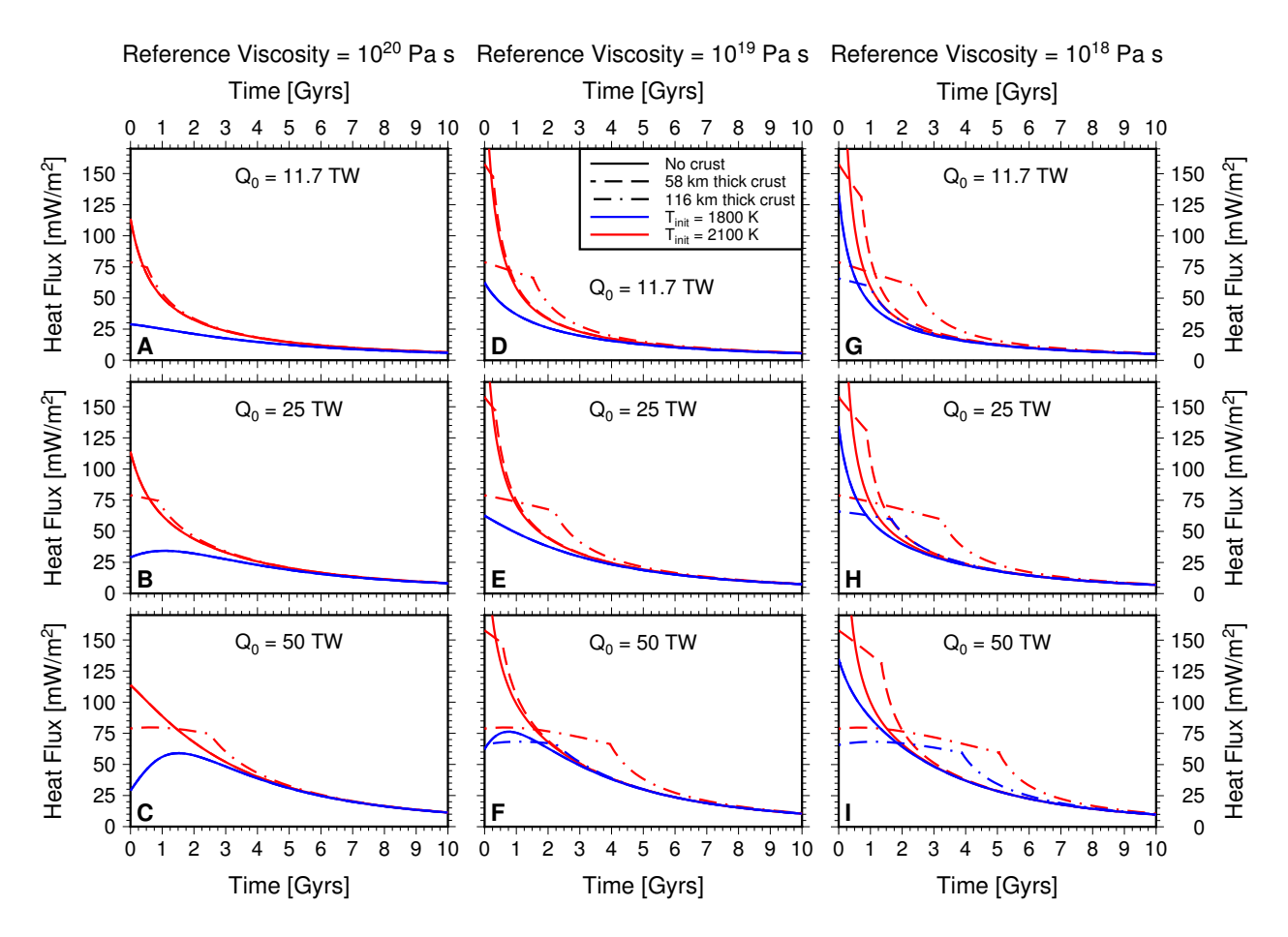


Figure 17: Time evolution of mantle convective heat flux for the same models shown in Figure 16.

this convergence can be very slow: with  $T_{\rm init}=2100$  K,  $\mu_r=10^{18}$  Pa·s, and a crustal thickness of 116 km, convection remains in the thick crust limit for  $\approx 2.5$  Gyrs, and elevated mantle temperatures persist for  $\approx 5-6$  Gyrs. Mantle temperatures are  $\approx 200-250$  K higher during the first 1-2 Gyrs of evolution for this model, in comparison to the no crust case. However, note that the simplifications made in our model set up mean we may overestimate this elevation in mantle temperature, and how long these elevated temperatures last.

With  $T_{\rm init} = 1800$  K, convection only enters the thick crust limit when the crust is 116 km thick and  $\mu_r = 10^{18}$  Pa·s. The mantle temperature in this case is only elevated by a few tens of degrees above the no crust case, and converges to the no crust case after  $\approx 2-3$  Gyrs. The buoyancy effects of a thick crust can thus accentuate differences in initial conditions, and allow the influence of different initial conditions to persist for multiple Gyrs, even longer than the age of our solar system in some cases. The higher the initial mantle temperature, the easier it is for convection to begin in the thick crust limit. As a result, mantle heat flux is suppressed, meaning this additional primordial heat supplied by the higher initial temperature is also more easily retained and contributes to long-lasting, elevated mantle temperatures. The buoyancy of a thick crust therefore acts to weaken the thermostat, or Tozer, effect that tends to regulate mantle thermal histories (Tozer, 1967, 1972), because mantle convective heat flux in the thick crust limit is far less sensitive to mantle temperature than isochemical convection (Figure 15). The lower the reference viscosity and thicker the crust, the longer it takes for initial conditions to be erased during mantle thermal evolution. 

The same trends hold with a higher initial heat production rates of 25 & 50 TW (Figures 16B, E & H and 16C, F & I, respectively). With a higher heat production rate, mantle temperatures are generally higher and it is thus easier for models to enter the thick crust limit. Moreover, models that enter the thick crust limit experience more pronounced, and longer-lasting, periods of elevated mantle temperatures during their early histories. With  $Q_0 = 50$  TW,  $T_{\rm init} = 2100$  K and  $\mu_r = 10^{18}$  Pa·s, mantle temperatures are  $\approx 500$  K greater during the first 1-2 Gyrs of evolution with a 116 km thick crust than if no crust were present (Figure 16F). Elevated temperatures then last for  $\approx 8-9$  Gyrs in this case. Even with a cooler initial temperature of  $T_{\rm init} = 1800$  K, the 116 km thick crust case reaches temperatures  $\approx 150$  K hotter than the no crust case, and elevated temperatures last for 5-6 Gyrs. Higher internal heating rates therefore accentuate and prolong the effects of crustal buoyancy on mantle thermal evolution. As a result, the higher the initial internal heating rate, the more the Tozer feedback is weakened, and the longer it will take for the influence of the initial mantle temperature to be erased during a planet's thermal evolution.

Crust formation has potentially removed half of the Martian mantle's initial heat producing element abundance (Plesa et al., 2018; Thiriet et al., 2018). Such depletion of heat producing elements in the mantle would thus mean that our model with  $Q_0 = 50$  TW would effectively have  $\approx 25$  TW of initial heating

power in the mantle once crustal formation has occurred, and thus may behave more like that case (i.e., 1070 Figures 16B, E, & H). Or put another way, the mantle, before crust formation, would need to have  $\approx 100$ 1071 TW of initial heating power to follow the thermal histories presented in Figures 16C, F, & I. As we discuss 1072 in more detail in §6, though, there are effects cutting back the other way. Heat production in the crust lowers mantle convective heat flux in the thick crust limit even more than our simple model estimates, by 1074 changing the crustal geotherm. In addition, the rate of crust growth will be important, as the thicker the 1075 crust the stronger the influence on mantle thermal history. A thick crust that grows slowly will lead to less 1076 pronounced elevation of mantle temperatures compared to a case where the same crust grows very rapidly. 1077 The thick crust limit could potentially be avoided altogether if crust growth is very slow. However, the same 1078 factors that lead to a significant influence from a thick, buoyant crust (low mantle reference viscosities, high 1079 mantle temperatures or rates of internal heat production) also lead to extensive mantle melting and faster 1080 crust growth. 1081

1082

1083

1084

1085

1086

1087

1088

1089

1090

1092

1093

1094

1095

1096

1097

1098

1099

1101

The time evolution of mantle convective heat flux also illustrates the same trends as the mantle temperature histories (Figure 17). Here, the way a thick crust limits mantle heat flux early in a planet's history is clearly illustrated, as well as the transition from the thick crust to thin crust limits, which shows up as a kink in the mantle heat flux versus time curve. In the thick crust limit, the weak dependence of mantle heat flux on mantle temperature causes it to evolve far more slowly than in the thin crust limit, or than in the cases where no crust is present; this further highlights the way the Tozer feedback is weakened by a thick, buoyant crust. Without a crust, mantle heat fluxes converge to the same trend after 1-2 Gyrs with a low reference viscosity, and after 3-4 Gyrs with a high reference viscosity, regardless of initial mantle temperature due to the Tozer feedback. After the effect of initial conditions is erased, mantle heat flux largely follows the mantle heat production rate. With a thick crust, this convergence does not happen until the mantle cools to the point that convection evolves into the thin crust limit. With no crust, mantle heat fluxes are within the range of 13-16 mW·m<sup>-2</sup> after 4.5 Gyrs for  $Q_0 = 11.7$  TW, compared to  $\approx 17 - 18$  mW·m<sup>-2</sup> in Hauck & Phillips (2002), 20-23 mW·m<sup>-2</sup> for  $Q_0 = 25$  TW, and 32-36 mW·m<sup>-2</sup> for  $Q_0 = 50$  TW. With a thick crust, mantle heat flux after 4.5 Gyrs can be higher, due to suppression of early mantle cooling. The highest seen is for the case with  $T_{\rm init}=2100$  K,  $\mu_r=10^{18}$  Pa·s, and  $Q_0=50$  TW, where mantle heat flux after 4.5 Gyrs is  $\approx 63 \text{ mW} \cdot \text{m}^{-2}$ .

Geophysical constraints indicate Mars' reference viscosity is larger than  $10^{18}$  Pa·s, in the range of  $10^{21}$  –  $10^{22}$  Pa·s (e.g. Plesa et al., 2018; Samuel et al., 2019). Combined with an initial heat production rate of no larger than 25 TW, with most geophysical models (e.g. Hauck & Phillips, 2002; Plesa et al., 2018) favoring the 11.7 TW derived from Wanke & Dreibus (1994), and an estimated crustal thickness of  $<\approx 80$  km (e.g. Wieczorek & Zuber, 2004), crustal buoyancy likely did not play a significant role in Mars' thermal evolution.

temperature evolution. However, extrasolar planets with different compositions could have lower reference 110 viscosities or higher abundances of heat producting elements, such that formation of a thick, buoyant crust 1105 could significantly impact their evolution. For example, a mantle composed of pure favalite (an iron rich 1106 mantle) is ~ 1000 times less viscous than a pure forsterite (or iron poor) mantle (e.g. Zhao et al., 2009), while 1107 preliminary constraints on heat producing element budgets in other stars show abundances up to at least 1108 2.5 times solar (Unterborn et al., 2015). Moreover, many exoplanets, in particular those around M-dwarf 1109 stars, could experience significant additional heating from tidal dissipation or magnetic induction heating 1110 (Jackson et al., 2008; Kislyakova et al., 2017). Such planets would be more likely to form thick crusts and 1111 enter the thick crust limit, as well as have these thick crusts significantly influence their thermal histories. 1112 Our thermal evolution model results therefore have important implications for the lifetime of volcanism 1113 on such rocky stagnant-lid planets exoplanets. How long rocky planets stay volcanically active is of course of 1114 interest for understanding their geologic histories, but is also critical for the evolution of their atmospheres. In particular, stagnant-lid exoplanets that lie in their respective habitable zones can potentially sustain 1116 temperate climates through the carbonate-silicate cycle (Tosi et al., 2017; Dorn et al., 2018; Foley & Smye, 1117 2018; Valencia et al., 2018; Foley, 2019; Höning et al., 2019). However, volcanism is critical for maintaining 1118 CO<sub>2</sub> outgassing rates high enough to prevent global glaciation (Kadoya & Tajika, 2014; Foley & Smye, 2018; 1119 Foley, 2019), so when volcanism ends, frozen snowball climates may prevail. That the presence of a thick, 1120 buoyant crust weakens the Tozer feedback means that planets that are otherwise identical, but have different 1121 initial mantle temperatures, could have drastically different thermal histories. Planets starting with initially 1122 hot mantles will be able to sustain volcanism, and thus potentially habitable surface conditions, for up to a 1123 few Gyrs longer than planets starting with initially cooler mantles. More detailed thermal evolution models 1124 would be needed to quantify this effect more precisely, and how it influences predictions of the volcanic 1125 lifetimes of rocky stagnant-lid planets. As our scaling analysis indicates, the effects of crustal buoyancy on 1126 thermal history will be most pronounced for smaller planets with low reference viscosities and high internal 1127 heat production rates, and thus it is these planets where initial conditions can most influence subsequent 1128 evolution, and predicting the lifetime of volcanism will be most difficult. 1129

If Mars ever did enter the thick crust limit, this was likely short-lived and didn't significantly alter mantle

### 1130 6 Discussion

1103

Our numerical convection models made a number of simplifications in order to reduce complexity, such that the influence of crustal buoyancy forces on stagnant-lid convection could be isolated, and scaling laws describing these effects developed. The simplifications in our numerical model setup were outlined in §12, and the implications discussed in some detail in §5. Specifically, our numerical convection models are bottom heated and employ the Frank-Kamenetskii approximation for viscosity. Our scaling laws are thus only benchmarked against fully dynamic mantle convection calculations for these conditions. However, as we argue in §5.1, we expect them to still apply, at least to first order accuracy, to internally heated convection or when an Arrhenius viscosity law is used, based on previous studies of stagnant-lid convection and convection beneath continents on Earth. For mixed-mode heating the percentage of internal heating likely also matters, and new convection models would be needed to develop scaling laws incorporating this factor.

1134

1136

1138

1140

1148

A potentially more important simplification is that we neglect differences in thermal conductivity and heat production rate between the crust and mantle, in both the numerical convection models and thermal evolution models. As explained in §5.2, this is unlikely to affect the thin crust limit scaling laws, as the mantle convective heat flux in this case is determined by the heat flux across the rheological sublayer, which is a function of  $\theta$  and  $Ra_i$ . However, heat flux in the thick crust limit will be modified, as the temperature at the base of the crust,  $T_c$ , will be influenced by the heat production rate and thermal conductivity in the crust.

A more general formulation for the mantle convective heat flux in the thick crust limit is

$$q = \frac{k(T_i - T_c)}{\delta_{ol}}. (34)$$

This heat flux will be applied to the base of the crust, and the total surface heat flux will include q and any heat produced within the crust.  $T_c$  can then be determined in a more general way by using the onedimensional, steady-state heat conduction equation to calculate a geotherm through the crust with a given
thickness  $\delta_c$ , conductivity  $k_c$ , and heat production rate per unit volume,  $x_c$ ; the latter two need not be the
same as their respective values in the mantle. Matching the heat flux at the base of the crust with the mantle
convective heat flux, one can solve for  $T_c$  as

$$T_c = \frac{x_c \delta_c^2 \delta_{sl}}{2(\delta_{sl} k_c + \delta_c k)} + \frac{k_c T_s \delta_{sl} + k T_i \delta_c}{\delta_{sl} k_c + \delta_c k}.$$
 (35)

If  $k_c = k$  and  $x_c = 0$ , Eq. (35) is equivalent to the dimensional form of Eq. (16).

Combining Eq. (35) with Eq. (15), both  $T_c$  and  $\delta_{sl}$  can be calculated numerically. If  $\delta_{sl}$  is fixed, either decreasing  $k_c$  or increasing  $x_c$  causes  $T_c$  to increase. However, increasing  $T_c$  also causes  $\delta_{sl}$  to increase, because the temperature difference driving foundering of the sub-crustal boundary layer is smaller. From Eq. (35), a larger  $\delta_{sl}$  acts to decrease  $T_c$  in most cases (though the situation can reverse if heat production rates in the crust are very large), so there are competing effects for how decreasing  $k_c$  or increasing  $x_c$ 

would ultimately influence  $T_c$ ,  $\delta_{sl}$ , and convective heat flux, q. In the end, the direct influence of either decreasing  $k_c$  or increasing  $x_c$  on  $T_c$  is stronger; both  $T_c$  and  $\delta_{sl}$  increase in this case. As a result, the mantle convective heat flux, q, will decrease. Thus, including the effects of a lower thermal conductivity or enrichment of heat producing elements in the crust will both act to suppress heat flux in the thick crust limit, even further than our results presented above in §5.2 show. The increase in  $\delta_{sl}$  brought about by lower crustal thermal conductivity or higher crustal heat production would also make it easier for planets to enter the thick crust limit; that is, the range of conditions where the thick crust limit could prevail, shown in Figure 14, would expand. Ultimately numerical convection models including internal heating, concentration of heat producing elements in the crust, and variable crustal thermal conductivity will be needed to confirm the trends we outline here based on a simple geotherm calculation. 

The effect of our model simplifications on mantle thermal evolution is more complicated, with many competing factors. We outline these competing effects here, but ultimately more complex thermal evolution models that track the time evolution of crustal thickness, heat loss by volcanism, and concentration of heat producing elements in the crust would be needed to determine which effects are dominant. Such a task is beyond the scope of this paper, but an important avenue for future work.

As seen above, the effect of a lower thermal conductivity and heat producing element enrichment in the crust will make the heat flux in the thick crust limit even lower than what was used in our thermal evolution models, for a given crustal thickness. This would tend to accentuate the effects described in §5.2, and prolong the time period where convection operates in the thick crust limit. However, there are important effects cutting the other way, which may be more significant in the end: depletion of heat producing elements from the mantle due to crust formation, heat loss due to volcanism, and early heat loss before a thick crust has formed. As explained in §5.2, crust formation strips heat producing elements from the mantle, thereby lowering heating power in the mantle. This would lead to smaller deviations between the no crust and thick crust cases than our thermal evolution models show. However, even with the lowest mantle heat production rate we considered, a thick crust still significantly modifies mantle thermal history when the reference viscosity is low. Therefore crustal buoyancy could be broadly important for planets with compositions that lead to low viscosities. For planets with higher viscosities, large heat production rates, either due to high abundances of heat producing elements or additional heat sources, would be needed for a thick, buoyant crust to significantly modify thermal evolution.

Our numerical convection models and thermal evolution models also neglect heat transport by melting and volcanic eruption, which is a significant heat loss mechanism when mantle temperatures are high (e.g. O'Reilly & Davies, 1981; Ogawa & Nakamura, 1998; Nakagawa & Tackley, 2012; Moore & Webb, 2013; Driscoll & Bercovici, 2014; Moore et al., 2017). Including heat loss by volcanism would likely produce lower

mantle temperatures for all of our thermal evolution models, and potentially lessen the temperature difference between models with a thick crust and those with a thin or no crust as well. Ultimately more sophisticated thermal evolution models incorporating parameterizations for heat loss by volcanism (e.g. Kankanamge & Moore, 2019), combined with our scaling laws for convective heat flux in the thick crust limit, would be needed to determine the extent to which volcanic heat loss would limit the effect of a thick, buoyant crust on mantle thermal history.

Finally, crustal thickness will of course evolve over time rather than remaining fixed, as assumed in our thermal evolution models, and, save for some entrainment of the buoyant crustal layer, in our numerical convection models. Very early in a planet's history, the crust will grow as a result of volcanism, and thus there will be a finite time before the crust is thick enough to enter the thick crust limit. As a result, heat loss during a planet's very early history will likely be higher than our thermal evolution models predict. However, the crust formed rapidly on Mars, and such rapid crust growth due to extensive volcanism appears common across the solar system (e.g. Moore et al., 2017; Byrne, 2020). Moreover, factors that lead to the strongest influence of crustal bouyancy on thermal evolution, low reference viscosity, high initial mantle temperature, and high mantle heat production rate, also favor the rapid formation of a thick crust. We therefore do not expect this to be a significant effect, though the influence of the time evolution of crustal thickness should be tested with more sophisticated thermal evolution models.

Loss of crust due to foundering or entrainment is also a possibility, that could modify our thermal evolution model results. As previously discussed in §3, we do see entrainment of the crust, in particular when the magnitude of the buoyancy number is low and the Rayleigh number is high. However, even this entrainment is slow, and the rate of entrainment is likely overpredicted in the models due to numerical artifacts. We therefore do not expect entrainment of buoyant crust to limit crustal thickness on real planets. Faster entrainment rates could be seen if thermal buoyancy forces are able to dominate compositional buoyancy forces in the convective sub-layer at the base of the stagnant lid. However, such a situation would require buoyancy number absolute values  $< 1/\theta$ , and thus very small compositional density differences of  $<\sim 10$  ${
m kg\cdot m^{-3}}$  for a Mars-size planet with a mantle potential temperature of 2100 K (a lower mantle temperature decreases this estimated compositional density difference even further) (Tackley, 2015). Even mafic crust formed from high degree mantle melting, such as komatiiate, has a compositional density difference much larger than 10 kg·m<sup>-3</sup>. Cooling of the mantle over time could also form a gradient in buoyancy number in the crust, with crust formed from higher temperature melting at the bottom and lower temperature melting at the top; the lower crust would then have weaker compositional buoyancy (lower magnitude buoyancy number) than the upper crust. However, given the arguments above, entrainment is likely to still be slow in this case, and such a buoyancy gradient in the crust is unlikely to change our scaling laws. Moreover, such a compositional gradient would also be convectively stable, and help prevent convection from developing within the crust. Finally, even if crust is actively thinning due to entrainment, our results show that Nusselt number follows the same trend as a function of crustal thickness that our scaling laws predict.

Foundering of dense lower crust could be significant as well, and would likely enhance convective heat flux above what our thick crust limit scaling laws predict. Our thermal evolution models assume the maximum crustal thickness is set by the transition to eclogite. However, if active volcanism is continuously creating new crust at the surface, and subsequently pushing the whole crustal column downwards, lower crust will be pushed into the eclogite stability field. As a result, this lower crust can founder into the mantle, dragging the underlying sub-crustal boundary layer with it. A planet where the lower crust is continuously foundering may thus have a thinner, or even effectively non-existent, sub-crustal boundary layer, and therefore higher convective heat flux with a thick crust than our models find. An important avenue for future work is thus investigating stagnant-lid convection with a buoyant upper crust and negatively buoyant lower crust, to develop heat flux scaling laws for the case where the lower crust is actively foundering. A similar effect was proposed by Lourenço et al. (2018), who argue that lithospheric weakening by melt intrusion can drive foundering of the lithosphere, and hence enhance stagnant-lid convective heat flux. However, this work did not consider buoyancy variations between the upper and lower crust and mantle, which are critical for the crustal foundering described here.

### 7 Conclusions

Numerical models of stagnant-lid convection with a buoyant crustal layer demonstrate two end-member regimes of behavior: a thin crust limit, where convection is largely unaffected by the presence of the buoyant crustal layer or its thickness, and a thick crust limit, where the buoyant crustal layer itself dictates the thickness of the stagnant lid, and hence the convective heat flux. We develop scaling laws for the Nusselt number in both limits. In the thin crust limit, convection follows previously developed scaling laws for purely thermal stagnant-lid convection, because the buoyant layer has a negligible effect. In the thick crust limit, a scaling law for Nusselt number is developed by assuming the stagnant lid thickness is given by the sum of the buoyant crustal layer thickness and the thickness of a sub-crustal thermal boundary layer. The sub-crustal thermal boundary layer thickness is found from standard boundary layer theory.

The scaling laws match the numerical model results well. The scaling laws also show when convection switches between these two end-member limits. Specifically, the thick crust limit is entered when the sum of the crust and sub-crustal thermal boundary layer thicknesses is greater than the stagnant lid thickness expected if there was no buoyant crustal layer. Mantle interior temperature also increases in the thick crust

limit, due to inefficient convective heat loss. A simple energy balance model was used to develop a scaling law that captures this effect to first order.

The critical crustal thickness that must be exceeded for convection to enter the thick crust limit is a strong function of mantle interior temperature, mantle reference viscosity, and planet size. The higher the temperature and lower the reference viscosity, the thinner the critical crustal thickness for convection to operate in the thick crust limit; planetary mantles are therefore more likely to convect in the thick crust limit under these conditions. Convective vigor declines with decreasing planet size, and the critical crustal thickness therefore increases. However, crustal thickness is likely limited by the transition to eclogite. This transition occurs much deeper on a smaller planet than a larger one. If the crust can grow no deeper than the depth where eclogite forms, then a wider range of interior temperatures and reference viscosities allow convection to enter the thick crust limit on a smaller planet than a larger one. Reference viscosity would have to be low (< 10<sup>20</sup> Pa·s) and mantle temperatures very high for convection to ever enter the thick crust limit on an Earth-size planet.

Applying the scaling laws to the thermal evolution of Mars-like stagnant-lid exoplanets shows that when convection operates in the thick crust limit, mantle heat flux is suppressed, and thus mantle temperature is elevated, in comparison to a case where no crust is present. Such an elevation in mantle temperature due to convection operating in the thick crust limit occurs early in a planet's history, when heat production and interior temperatures are high. As the planet cools, convection eventually switches to the thin crust limit, and, with enough time, planets with a thick crust and those with no crust converge to the same thermal evolution. However, during the time when the mantle convects in the thick crust limit, mantle temperatures can reach hundreds of degrees K hotter than the no crust case, and these elevated temperatures can last for > 5 Gyrs, depending on mantle reference viscosity, crustal thickness, and heat production rate. Specifically the lower the reference viscosity, higher the heat production rate, and thicker the crust, the more pronounced and long-lasting the period of elevated mantle temperatures. Our analysis indicates that Mars' mantle reference viscosity is too high and heat production rate too low for crustal buoyancy to have played a significant role it its thermal history. However, crustal buoyancy would be important for exoplanets with lower reference viscosities or higher interior heat production rates.

The models also show that initial mantle temperature is important. The hotter the initial temperature, the easier it is for convection to enter the thick crust limit. When convection is in the thick crust limit, the suppression of mantle heat flux means primordial heat is retained for longer. Thick, buoyant crusts therefore weaken the Tozer feedback, and cause the influence of initial conditions to persist for far longer on stagnant-lid planets than traditional thermal evolution models, which ignore the effects of crustal buoyancy, would predict. In particular small rocky exoplanets with low reference viscosities and high heat production

rates may take longer than the age of our solar system before initial conditions are erased, so predicting the
thermal state of such planets may be especially difficult.

Table 4: Compilation of numerical model results without crustal convection

	1		1	ı		
$Ra_0$	θ	$\delta_{c0}^{'}$	$\delta_c^{'}$	$T_{i}^{'}$	Nu	В
$10^{6}$	13.82	0.0	-	$0.9195 \pm 8.7 \times 10^{-13}$	$1.6646 \pm 1.7 \times 10^{-13}$	-
$10^{6}$	13.82	0.1	$0.0934 \pm 2.63 \times 10^{-5}$	$0.9195 \pm 2.63 \times 10^{-13}$	$1.6646 \pm 4.85 \times 10^{-5}$	-1.0
$10^{6}$	13.82	0.2	$0.1928 \pm 9.64 \times 10^{-6}$	$0.9196 \pm 4.43 \times 10^{-6}$	$1.6637 \pm 7.33 \times 10^{-5}$	-1.0
$10^{6}$	13.82	0.3	$0.2922 \pm 6.45 \times 10^{-5}$	$0.9204 \pm 2.09 \times 10^{-5}$	$1.6456 \pm 1.26 \times 10^{-4}$	-1.0
$10^{6}$	13.82	0.4	$0.3898 \pm 1.23 \times 10^{-4}$	$0.9204 \pm 1.13 \times 10^{-4}$	$1.5802 \pm 0.001$	-1.0
$10^{6}$	13.82	0.5	$0.4897 \pm 1.31 \times 10^{-4}$	$0.9256 \pm 4.67 \times 10^{-5}$	$1.4502 \pm 6.65 \times 10^{-5}$	-1.0
$3 \times 10^{6}$	13.82	0.0	-	$0.9261 \pm 8.60 \times 10^{-13}$	$2.0650 \pm 8.14 \times 10^{-6}$	-
$3 \times 10^{6}$	13.82	0.1	$0.0928 \pm 1.21 \times 10^{-5}$	$0.9261 \pm 8.72 \times 10^{-6}$	$2.0638 \pm 2.35 \times 10^{-4}$	-1.0
$3 \times 10^{6}$	13.82	0.2	$0.1926 \pm 1.13 \times 10^{-5}$	$0.9263 \pm 2.18 \times 10^{-5}$	$2.0560 \pm 6.97 \times 10^{-4}$	-1.0
$3 \times 10^{6}$	13.82	0.3	$0.2895 \pm 3.09 \times 10^{-5}$	$0.9274 \pm 7.43 \times 10^{-5}$	$2.0010 \pm 2.20 \times 10^{-4}$	-1.0
$3 \times 10^{6}$	13.82	0.35	$0.3392 \pm 5.30 \times 10^{-5}$	$0.9302 \pm 7.65 \times 10^{-5}$	$1.9101 \pm 5.83 \times 10^{-4}$	-1.0
$3 \times 10^{6}$	13.82	0.4	$0.3895 \pm 3.06 \times 10^{-5}$	$0.9342 \pm 1.01 \times 10^{-4}$	$1.7910 \pm 9.18 \times 10^{-5}$	-1.0
$3 \times 10^{6}$	13.82	0.5	$0.4909 \pm 2.91 \times 10^{-5}$	$0.9410 \pm 1.13 \times 10^{-4}$	$1.5572 \pm 3.23 \times 10^{-4}$	-1.0
$5 \times 10^6$	13.82	0.0	-	$0.9271 \pm 3.30 \times 10^{-13}$	$2.3084 \pm 2.02 \times 10^{-12}$	-
$5 \times 10^6$	13.82	0.2	$0.1913 \pm 4.90 \times 10^{-5}$	$0.9268 \pm 4.70 \times 10^{-5}$	$2.3020 \pm 0.0017$	-1.0
$5 \times 10^6$	13.82	0.3	$0.2871 \pm 5.62 \times 10^{-5}$	$0.9325 \pm 3.68 \times 10^{-4}$	$2.1574 \pm 0.0014$	-1.0
$5 \times 10^{6}$	13.82	0.32	$0.3072 \pm 5.34 \times 10^{-5}$	$0.9337 \pm 2.82 \times 10^{-4}$	$2.1077 \pm 0.0012$	-1.0
$5 \times 10^{6}$	13.82	0.4	$0.3883 \pm 4.96 \times 10^{-5}$	$0.9407 \pm 2.69 \times 10^{-4}$	$1.8679 \pm 2.39 \times 10^{-4}$	-1.0
$5 \times 10^{6}$	13.82	0.5	$0.4906 \pm 4.26 \times 10^{-5}$	$0.9464 \pm 4.51 \times 10^{-4}$	$1.6061 \pm 8.30 \times 10^{-4}$	-1.0
$10^{7}$	13.82	0.0	-	$0.9258 \pm 5.19 \times 10^{-13}$	$2.6895 \pm 2.07 \times 10^{-12}$	-
$10^{7}$	13.82	0.1	$0.0928 \pm 6.57 \times 10^{-6}$	$0.9261 \pm 1.24 \times 10^{-4}$	$2.6797 \pm 0.0033$	-1.0
$10^{7}$	13.82	0.2	$0.1887 \pm 4.31 \times 10^{-5}$	$0.9300 \pm 0.001$	$2.6092 \pm 0.0071$	-1.0
107	13.82	0.25	$0.2367 \pm 6.19 \times 10^{-5}$	$0.9324 \pm 7.07 \times 10^{-4}$	$2.5091 \pm 0.0024$	-1.0
107	13.82	0.3	$0.2858 \pm 5.60 \times 10^{-5}$	$0.9361 \pm 7.37 \times 10^{-4}$	$2.3431 \pm 0.0019$	-1.0
$10^{7}$	13.82	0.4	$0.3880 \pm 8.85 \times 10^{-5}$	$0.9489 \pm 0.0012$	$2.0073 \pm 0.0024$	-1.0
$10^{7}$	13.82	0.5	$0.4887 \pm 1.74 \times 10^{-4}$	$0.9564 \pm 5.24 \times 10^{-4}$	$1.6867 \pm 7.70 \times 10^{-4}$	-1.0
$10^{7}$	13.82	0.2	$0.151 \pm 3.84 \times 10^{-4}$	$0.9309 \pm 9.45 \times 10^{-4}$	$2.6496 \pm 0.003$	-0.3
$10^{7}$	13.82	0.3	$0.161 \pm 0.0037$	$0.9336 \pm 9.35 \times 10^{-4}$	$2.6118 \pm 0.001$	-0.3
$10^{7}$	13.82	0.4	$0.278 \pm 0.0064$	$0.9387 \pm 0.0022$	$2.4352 \pm 0.006$	-0.3

Table 4: Compilation of numerical model results without crustal convection

$Ra_0$	θ	$\delta_{c0}^{'}$	$\delta_c^{'}$	$T_{i}^{'}$	Nu	В
$10^{7}$	13.82	0.2	$0.167 \pm 3.10 \times 10^{-4}$	$0.9331 \pm 0.0012$	$2.6048 \pm 0.017$	-0.5
$10^{7}$	13.82	0.3	$0.201 \pm 0.0064$	$0.9333 \pm 0.0014$	$2.516 \pm 0.0022$	-0.5
107	13.82	0.4	$0.374 \pm 3.59 \times 10^{-4}$	$0.9472 \pm 4.63 \times 10^{-4}$	$2.0657 \pm 0.0043$	-0.5
$10^{7}$	13.82	0.2	$0.178 \pm 1.46 \times 10^{-4}$	$0.9338 \pm 0.0011$	$2.5735 \pm 0.0016$	-0.7
$10^{7}$	13.82	0.3	$0.271 \pm 0.0022$	$0.9362 \pm 0.001$	$2.4085 \pm 0.0022$	-0.7
$10^{7}$	13.82	0.4	$0.385 \pm 9.92 \times 10^{-5}$	$0.9472 \pm 7.11 \times 10^{-4}$	$2.0176 \pm 9.13 \times 10^{-4}$	-0.7
$3 \times 10^7$	13.82	0.0	-	$0.9292 \pm 8.02 \times 10^{-4}$	$3.49 \pm 8.90 \times 10^{-4}$	-
$5 \times 10^7$	13.82	0.0	-	$0.9308 \pm 7.58 \times 10^{-4}$	$3.9701 \pm 0.0014$	-
$7 \times 10^7$	13.82	0.0	-	$0.9311 \pm 0.0013$	$4.4246 \pm 0.0043$	-
$10^{8}$	13.82	0.0	-	$0.9264 \pm 9.48 \times 10^{-4}$	$4.7581 \pm 0.0106$	-
$10^{8}$	13.82	0.05	$0.0427 \pm 2.54 \times 10^{-5}$	$0.9292 \pm 9.33 \times 10^{-4}$	$4.7083 \pm 0.0027$	-1.0
$10^{8}$	13.82	0.1	$0.0925 \pm 2.79 \times 10^{-5}$	$0.9308 \pm 0.0012$	$4.6547 \pm 0.0139$	-1.0
$10^{8}$	13.82	0.15	$0.1398 \pm 5.40 \times 10^{-5}$	$0.9378 \pm 0.0014$	$4.4180 \pm 0.0172$	-1.0
$10^{8}$	13.82	0.2	$0.1896 \pm 1.84 \times 10^{-4}$	$0.9421 \pm 0.0012$	$3.8680 \pm 0.0017$	-1.0
$10^{8}$	13.82	0.3	$0.2871 \pm 3.43 \times 10^{-4}$	$0.9542 \pm 0.001$	$3.0266 \pm 0.0033$	-1.0
$10^{8}$	13.82	0.15	$0.125 \pm 2.47 \times 10^{-4}$	$0.9303 \pm 0.0012$	$4.6875 \pm 0.0042$	-0.3
$10^{8}$	13.82	0.25	$0.225 \pm 2.53 \times 10^{-4}$	$0.945 \pm 0.0011$	$3.5254 \pm 0.0206$	-0.3
$10^{8}$	13.82	0.15	$0.138 \pm 1.91 \times 10^{-4}$	$0.9358 \pm 5.59 \times 10^{-4}$	$4.5728 \pm 0.0166$	-0.5
108	13.82	0.25	$0.236 \pm 1.57 \times 10^{-4}$	$0.9468 \pm 9.24 \times 10^{-4}$	$3.3726 \pm 0.0014$	-0.5
108	13.82	0.15	$0.142 \pm 2.97 \times 10^{-5}$	$0.936 \pm 8.17 \times 10^{-4}$	$4.3093 \pm 0.0032$	-0.7
108	13.82	0.25	$0.239 \pm 6.03 \times 10^{-5}$	$0.9482 \pm 0.0015$	$3.3313 \pm 3.53 \times 10^{-4}$	-0.7
$3 \times 10^{8}$	13.82	0.0	-	$0.9264 \pm 0.0011$	$6.5279 \pm 0.0029$	-
$5 \times 10^{8}$	13.82	0.0	-	$0.9206 \pm 6.16 \times 10^{-4}$	$7.8563 \pm 0.0043$	-
$5 \times 10^8$	13.82	0.05	$0.0420 \pm 2.05 \times 10^{-4}$	$0.9212 \pm 9.12 \times 10^{-4}$	$7.8178 \pm 0.0073$	-1.0
$5 \times 10^8$	13.82	0.1	$0.0887 \pm 7.03 \times 10^{-4}$	$0.9265 \pm 0.001$	$7.1272 \pm 0.0026$	-1.0
$5 \times 10^8$	13.82	0.15	$0.1322 \pm 4.60 \times 10^{-4}$	$0.9374 \pm 6.45 \times 10^{-4}$	$6.0529 \pm 0.0032$	-1.0
$5 \times 10^8$	13.82	0.2	$0.1764 \pm 7.28 \times 10^{-4}$	$0.9481 \pm 7.06 \times 10^{-4}$	$4.9086 \pm 0.0019$	-1.0
$5 \times 10^8$	13.82	0.1	$0.061 \pm 1.62 \times 10^{-4}$	$0.9221 \pm 7.61 \times 10^{-4}$	$7.8473 \pm 0.0225$	-0.3
$5 \times 10^8$	13.82	0.1	$0.091 \pm 5.08 \times 10^{-5}$	$0.9283 \pm 9.78 \times 10^{-4}$	$6.9121 \pm 0.0066$	-0.5

Table 4: Compilation of numerical model results without crustal convection

$Ra_0$	$\theta$	$\delta_{c0}^{'}$	$\delta_c^{'}$	$T_i^{'}$	Nu	В
$5 \times 10^8$	13.82	0.1	$0.093 \pm 1.10 \times 10^{-4}$	$0.9311 \pm 9.91 \times 10^{-4}$	$6.8331 \pm 0.0026$	-0.7
$5 \times 10^8$	13.82	0.15	$0.1302 \pm 3.38 \times 10^{-4}$	$0.9386 \pm 0.0021$	$5.8378 \pm 7.16 \times 10^{-4}$	-0.3
$5 \times 10^{8}$	13.82	0.15	$0.1366 \pm 2.00 \times 10^{-4}$	$0.94 \pm 0.0013 \times 10^{-4}$	$5.6128 \pm 0.0013$	-0.5
$5 \times 10^{8}$	13.82	0.15	$0.139 \pm 1.17 \times 10^{-4}$	$0.9411 \pm 0.0014$	$5.5059 \pm 5.46 \times 10^{-4}$	-0.7
$7 \times 10^8$	13.82	0.0	-	$0.9212 \pm 8.44 \times 10^{-4}$	$8.587 \pm 0.0028$	-
$10^{7}$	16.12	0.0	-	$0.9365 \pm 3.55 \times 10^{-13}$	$2.2622 \pm 1.91 \times 10^{-12}$	-
$10^{7}$	16.12	0.1	$0.0931 \pm 5.73 \times 10^{-6}$	$0.9365 \pm 4.85 \times 10^{-6}$	$2.2620 \pm 4.90 \times 10^{-5}$	-1.0
$10^{7}$	16.12	0.2	$0.1928 \pm 2.48 \times 10^{-6}$	$0.9367 \pm 1.30 \times 10^{-5}$	$2.2552 \pm 4.82 \times 10^{-4}$	-1.0
$10^{7}$	16.12	0.25	$0.2418 \pm 1.03 \times 10^{-5}$	$0.9369 \pm 1.11 \times 10^{-4}$	$2.2472 \pm 0.0015$	-1.0
$10^{7}$	16.12	0.3	$0.2899 \pm 2.81 \times 10^{-5}$	$0.9398 \pm 3.55 \times 10^{-4}$	$2.1702 \pm 0.0035$	-1.0
$10^{7}$	16.12	0.4	$0.3906 \pm 3.07 \times 10^{-5}$	$0.9465 \pm 7.92 \times 10^{-4}$	$1.8887 \pm 1.18 \times 10^{-4}$	-1.0
$5 \times 10^7$	16.12	0.0	_	$0.9371 \pm 0.0013$	$3.2609 \pm 0.0104$	-
$5 \times 10^7$	16.12	0.1	$0.0934 \pm 2.92 \times 10^{-5}$	$0.9371 \pm 0.0013$	$3.3048 \pm 0.0075$	-1.0
$5 \times 10^7$	16.12	0.2	$0.1928 \pm 0.0075$	$0.9442 \pm 0.0011$	$3.0337 \pm 0.0093$	-1.0
$5 \times 10^7$	16.12	0.25	$0.2426 \pm 5.42 \times 10^{-5}$	$0.9465 \pm 0.0012$	$2.8745 \pm 0.0046$	-1.0
$5 \times 10^7$	16.12	0.3	$0.2914 \pm 2.43 \times 10^{-4}$	$0.9519 \pm 0.0017$	$2.6628 \pm 0.006$	-1.0
$5 \times 10^7$	16.12	0.4	$0.3887 \pm 1.60 \times 10^{-4}$	$0.9598 \pm 9.46 \times 10^{-4}$	$2.1549 \pm 6.15 \times 10^{-4}$	-1.0
$7 \times 10^7$	16.12	0.0	-	$0.938 \pm 0.001$	$3.6595 \pm 0.0156$	-
$10^{8}$	16.12	0.0	-	$0.9351 \pm 9.73 \times 10^{-4}$	$4.0564 \pm 0.0083$	-
$10^{8}$	16.12	0.05	$0.0420 \pm 3.79 \times 10^{-5}$	$0.9351 \pm 9.65 \times 10^{-4}$	$4.0191 \pm 0.0105$	-1.0
$10^{8}$	16.12	0.1	$0.0931 \pm 1.15 \times 10^{-5}$	$0.9352 \pm 0.0011$	$4.0644 \pm 0.0152$	-1.0
$10^{8}$	16.12	0.15	$0.1423 \pm 2.59 \times 10^{-4}$	$0.9334 \pm 0.0011$	$3.9814 \pm 0.0037$	-1.0
$10^{8}$	16.12	0.2	$0.1912 \pm 3.06 \times 10^{-4}$	$0.9389 \pm 8.61 \times 10^{-4}$	$3.5552 \pm 0.0072$	-1.0
$10^{8}$	16.12	0.3	$0.2886 \pm 3.17 \times 10^{-4}$	$0.9517 \pm 9.94 \times 10^{-4}$	$2.8710 \pm 0.0033$	-1.0
$3 \times 10^8$	16.12	0.0	-	$0.9373 \pm 9.84 \times 10^{-4}$	$5.4032 \pm 0.012$	_

Table 4: Compilation of numerical model results without crustal convection

$Ra_0$	$\theta$	$\delta_{c0}^{'}$	$\delta_c^{'}$	$T_{i}^{'}$	Nu	B
1 2000		$^{\circ}c_{0}$	c	<b>-</b> <i>i</i>	1	_

Note that all crustal thickness, internal temperature, and Nusselt number averages, and their standard deviations, for all models with  $B=-0.7,\,-0.5,\,\mathrm{or}\,-0.3$  were calculated from the final 25 model timesteps, as these models do not reach a statistical steady-state due to crustal entrainment.

Table 5: Compilation of numerical convection model results with crustal convection

$Ra_0$	θ	$\delta_{c0}^{'}$	$\delta_c^{'}$	$T_{i}^{^{\prime}}$	Nu	В
108	13.82	0.4	$0.3767 \pm 0.0021$	$0.9534 \pm 0.0011$	$3.2401 \pm 0.0052$	-1.0
108	13.82	0.35	$0.243 \pm 8.77 \times 10^{-4}$	$0.9379 \pm 6.76 \times 10^{-4}$	$3.7912 \pm 0.003$	-0.3
108	13.82	0.35	$0.307 \pm 0.003$	$0.9497 \pm 6.97 \times 10^{-4}$	$3.1887 \pm 0.001$	-0.5
108	13.82	0.35	$0.323 \pm 2.44 \times 10^{-4}$	$0.9513 \pm 9.94 \times 10^{-4}$	$3.1346 \pm 0.002$	-0.7
$5 \times 10^8$	13.82	0.2	$0.155 \pm 5.18 \times 10^{-4}$	$0.9418 \pm 6.56 \times 10^{-4}$	$5.3843 \pm 0.0011$	-0.3
$5 \times 10^8$	13.82	0.3	$0.193 \pm 1.49 \times 10^{-4}$	$0.9437 \pm 5.29 \times 10^{-4}$	$5.212 \pm 0.0016$	-0.3
$5 \times 10^8$	13.82	0.2	$0.175 \pm 1.75 \times 10^{-4}$	$0.9479 \pm 3.45 \times 10^{-4}$	$4.8789 \pm 0.0023$	-0.5
$5 \times 10^8$	13.82	0.3	$0.194 \pm 0.0047$	$0.944 \pm 7.67 \times 10^{-4}$	$5.4074 \pm 0.0023$	-0.5
$5 \times 10^8$	13.82	0.2	$0.183 \pm 1.58 \times 10^{-4}$	$0.9482 \pm 6.69 \times 10^{-4}$	$4.8992 \pm 0.0068$	-0.7
$5 \times 10^8$	13.82	0.3	$0.268 \pm 0.0015$	$0.9478 \pm 6.02 \times 10^{-4}$	$5.1386 \pm 3.48 \times 10^{-4}$	-0.7
108	16.12	0.4	$0.3849 \pm 4.24 \times 10^{-4}$	$0.9616 \pm 8.84 \times 10^{-4}$	$2.2775 \pm 8.84 \times 10^{-4}$	-1.0

Note that all crustal thickness, internal temperature, and Nusselt number averages, and their standard deviations, for all models with  $B=-0.7,\,-0.5,\,$  or -0.3 were calculated from the final 25 model timesteps, as these models do not reach a statistical steady-state due to crustal entrainment.

Table 6: Crust Entrainment Rate

$Ra_0$	В	θ	$\delta_{c0}^{'}$	Elapsed Time $(t)$	$\delta_{ci}^{'}$	$\delta_{cf}^{'}$	Entrainment Rate
10 <sup>7</sup>	-0.3	13.82	0.2	0.3438	0.1927	0.1506	-0.1225
$10^{7}$	-0.3	13.82	0.3	0.4668	0.2931	0.1602	-0.2847
$10^{7}$	-0.3	13.82	0.4	0.2681	0.3935	0.2733	-0.4483
$10^{7}$	-0.5	13.82	0.2	0.3298	0.1928	0.167	-0.0782
$10^{7}$	-0.5	13.82	0.3	0.4985	0.2931	0.1936	-0.1996
$10^{7}$	-0.5	13.82	0.4	0.3037	0.3935	0.3735	-0.0659
$10^{7}$	-0.7	13.82	0.2	0.4022	0.1929	0.1775	-0.0383
$10^{7}$	-0.7	13.82	0.3	0.5368	0.2931	0.2674	-0.0479
$10^{7}$	-0.7	13.82	0.4	0.3420	0.3935	0.3851	-0.0246
$10^{8}$	-0.3	13.82	0.15	0.0328	0.1426	0.1243	-0.5579
$10^{8}$	-0.3	13.82	0.25	0.0462	0.2424	0.2247	-0.3831
$10^{8}$	-0.5	13.82	0.15	0.0312	0.1428	0.1372	-0.1795
$10^{8}$	-0.5	13.82	0.25	0.0629	0.2424	0.2355	-0.1097
$10^{8}$	-0.7	13.82	0.15	0.0372	0.1428	0.142	-0.0215
$10^{8}$	-0.7	13.82	0.25	0.0647	0.2426	0.2385	-0.0634
$5 \times 10^8$	-0.3	13.82	0.1	0.0474	0.0927	0.0554	-0.7869
$5 \times 10^8$	-0.3	13.82	0.15	0.0193	0.1429	0.1292	-0.7098
$5 \times 10^8$	-0.5	13.82	0.1	0.0143	0.0927	0.091	-0.1189
$5 \times 10^8$	-0.5	13.82	0.15	0.0275	0.1429	0.1361	-0.2473
$5 \times 10^8$	-0.7	13.82	0.1	0.0313	0.0927	0.0908	-0.0607
$5 \times 10^8$	-0.7	13.82	0.15	0.0249	0.1429	0.139	-0.1566
$10^{6}$	-1	13.82	0.1	2.1804	0.0941	0.0926	-0.0007
$10^{6}$	-1	13.82	0.2	2.1803	0.1927	0.1927	0.0000
$10^{6}$	-1	13.82	0.3	2.1803	0.2914	0.2909	-0.0002
$10^{6}$	-1	13.82	0.4	2.2205	0.3919	0.3866	-0.0024
$10^{6}$	-1	13.82	0.5	1.9304	0.4929	0.4868	-0.0032
$10^{6}$	-1	13.82	0.1	0.9994	0.0941	0.0929	-0.0012
$3 \times 10^6$	-1	13.82	0.2	0.9993	0.1928	0.1917	-0.0011
$3 \times 10^6$	-1	13.82	0.3	0.8523	0.2914	0.2857	-0.0067
$3 \times 10^6$	-1	13.82	0.35	0.8492	0.3436	0.3356	-0.0094

Table 6: Crust Entrainment Rate

$Ra_0$	В	θ	$\delta_{c0}^{'}$	Elapsed Time (t)	$\delta_{ci}^{'}$	$\delta_{cf}^{'}$	Entrainment Rate
$3 \times 10^6$	-1	13.82	0.4	0.8773	0.3926	0.3862	-0.0073
$3 \times 10^6$	-1	13.82	0.5	0.9995	0.4930	0.4886	-0.0044
$5 \times 10^6$	-1	13.82	0.2	0.9992	0.1928	0.1884	-0.0044
$5 \times 10^6$	-1	13.82	0.3	0.9992	0.2925	0.2813	-0.0112
$5 \times 10^6$	-1	13.82	0.32	0.9994	0.3130	0.3015	-0.0115
$5 \times 10^6$	-1	13.82	0.4	0.9962	0.3934	0.3837	-0.0097
$5 \times 10^6$	-1	13.82	0.5	0.9993	0.4933	0.4877	-0.0056
$10^{7}$	-1	13.82	0.1	0.9991	0.0941	0.0926	-0.0015
$10^{7}$	-1	13.82	0.2	0.9992	0.1928	0.1838	-0.0090
$10^{7}$	-1	13.82	0.25	0.8051	0.2426	0.2303	-0.0153
$10^{7}$	-1	13.82	0.3	0.9601	0.2933	0.2787	-0.0152
$10^{7}$	-1	13.82	0.4	0.9610	0.3939	0.3822	-0.0122
$10^{7}$	-1	13.82	0.5	0.9782	0.4935	0.4849	-0.0088
108	-1	13.82	0.05	0.1496	0.0417	0.0417	0.0000
108	-1	13.82	0.1	0.1470	0.0941	0.0921	-0.0136
108	-1	13.82	0.15	0.1879	0.1419	0.1376	-0.0229
108	-1	13.82	0.2	0.1880	0.1928	0.1870	-0.0309
108	-1	13.82	0.3	0.1989	0.2914	0.2826	-0.0442
$5 \times 10^8$	-1	13.82	0.05	0.0678	0.0414	0.0405	-0.0133
$5 \times 10^8$	-1	13.82	0.1	0.0698	0.0941	0.0843	-0.1404
$5 \times 10^8$	-1	13.82	0.15	0.0988	0.1418	0.1259	-0.1609
$5 \times 10^8$	-1	13.82	0.2	0.1110	0.1905	0.1679	-0.2036
$10^{7}$	-1	16.12	0.1	0.9991	0.0941	0.0927	-0.0014
$10^{7}$	-1	16.12	0.2	0.9993	0.1929	0.1928	-0.0001
$10^{7}$	-1	16.12	0.25	0.9992	0.2430	0.2394	-0.0036
$10^{7}$	-1	16.12	0.3	0.9783	0.2914	0.2858	-0.0057
$10^{7}$	-1	16.12	0.4	0.6571	0.3919	0.3879	-0.0061
$5 \times 10^7$	-1	16.12	0.1	0.1698	0.0941	0.0927	-0.0082
$5 \times 10^7$	-1	16.12	0.2	0.1879	0.1928	0.1926	-0.0011
$5 \times 10^7$	-1	16.12	0.25	0.2048	0.2430	0.2418	-0.0059

Table 6: Crust Entrainment Rate

$Ra_0$	В	θ	$\delta_{c0}^{'}$	Elapsed Time $(t)$	$\delta_{ci}^{'}$	$\delta_{cf}^{'}$	Entrainment Rate
$5 \times 10^7$	-1	16.12	0.3	0.2338	0.2914	0.2890	-0.0103
$5 \times 10^7$	-1	16.12	0.4	0.2388	0.3918	0.3843	-0.0314
$10^{8}$	-1	16.12	0.05	0.1959	0.0414	0.0414	0.0000
108	-1	16.12	0.1	0.1769	0.0941	0.0927	-0.0079
$10^{8}$	-1	16.12	0.15	0.1316	0.1419	0.1412	-0.0053
$10^{8}$	-1	16.12	0.2	0.1380	0.1928	0.1869	-0.0428
$10^{8}$	-1	16.12	0.3	0.1660	0.2914	0.2826	-0.0530

## 8 Acknowledgements

- This work has been supported by NSF Grant 1723057, the Pennsylvania State University's Erikson Discovery
- Grant, the Schreyer Honors College, and the NASA Pennsylvania Space Grant Consortium Undergraduate
- 1296 Scholarship. The authors thank William B. Moore and an anonymous reviewer for a critical scientific reviews
- that helped to significanly improve the manuscript.

# 9 Data availability

- The mantle convection code used to perform the modeling is available on GitHub: https://github.com/bradfordjfoley/foley-
- convection-code. The raw numerical model results and input files used for the models are available at Penn
- State's data commons: https://www.datacommons.psu.edu/commonswizard/MetadataDisplay.aspx?Dataset=6289

1302

## 3 10 Bibliography

### 1304 References

- Arndt, N. T. (1983). Role of a thin, komatiite-rich oceanic crust in the archean plate-tectonic process.
- 1306 Geology, 11, 372–375.
- <sup>1307</sup> Artemieva, I. M., & Meissner, R. (2012). Crustal thickness controlled by plate tectonics: a review of crust-
- mantle interaction processes illustrated by european examples. Tectonophysics, 530, 18–49.
- Baratoux, D., Samuel, H., Michaut, C., Toplis, M. J., Monnereau, M., Wieczorek, M., Garcia, R., & Kurita,
- 1310 K. (2014). Petrological constraints on the density of the martian crust. Journal of Geophysical Research:
- 1311 Planets, 119, 1707–1727.
- Beattie, P. (1993). Uranium-thorium disequilibria and partitioning on melting of garnet peridotite. Nature,
- 363, 63–65.
- Berner, R., Lasaga, A., & Garrels, R. (1983). The carbonate-silicate geochemical cycle and its effect on
- atmospheric carbon dioxide over the past 100 million years. Am. J. Sci, 283, 641–683.
- Botelho, R. B., Milone, A. d. C., Meléndez, J., Bedell, M., Spina, L., Asplund, M., dos Santos, L., Bean,
- J. L., Ramírez, I., Yong, D., Dreizler, S., Alves-Brito, A., & Yana Galarza, J. (2019). Thorium in solar
- twins: implications for habitability in rocky planets. Mon. Not. R. Astron. Soc., 482, 1690–1700.
- Breuer, D., & Moore, W. (2015). 10.08 Dynamics and Thermal History of the Terrestrial Planets, the
- Moon, and Io. In G. Schubert (Ed.), Treatise on Geophysics (Second Edition) (pp. 255 305). Oxford:
- Elsevier. (Second edition ed.).
- Byrne, P. K. (2020). A comparison of inner solar system volcanism. Nature Astronomy, 4, 321–327.
- 1323 Christensen, U., & Yuen, D. (1985). Layered convection induced by phase changes. J. Geophys. Res., 90,
- 291-300, .
- 1325 Christensen, U. R. (1984). Heat transport by variable viscosity convection and implications for the earth's
- thermal evolution. Physics of the earth and planetary interiors, 35, 264–282.
- 1327 Clauser, C., & Huenges, E. (1995). Thermal Conductivity of Rocks and Minerals. In Rock Physics & Phase
- Relations chapter 3-9. (pp. 105–126). American Geophysical Union (AGU).

- Davaille, A. (1999). Simultaneous generation of hotspots and superswells by convection in a heterogeneous planetary mantle. *Nature*, 402, 756–760.
- Davaille, A. (1999). Two-layer thermal convection in miscible viscous fluids. *Journal of Fluid Mechanics*, 379, 223–253.
- Davaille, A., & Jaupart, C. (1993). Transient high-Rayleigh-number thermal convection with large viscosity variations. J. Fluid Mech., 253, 141–166.
- Davies, G. (1992). On the emergence of plate tectonics. Geology, 20, 963–966.
- Davies, G. F. (2007). Thermal evolution of the mantle. In D. Stevenson, & G. Schubert (chief editor) (Eds.),

  Treatise on Geophysics (pp. 197–216). New York: Elsevier volume 9, Evolution of the Earth.
- Dorn, C., Noack, L., & Rozel, A. B. (2018). Outgassing on stagnant-lid super-Earths. Astron. Astrophys.,
  614, A18.
- Driscoll, P., & Bercovici, D. (2014). On the thermal and magnetic histories of Earth and Venus: Influences of melting, radioactivity, and conductivity. *Phys. Earth Planet. Inter.*, 236, 36–51.
- Driscoll, P. E., & Barnes, R. (2015). Tidal heating of Earth-like exoplanets around M stars: Thermal, magnetic, and orbital evolutions. *Astrobiology*, 15, 739–760.
- Dumoulin, C., Doin, M.-P., & Fleitout, L. (1999). Heat transport in stagnant lid convection with temperature- and pressure-dependent Newtonian or non-Newtonian rheology. *J. Geophys. Res.*, 104, 12759.
- Elkins-Tanton, L. T., Parmentier, E. M., & Hess, P. C. (2003). Magma ocean fractional crystallization and cumulate overturn in terrestrial planets: Implications for Mars. *Meteoritics and Planetary Science*, 38, 1753–1771.
- Foley, B. J. (2019). Habitability of Earth-like Stagnant Lid Planets: Climate Evolution and Recovery from
  Snowball States. Astrophys. J., 875, 72.
- Foley, B. J., & Bercovici, D. (2014). Scaling laws for convection with temperature-dependent viscosity and grain-damage. *Geophys. J. Int.*, 199, 580–603.
- Foley, B. J., Bercovici, D., & Elkins-Tanton, L. T. (2014). Initiation of plate tectonics from post-magma ocean thermochemical convection. *J. Geophys. Res. Solid Earth*, 119, 8538–8561.

- Foley, B. J., Bercovici, D., & Landuyt, W. (2012). The conditions for plate tectonics on super-earths:
- Inferences from convection models with damage. Earth Planet. Sci. Lett., 331–332, 281 290.
- Foley, B. J., & Driscoll, P. E. (2016). Whole planet coupling between climate, mantle, and core: Implications
- for rocky planet evolution. Geochem., Geophys., Geosyst., 17.
- Foley, B. J., & Rizo, H. (2017). Long-term preservation of early formed mantle heterogeneity by mobile lid
- convection: Importance of grainsize evolution. Earth Planet. Sci. Lett., 475, 94–105.
- Foley, B. J., & Smye, A. J. (2018). Carbon cycling and habitability of Earth-size stagnant lid planets.
- 1363 Astrobiology, 18, 873–896.
- Fowler, A. (1985). Fast thermoviscous convection. Studies in Applied Mathematics, 72, 189–219.
- Fraeman, A. A., & Korenaga, J. (2010). The influence of mantle melting on the evolution of Mars. *Icarus*,
- 210, 43–57.
- Garnero, E. J., & McNamara, A. K. (2008). Structure and Dynamics of Earth's Lower Mantle. Science,
- 320, 626.
- Goossens, S., Sabaka, T. J., Genova, A., Mazarico, E., Nicholas, J. B., & Neumann, G. A. (2017). Evidence
- for a low bulk crustal density for Mars from gravity and topography. Geophys. Res. Lett., 44, 7686–7694.
- Grasset, O., & Parmentier, E. M. (1998). Thermal convection in a volumetrically heated, infinite Prandtl
- number fluid with strongly temperature-dependent viscosity: Implications for planetary evolution. J.
- 1373 Geophys. Res., 1031, 18171–18181.
- Grott, M., Morschhauser, A., Breuer, D., & Hauber, E. (2011). Volcanic outgassing of CO<sub>2</sub> and H<sub>2</sub>O on
- 1375 Mars. Earth Planet. Sci. Lett., 308, 391–400.
- Hacker, B. R. (1996). Eclogite formation and the rheology, buoyancy, seismicity, and H<sub>2</sub>O content of oceanic
- crust. In G. Bebout, D. Scholl, S. Kirby, & J. P. Platt (Eds.), Subduction Top to Bottom (pp. 337–346).
- AGU Geophysical Monograph Series volume 96.
- Hacker, B. R., Abers, G. A., & Peacock, S. M. (2003). Subduction factory 1. theoretical mineralogy, densities,
- seismic wave speeds, and h2o contents. Journal of Geophysical Research: Solid Earth, 108.
- Hart, S. E., & Brooks, C. (1974). Clinopyroxene-matrix partitioning of K, Rb, Cs, Sr and Ba. Geochim.
- 1382 Cosmchim. Acta, 38, 1799–1806.

- Hauck, S. A., & Phillips, R. J. (2002). Thermal and crustal evolution of Mars. J. Geophys. Res. Planets, 1383 107, 6-1.
- Helffrich, G., & Wood, B. (2001). The earth's mantle. *Nature*, 412, 501–507. 1385

1387

- Hernlund, J., & McNamara, A. (2015). 7.11 The Core-Mantle Boundary Region. In G. Schubert (Ed.), Treatise on Geophysics (Second Edition) (pp. 461 – 519). Oxford: Elsevier. (Second edition ed.).
- Hirth, G., & Kohlstedt, D. (1996). Water in the oceanic upper mantle: implications for rheology, melt 1388 extraction and the evolution of the lithosphere. Earth Planet. Sci. Lett., 144, 93–108. 1389
- Höning, D., Tosi, N., & Spohn, T. (2019). Carbon cycling and interior evolution of water-covered plate tectonics and stagnant-lid planets. Astron. Astophys., 627, A48. 1391
- Ito, K., & Kennedy, G. C. (1971). An experimental study of the basalt-garnet granulite-eclogite transition. 1392 The structure and physical properties of the Earth's crust, 14, 303–314. 1393
- Jackson, B., Barnes, R., & Greenberg, R. (2008). Tidal heating of terrestrial extrasolar planets and impli-1394 cations for their habitability. Mon. Not. R. Astron. Soc., 391, 237–245. 1395
- Jackson, B., Greenberg, R., & Barnes, R. (2008). Tidal heating of extrasolar planets. The Astrophysical Journal, 681, 1631-1638. 1397
- Jaupart, C., Labrosse, S., Lucazeau, F., & Mareschal, J.-C. (2015). 7.06 temperatures, heat and energy in the mantle of the earth. In D. Bercovici, & G. Schubert (chief editor) (Eds.), Treatise on Geophysics 1399 (Second Edition) (pp. 223 – 270). New York: Elsevier volume 7, Mantle Dynamics. 1400
- Johnson, T. E., Brown, M., Kaus, B. J., & VanTongeren, J. A. (2014). Delamination and recycling of 1401 archaean crust caused by gravitational instabilities. Nature Geoscience, 7, 47–52. 1402
- Jones, T. D., Maguire, R. R., van Keken, P. E., Ritsema, J., & Koelemeijer, P. (2020). Subducted oceanic 1403 crust as the origin of seismically slow lower-mantle structures. Prog. Earth Planet. Sci., 7, 17. 1404
- Jull, M., & Kelemen, P. á. (2001). On the conditions for lower crustal convective instability. Journal of 1405 Geophysical Research: Solid Earth, 106, 6423-6446.
- Kadoya, S., & Tajika, E. (2014). Conditions for Oceans on Earth-like Planets Orbiting within the Habitable 1407 Zone: Importance of Volcanic CO<sub>2</sub> Degassing. Astrophys. J., 790, 107. 1408
- Kankanamge, D. G., & Moore, W. B. (2019). A parameterization for volcanic heat flux in heat pipe planets. 1409 Journal of Geophysical Research: Planets, 124, 114–127. 1410

- Kasting, J. F., & Catling, D. (2003). Evolution of a Habitable Planet. Annu. Rev. Astron. Astrophys., 41, 429–463.
- Katz, R. F., Spiegelman, M., & Langmuir, C. H. (2003). A new parameterization of hydrous mantle melting.

  Geochemistry, Geophysics, Geosystems, 4.
- Keller, T., & Tackley, P. J. (2009). Towards self-consistent modeling of the martian dichotomy: The influence of one-ridge convection on crustal thickness distribution. *Icarus*, 202, 429–443.
- Kellogg, L., Hager, B., & van der Hilst, R. (1999). Compositional stratification in the deep mantle. Science,
   283, 1881–1884.
- Kellogg, L. H. (1992). Mixing in the mantle. Annual Review of Earth and Planetary Sciences, 20, 365–388.
- Kislyakova, K. G., Noack, L., Johnstone, C. P., Zaitsev, V. V., Fossati, L., Lammer, H., Khodachenko, M. L.,
- Odert, P., & Güdel, M. (2017). Magma oceans and enhanced volcanism on TRAPPIST-1 planets due to
- induction heating. Nature Astronomy, 1, 878–885.
- <sup>1423</sup> Korenaga, J. (2006). Archean geodynamics and the thermal evolution of earth. In K. Benn, J.-C. Mareschal,
- & K. Condie (Eds.), Archean Geodynamics and Environments (pp. 7–32). AGU Geophysical Monograph
- Series volume 164.
- Korenaga, J. (2009). Scaling of stagnant-lid convection with Arrhenius rheology and the effects of mantle melting. Geophys. J. Int., 179, 154–170.
- Korenaga, J. (2010). On the likelihood of plate tectonics on super-earths: Does size matter? Astrophys. J., 725, L43.
- Korenaga, J. (2017). Pitfalls in modeling mantle convection with internal heat production. J. Geophys. Res.
   Solid Earth, 122, 4064–4085.
- Lenardic, A. (1998). On the partitioning of mantle heat loss below oceans and continents over time and its relationship to the archaean paradox. *Geophysical Journal International*, 134, 706–720.
- Lenardic, A., & Crowley, J. W. (2012). On the Notion of Well-defined Tectonic Regimes for Terrestrial

  Planets in this Solar System and Others. Astrophys. J. Lett., 755, 132.
- Lenardic, A., & Kaula, W. (1996). Near surface thermal/chemical boundary layer convection at infinite prandtl number: Two-dimensional numerical experiments. *Geophys. J. Int.*, 126, 689–711.

- Lenardic, A., Moresi, L.-N., Jellinek, A., & Manga, M. (2005). Continental insulation, mantle cooling, and
  the surface area of oceans and continents. *Earth and Planetary Science Letters*, 234, 317–333.
- Li, M., & McNamara, A. K. (2013). The difficulty for subducted oceanic crust to accumulate at the Earth's core-mantle boundary. J. Geophys. Res. (Solid Earth), 118, 1807–1816.
- Lodders, K., & Fegley, B. (1997). An Oxygen Isotope Model for the Composition of Mars. *Icarus*, 126, 373–394.
- Lourenço, D. L., Rozel, A. B., Gerya, T., & Tackley, P. J. (2018). Efficient cooling of rocky planets by intrusive magmatism. *Nature Geoscience*, 11, 322–327.
- Maaløe, S. (2004). The solidus of harzburgite to 3 gpa pressure: the compositions of primary abyssal tholeiite.

  Mineralogy and Petrology, 81, 1–17.
- McNamara, A. K., & Zhong, S. (2005). Degree-one mantle convection: Dependence on internal heating and temperature-dependent rheology. *Geophys. Res. Lett.*, 32, L01301.
- Moore, W. B. (2008). Heat transport in a convecting layer heated from within and below. *J. Geophys. Res.*, 113, 11407.
- Moore, W. B., Simon, J. I., & Webb, A. A. G. (2017). Heat-pipe planets. Earth and Planetary Science

  Letters, 474, 13–19.
- <sup>1454</sup> Moore, W. B., & Webb, A. A. G. (2013). Heat-pipe Earth. *Nature*, 501, 501–505.
- Morris, S., & Canright, D. (1984). A boundary-layer analysis of Benard convection in a fluid of strongly temperature-dependent viscosity. *Phys. Earth Planet. Inter.*, 36, 355–373.
- Morschhauser, A., Grott, M., & Breuer, D. (2011). Crustal recycling, mantle dehydration, and the thermal evolution of Mars. *Icarus*, 212, 541–558.
- Mulyukova, E., Steinberger, B., Dabrowski, M., & Sobolev, S. V. (2015). Survival of LLSVPs for billions of
- years in a vigorously convecting mantle: Replenishment and destruction of chemical anomaly. J. Geophys.
- 1461 Res. (Solid Earth), 120, 3824–3847.
- Nakagawa, T., & Tackley, P. J. (2012). Influence of magmatism on mantle cooling, surface heat flow and
  Urey ratio. Earth Planet. Sci. Lett., 329, 1–10.
- Nimmo, F., & Tanaka, K. (2005). Early Crustal Evolution of Mars. Ann. Rev. Earth Planet. Sci., 33, 133–161.

- Noack, L., & Breuer, D. (2014). Plate tectonics on rocky exoplanets: Influence of initial conditions and mantle rheology. *Planetary and Space Science*, 98, 41–49.
- Noack, L., Rivoldini, A., & Van Hoolst, T. (2017). Volcanism and outgassing of stagnant-lid planets:

  Implications for the habitable zone. *Phys. Earth Planet. Int.*, 269, 40–57.
- Ogawa, M., & Nakamura, H. (1998). Thermochemical regime of the early mantle inferred from numerical models of the coupled magmatism-mantle convection system with the solid-solid phase transitions at depths around 660 km. *Journal of Geophysical Research: Solid Earth*, 103, 12161–12180.
- Ogawa, M., Schubert, G., & Zebib, A. (1991). Numerical simulations of three-dimensional thermal convection in a fluid with strongly temperature-dependent viscosity. *J. Fluid Mech.*, 233, 299–328.
- Ogawa, M., & Yanagisawa, T. (2011). Numerical models of Martian mantle evolution induced by magmatism and solid-state convection beneath stagnant lithosphere. J. Geophys. Res. Planets, 116, E08008.
- O'Neill, C., & Lenardic, A. (2007). Geological consequences of super-sized Earths. Geophys. Res. Lett., 34, 19204–19208.
- O'Reilly, T. C., & Davies, G. F. (1981). Magma transport of heat on Io A mechanism allowing a thick lithosphere. *Geophys. Res. Lett.*, 8, 313–316.
- O'Reilly, T. C., & Davies, G. F. (1981). Magma transport of heat on io: A mechanism allowing a thick lithosphere. *Geophysical Research Letters*, 8, 313–316.
- Oxburgh, E., & Parmentier, E. (1977). Compositional and density stratification in oceanic lithosphere-causes and consequences. J. Geol. Soc., 133, 343–355.
- Plesa, A. C., & Breuer, D. (2014). Partial melting in one-plate planets: Implications for thermo-chemical and atmospheric evolution. *Planet. Space Sci.*, 98, 50–65.
- Plesa, A. C., Padovan, S., Tosi, N., Breuer, D., Grott, M., Wieczorek, M. A., Spohn, T., Smrekar, S. E.,
- & Banerdt, W. B. (2018). The Thermal State and Interior Structure of Mars. Geophys. Res. Lett, 45,
- 12,198-12,209.
- Plesa, A. C., Tosi, N., Grott, M., & Breuer, D. (2015). Thermal evolution and Urey ratio of Mars. J.

  Geophys. Res. Planets, 120, 995–1010.
- Reese, C., & Solomatov, V. (2009). Early martian dynamo generation due to giant impacts. *Icarus*, *In*Press, Accepted Manuscript, –.

- Reese, C., Solomatov, V., & Baumgardner, J. (2005). Scaling laws for time-dependent stagnant lid convection in a spherical shell. *Physics of the Earth and Planetary Interiors*, 149, 361–370.
- Reese, C. C., Solomatov, V. S., & Moresi, L.-N. (1998). Heat transport efficiency for stagnant lid convection with dislocation viscosity: Application to Mars and Venus. J. Geophys. Res., 103, 13643–13658.
- Richter, F. M., & Johnson, C. E. (1974). Stability of a chemically layered mantle. *Journal of Geophysical*Research, 79, 1635–1639.
- Richter, F. M., & McKenzie, D. P. (1981). On some consequences and possible causes of layered mantle convection. *Journal of Geophysical Research: Solid Earth*, 86, 6133–6142.
- Richter, F. M., Nataf, H.-C., & Daly, S. F. (1983). Heat transfer and horizontally averaged temperature of convection with large viscosity variations. *J. Fluid Mech.*, 129, 173–192.
- Ruedas, T., Tackley, P. J., & Solomon, S. C. (2013). Thermal and compositional evolution of the martian mantle: Effects of phase transitions and melting. *Phys. Earth Planet. Inter.*, 216, 32–58.
- Samuel, H., Lognonné, P., Panning, M., & Lainey, V. (2019). The rheology and thermal history of Mars revealed by the orbital evolution of Phobos. *Nature*, 569, 523–527.
- Schott, B., Van den Berg, A., & Yuen, D. A. (2001). Focussed time-dependent martian volcanism from chemical differentiation coupled with variable thermal conductivity. *Geophys. Res. Lett.*, 28, 4271–4274.
- Schubert, G., Cassen, P., & Young, R. E. (1979). Subsolidus convective cooling histories of terrestrial planets. *Icarus*, 38, 192–211.
- Semprich, J., Simon, N. S., & Podladchikov, Y. Y. (2010). Density variations in the thickened crust as a function of pressure, temperature, and composition. *International Journal of Earth Sciences*, 99, 1487–1514.
- Solomatov, S. (2015). Magma ocean and primordial mantle differentiation. In G. Schubert (Ed.), *Treatise*on Geophysics (pp. 81–104). Elsevier.
- Solomatov, V. (1995). Scaling of temperature-and stress-dependent viscosity convection. *Physics of Fluids*, 7, 266.
- Solomatov, V., & Barr, A. (2006). Onset of convection in fluids with strongly temperature-dependent, power-law viscosity. *Physics of the Earth and Planetary Interiors*, 155, 140–145.

- Solomatov, V., & Barr, A. (2007). Onset of convection in fluids with strongly temperature-dependent, power-
- law viscosity: 2. dependence on the initial perturbation. Physics of the Earth and Planetary Interiors,
- 1523 165, 1–13.
- Solomatov, V. S., & Moresi, L.-N. (2000). Scaling of time-dependent stagnant lid convection: Application
- to small-scale convection on Earth and other terrestrial planets. J. Geophys. Res., 105, 21795–21818.
- Spohn, T. (1991). Mantle differentiation and thermal evolution of Mars, Mercury, and Venus. *Icarus*, 90,
- 1527 222-236.
- Stamenkovic, V., Breuer, D., & Spohn, T. (2011). Thermal and transport properties of mantle rock at high
- pressure: Applications to super-earths. *Icarus*, 216, 572 596.
- 1530 Stein, C., Lowman, J. P., & Hansen, U. (2013). The influence of mantle internal heating on lithospheric
- mobility: Implications for super-Earths. Earth Planet. Sci. Lett., 361, 448–459.
- Stengel, K. C., Oliver, D. S., & Booker, J. R. (1982). Onset of convection in a variable-viscosity fluid. J.
- 1533 Fluid Mech., 120, 411–431.
- Stern, R. J., Gerya, T., & Tackley, P. J. (2018). Stagnant lid tectonics: Perspectives from silicate planets,
- dwarf planets, large moons, and large asteroids. Geosci. Front., 9, 103–119.
- Stevenson, D. J., Spohn, T., & Schubert, G. (1983). Magnetism and thermal evolution of the terrestrial
- planets. *Icarus*, 54, 466–489.
- Tackley, P. (2015). 7.12 Mantle Geochemical Geodynamics. In G. Schubert (Ed.), Treatise on Geophysics
- (Second Edition) (pp. 521 585). Oxford: Elsevier. (Second edition ed.).
- Tackley, P., Stevenson, D., Glatzmaier, G. A., & Schubert, G. (1993). Effects of an endothermic phase
- transition at 670 km depth in a spherical model of convection in the earth's mantle. Nature, 361, 699-
- 1542 704, .
- Tackley, P. J., & King, S. D. (2003). Testing the tracer ratio method for modeling active compositional fields
- in mantle convection simulations. Geochem., Geophys., Geosyst., 4.
- Taylor, S. R., & McLennan, S. (2009). Planetary crusts: their composition, origin and evolution volume 10.
- 1546 Cambridge University Press.
- Thiriet, M., Breuer, D., Michaut, C., & Plesa, A.-C. (2019). Scaling laws of convection for cooling planets
- in a stagnant lid regime. Phys. Earth Planet. Int., 286, 138–153.

- Thiriet, M., Michaut, C., Breuer, D., & Plesa, A.-C. (2018). Hemispheric Dichotomy in Lithosphere Thickness
- on Mars Caused by Differences in Crustal Structure and Composition. J. Geophys. Res. Planets, 123,
- 1551 823-848.
- Tosi, N., Godolt, M., Stracke, B., Ruedas, T., Grenfell, J. L., Höning, D., Nikolaou, A., Plesa, A.-C., Breuer,
- D., & Spohn, T. (2017). The habitability of a stagnant-lid Earth. Astron. Astrophys., 605, A71.
- Tosi, N., Plesa, A. C., & Breuer, D. (2013). Overturn and evolution of a crystallized magma ocean: A
- numerical parameter study for Mars. J. Geophys. Res. Planets, 118, 1512–1528.
- Tozer, D. (1967). Towords a theory of thermal convection in the mantle. In T. Gaskell (Ed.), The Earth's
- mantle (pp. 327–353). New York: Academic Press.
- Tozer, D. (1972). The present thermal state of the terrestrial planets. Phys. Earth Planet. Int., 6, 182–197,
- 1559
- Turcotte, D., & Schubert, G. (2002). Geodynamics. (2nd ed.). New York: Cambridge Univ. Press.
- Turcotte, D. L. (1989). A heat pipe mechanism for volcanism and tectonics on venus. Journal of Geophysical
- 1562 Research: Solid Earth (1978–2012), 94, 2779–2785.
- Unterborn, C. T., Johnson, J. A., & Panero, W. R. (2015). Thorium Abundances in Solar Twins and
- Analogs: Implications for the Habitability of Extrasolar Planetary Systems. Astrophys. J., 806, 139.
- Valencia, D., O'Connell, R. J., & Sasselov, D. (2006). Internal structure of massive terrestrial planets. *Icarus*,
- 181, 545–554.
- Valencia, D., O'Connell, R. J., & Sasselov, D. D. (2007). Inevitability of Plate Tectonics on Super-Earths.
- 1568 Astrophys. J., 670, L45–L48.
- Valencia, D., Tan, V. Y. Y., & Zajac, Z. (2018). Habitability from Tidally Induced Tectonics. Astrophys.
- J., 857, 106.
- van Heck, H. J., & Tackley, P. J. (2011). Plate tectonics on super-Earths: Equally or more likely than on
- Earth. Earth Planet. Sci. Lett., 310, 252–261.
- van Keken, P. E., King, S. D., Schmeling, H., Christensen, U. R., Neumeister, D., & Doin, M.-P. (1997).
- A comparison of methods for the modeling of thermochemical convection. J. Geophys. Res., 102, 22477—
- 1575 22495.

- Van Thienen, P. (2007). Convective vigour and heat flow in chemically differentiated systems. *Geophys. J.*1577

  Int., 169, 747–766.
- van Thienen, P., van den Berg, A. P., & Vlaar, N. J. (2004a). Production and recycling of oceanic crust in
  the early Earth. *Tectonophysics*, 386, 41–65.
- van Thienen, P., Vlaar, N. J., & van den Berg, A. P. (2004b). Plate tectonics on the terrestrial planets.

  Phys. Earth Planet. Inter., 142, 61–74.
- Vlaar, N. J. (1985). Precambrian geodynamical constraints. In *The Deep Proterozoic Crust in the North*Atlantic Provinces (pp. 3–20). Springer.
- Walker, J., Hays, P., & Kasting, J. (1981). A negative feedback mechanism for the long-term stabilization of the earth's surface temperature. *Journal of Geophysical Research*, 86, 9776–9782.
- Wanke, H., & Dreibus, G. (1994). Chemistry and Accretion History of Mars. *Phil. Trans. R. Soc. A*, 349,
   285–293.
- Weller, M. B., & Lenardic, A. (2016). The energetics and convective vigor of mixed-mode heating: Velocity scalings and implications for the tectonics of exoplanets. *Geophys. Res. Lett.*, 43, 9469–9474.
- Weller, M. B., Lenardic, A., & Moore, W. B. (2016). Scaling relationships and physics for mixed heating
  convection in planetary interiors: Isoviscous spherical shells. *Journal of Geophysical Research: Solid Earth*,
  121, 7598–7617.
- Wieczorek, M. A., & Zuber, M. T. (2004). Thickness of the Martian crust: Improved constraints from geoid-to-topography ratios. *J. Geophys. Res. Planets*, 109, E01009.
- Zaranek, S. E., & Parmentier, E. (2004). Convective cooling of an initially stably stratified fluid with
   temperature-dependent viscosity: Implications for the role of solid-state convection in planetary evolution.
   J. Geophys. Res. Solid Earth, 109.
- Zhao, Y.-H., Zimmerman, M. E., & Kohlstedt, D. L. (2009). Effect of iron content on the creep behavior of olivine: 1. anhydrous conditions. *Earth and Planetary Science Letters*, 287, 229–240.
- <sup>1600</sup> Zuber, M. T. (2001). The crust and mantle of Mars. Nature, 412, 220–227.